

Local temperature reconstruction from gas trapping processes in the Dye 3 ice core from Greenland

MASTER'S THESIS

by

David Aaron Soestmeyer

Supervisor: Priv.-Doz. Rebecca Hood-Nowotny

Co-supervisor: Prof. Thomas Blunier



University of Natural
Resources and Life Sciences
Department for Forest- and
Soil Sciences
Institute of Soil Research



EnvEuro –
Environmental Science
in Europe



University of Copenhagen
Faculty of Science
Department of Physics of
Ice, Climate and Earth

- page left intentionally blank for double sided print -

Affidavit

I hereby declare that this thesis is solely my original work. No help other than what is permitted has been used. All information taken from other sources have been identified as such and cited explicitly. This paper has not been submitted in any part for examination in the past.

Vienna,

17th December, 2020

Date

D. Sordmeyer

Signature

- page left intentionally blank for double sided print -

Abstract

Ancient air trapped in ice cores can reveal information about past atmospheres and climate conditions. The inert gas nitrogen and noble gas argon are gases with long atmospheric lifetimes – thus any alteration in their isotopic composition observed in ice cores is indicative of the drill site's past conditions. Using a combination of laboratory isotopic measurements and an inversion model, it is possible to reconstruct the site's past atmospheric temperature. This master thesis project developed a Continuous Flow Analysis (CFA) system to measure $\delta^{15}\text{N}$ of nitrogen and $\delta^{40}\text{Ar}$ of argon continuously from gas bubbles trapped in the Dye 3 ice core from South Greenland. The system gives an unprecedentedly high data resolution and generates results faster than previously established discrete measurements. A perovskite membrane was used to remove oxygen from the sample stream to obtain an improved $\delta^{40}\text{Ar}$ data quality. In total, 108 m of ice core were melted in 1 m sections continuously and then analyzed by mass spectrometry. The $\delta^{15}\text{N}$ data result in a realistic surface temperature reconstruction, however unfortunately it seems likely the $\delta^{40}\text{Ar}$ data suffer from analytical issues. A fitting algorithm coupled with a firn model were used to reconstruct the Dye 3 surface temperature. The reconstructed age section dating from 28,000 years to 44,000 years b2k includes Dansgaard-Oeschger (D-O) climatic events 4 to 11. It indicates an average warming of 22.41°C between the onset and peak temperature of the D-O events. In comparison with the NGRIP ice core from Central Greenland, the temperature reconstruction shows on average 10.35°C warmer temperatures for Dye 3 which is comparable to present day temperature differences. Compared to the discrete samples taken from Dye 3, the CFA $\delta^{15}\text{N}$ are on average 0.09‰ lower. Finally, as a result of the experience gained and the analytical challenges faced, suggestions are given to improve the data quality for future measurements.

- page left intentionally blank for double sided print -

Zusammenfassung

Eingeschlossene Gase aus Eisbohrkernen geben Informationen über vergangene Atmosphären und Klimabedingungen. Der reaktionsträge Stickstoff und das Edelgas Argon haben lange atmosphärischen Lebensdauern, daher weisen Änderungen in der Isotopenzusammensetzung auf Klimaveränderungen an der Bohrstelle hin. Durch isotopische Messungen und ein Inversionsmodell ist es möglich die vergangenen Temperaturen an der Bohrstelle zu rekonstruieren. Diese Masterarbeit hat ein Verfahren zur Kontinuierlichen-Fluss-Analyse (CFA) entwickelt, um $\delta^{15}\text{N}$ (Stickstoff) und $\delta^{40}\text{Ar}$ (Argon) aus Gasblasen des Dye 3 Eisbohrkerns aus Südgrönland zu messen. Damit gibt eine höhere Datendichte und schneller verfügbare Daten als mit konventionellen diskreten Messungen. Eine Perowskit-Membran wurde genutzt, um Sauerstoff aus der Luft zu filtern und eine bessere $\delta^{40}\text{Ar}$ Datenqualität zu erreichen. Insgesamt wurden 108 m Eisbohrkern in 1 m langen Sektionen geschmolzen und dann mithilfe von Massenspektrometrie analysiert. Die Ergebnisse von $\delta^{15}\text{N}$ zeigen eine realistische Rekonstruktion der Oberflächentemperatur, die $\delta^{40}\text{Ar}$ Daten unterliegen analytischen Problemen. Dementsprechend wurden nur die CFA $\delta^{15}\text{N}$ genutzt, um mithilfe eines automatisierten Anpassungs-Algorithmus und einem Firn-Modell die Oberflächentemperatur zu rekonstruieren. Der Altersabschnitt von 28.000 bis 44.000 Jahren b2k beinhaltet die Dansgaard-Oeschger (D-O) Klimaereignisse 4 bis 11. Die Ergebnisse zeigen eine durchschnittliche Erwärmung von $22,41^\circ\text{C}$ zwischen dem Start und Höhepunkt der D-O Ereignisse. Im Vergleich mit dem NGRIP Eisbohrkern zeigt die Rekonstruktion durchschnittlich $10,35^\circ\text{C}$ wärmere Temperaturen für Dye 3, was vergleichbar mit heutigen Temperaturunterschieden ist. Verglichen mit den diskreten Messungen von Dye 3 sind die CFA $\delta^{15}\text{N}$ durchschnittlich um $0,09\text{‰}$ niedriger. Basierend auf den gemachten Erfahrungen und analytischen Herausforderungen werden Vorschläge gegeben, um die Datenqualität für zukünftige Messungen zu verbessern.

- page left intentionally blank for double sided print -

Acknowledgements

Foremost, I would like to thank Priv.-Doz. MBA Ph.D. Rebecca Hood-Nowotny for her encouragements, her scientific advice and patience with me in her role as main supervisor.

Furthermore, I would like to thank Professor Thomas Blunier for his analytical expertise, his scientific guidance, his support and his patience as co-supervisor during the laboratory work as well as during the thesis writing process.

My deepest gratitude and appreciation go to Jesper Baldtzer Liisberg with whom I worked to together for setting up the measurement system, the sample measurements and for the data analysis.

I would like to thank Jens Will Iversen for supporting the data analysis with the basic version of the Matlab data evaluation script.

A big thanks goes to Janani Venkantesh, Michael Döring, Michael Dionysus for providing valuable feedback on my thesis that helped me improve the final version that was submitted.

I would like to thank Orsolya Ludmany, Susanne Wangert and Lara Möllney for deep and good conversations, detailed feedback and encouragements during the writing process.

Finally, I would like to thank the gas measurement group at PICE, the international CFA measurement campaign team and the PICE section of NBI for the good and interesting time as well as various scientific insights into ice and earth sciences.

- page left intentionally blank for double sided print -

List of figures

Figure 0.1: Location of the Dye 3 ice core drilling site (Johnsen et al., 2001)	24
Figure 1.1: NGRIP Temperature reconstruction from 9,000 to 49,000 years b2k on the ss09sea06bm timescale. The temperature reconstruction (red) is done based on $\delta^{15}\text{N}$ data (dark and light blue). The modelled temperature amplitude is given for the D-O events. The black line is the modelled $\delta^{15}\text{N}$. $\delta^{18}\text{O}_{\text{ice}}$ data (grey points) and $\delta^{15}\text{N}$ data is shown for comparison and the D-O events and Heinrich events (yellow/red) are marked and numbered. (Kindler et al., 2014).	28
Figure 1.2: The basic functioning principle of a mass spectrometer (Thermo Fisher Scientific, n.d.).....	31
Figure 1.3: A simplified setup scheme for an example of a CFA measurement system based on this study. Dark red is the melthead. Black lines are mixed gas and liquid flows. Orange lines are gas flows and blue lines are liquid flows. MM is the Micromodule that was used for gas extraction from the sample stream.	33
Figure 1.4: A sketch of the firn column and influence on $\delta^{15}\text{N}$ (Blunier and Schwander, 2000).	34
Figure 2.1: An example of a discrete measurement system based on Kobashi et al., (2008). .	37
Figure 3.1: Zoom on the standard line setup: The flow passed to the IRMS was controlled by the forward pressure controller at 145 mbar. The standard capillary (yellow) was passed through the T-piece so that it reached the upstream end of it and could measure the standard.....	42
Figure 3.2: Schematic overview of the PICE 2019 CFA system used for this study.....	43
Figure 3.3: Zoom on the oven setup with the BCFZ membrane that extracted the oxygen from the sample stream.....	44
Figure 3.4: Scheme of the on-line measurement system according to Huber and Leuenberger, (2004).....	47
Figure 3.5: Picture of the BCFZ hollow fiber membrane under a micrograph (Liang, 2010).	47
Figure 3.6: Graph showing the oxygen removal dependency on the oven temperature. The temperature was increased in 50°C steps from 250°C to 850°C.	48
Figure 3.7: Graph showing the oxygen removal dependency on the BPR setpoint of the oven setup. The pressure setpoints were varied between 130 mbar and 900 mbar. Additionally, the pressure difference between total atmospheric pressure and BPR setpoint is shown (1000 mbar – pressure setpoint).	49
Figure 3.8: Graph showing the oxygen removal dependency on the counter-sample helium flow.....	50
Figure 3.9: Graph showing the intensity of nitrogen (mass 28) during the measurement run of the 5 th November 2019.	52
Figure 3.10: The gas age before the year 2000 (b2k) and depth assignment based on the methane measurements. The dashed yellow line indicates a linear extrapolation between the two depth sections of Dye 3 that were measured.	62
Figure 4.1: Combined results from 11,000 to 16,000 years b2k showing CH_4 , $\delta^{15}\text{N}$, $\delta^{40}\text{Ar}$, $\delta\text{Ar}/\text{N}_2$ on the preliminary gas age scale. $\delta^{18}\text{O}$ (ice) is shown for comparison on	

the assigned ice age scale (GIC05) and was provided by Bo M. Vinther (PICE). This first section corresponds to depths from 1780 m to 1821 m.	64
Figure 4.2: Combined results from 28,000 to 44,000 years b2k showing CH ₄ , δ ¹⁵ N, δ ⁴⁰ Ar, δAr/N ₂ on the preliminary gas age scale. δ ¹⁸ O is shown for comparison on the assigned ice age scale (GIC05) and was provided by Bo M. Vinther (PICE). This second section shown corresponds to depths from 1865 m to 1920 m.	65
Figure 4.3: Overview of variations observed on δ ¹⁵ N and δ ⁴⁰ Ar during the daily calibrations of standard (nitrogen-argon mix) against lab air.	67
Figure 4.4: Daily δ ¹⁵ N calibrations of the 30th and 31st October 2019.	68
Figure 4.5: Daily δ ¹⁵ N calibrations of the second measurement week (4 th to 7 th November 2019) excluding the morning calibration of the 4 th November when the Argon was turned off accidentally.	68
Figure 4.6: δ ⁴⁰ Ar calibration values of the 30th and 31st October 2019.	69
Figure 4.7: δ ⁴⁰ Ar calibration values of the second measurement week excluding the morning calibration of the 4 th November when the argon was turned off.	70
Figure 4.8 and Figure 4.9: The impact of CO ₂ removal on the δ ¹⁵ N and δ ⁴⁰ Ar data on a depth scale.	71
Figure 4.10: Graph showing the impact of the CO ₂ spike on the δ ¹⁵ N data on a depth scale. .	72
Figure 4.11: Graph showing the impact of the CO ₂ spike on the δ ⁴⁰ Ar data on a depth scale.	73
Figure 4.12 and Figure 4.13: Graphs showing the impact of the oxygen removal on δ ¹⁵ N and δ ⁴⁰ Ar data.	74
Figure 4.14: Overview of the discrete δ ¹⁵ N and CFA δ ¹⁵ N measurements from Dye 3 on a depth scale.	75
Figure 4.15: Comparison of δ ¹⁵ N of discrete and CFA measurements in depth zone 1 ranging from 1786 m to 1790 m.	76
Figure 4.16: Comparison of δ ¹⁵ N of discrete and CFA measurements in depth zone 2 ranging from 1879.5 m to 1881.25 m.	77
Figure 4.17: Comparison of δ ¹⁵ N of discrete and CFA measurements in depth zone 3 ranging from 1884.5 m to 1886.5 m.	78
Figure 4.18: Comparison of δ ¹⁵ N of discrete and CFA measurements in depth zone 4 ranging from 1899.0 m to 1900.5 m.	79
Figure 4.19 and Figure 4.20: δ ¹⁵ N from this study plotted on a (preliminary) gas age scale for Dye 3. NGRIP δ ¹⁵ N is plotted for comparison for the period 11,000 to 16,000 years b2k (Figure 4.19) and 26,000 to 44,000 years b2k (Figure 4.20)	81
Figure 4.21: Accumulation rates, mean annual temperature and firn depth at different ice core drill sites in Antarctica and Greenland. NGRIP is expected to be at a firn depth and temperature similar to GRIP and Crete at approximately 70 m and marked in orange. Dye 3 is marked in blue. (Provided by Thomas Blunier through personal communication, 2019 calculated in steady state with the Schwander model (Schwander et al., 1993)).	82
Figure 4.22: A calculation based on firn depth and surface temperatures calculated assuming steady state conditions taking into account gravitational settling and molecular diffusion. Calculated after equation 1.5 (gravitational settling).	83

Figure 4.23: The measured and modelled $\delta^{15}\text{N}$ data on a gas age scale for 28,000 to 44,000 years b2k. Orange is the modelled data, blue is measured data.	86
Figure 4.24: The temperature reconstruction based on the observed Dye 3 $\delta^{15}\text{N}$ values. The reconstructed temperature is shown in red. The observed D-O events 4-11 are marked in light blue and numbered.	86
Figure 4.25: The modelled Lock-In-Depth (LID) based on the CFA $\delta^{15}\text{N}$ values. The LID for D-O event 5.1 is marked in red.	87
Figure 4.26: The temperature amplitude difference from Dye 3 to NGRIP for the measured D-O events (28,000 to 44,000 b2k). The NGRIP temperature reconstruction was done by Kindler et al. (2014). The NGRIP temperature reconstruction can be seen in Figure 1.1,.....	89

- page left intentionally blank for double sided print -

List of tables

Table 1.1: Natural abundances of relevant isotopes according to (Krebs, 2006). Mass 36 (marked in bold) can be either a clumped isotope of oxygen ($^{18}\text{O}_2$) or an argon molecule.....	29
Table 3.1: Overview of the data acquisition times and total meters melted. *The total meters melted are based on the finalized depth assignment and therefore include missing parts and pieces that were too small for the gas CFA (<3.5x3.5 cm in cross-section). The actual melted sample from Dye 3 was approximately 108 m.....	53
Table 3.2: Daily ratio, daily offset and uncertainty of $\delta^{29}\text{N}$, $\delta^{40}\text{Ar}$ and $\delta\text{Ar}/\text{N}_2$ following Baldtzer Liisberg (2020). For the 5 th November two averages were generated, one for the morning run (*) and one for the afternoon run (**).	54
Table 4.1: Mean offsets for the different depth zones and the 2σ standard deviation.....	79
Table 4.2: Modelled $\delta^{15}\text{N}$ for Dye 3 and NGRIP based on present day firn properties and temperatures.....	83
Table 4.3: Onset temperature (T_{onset}), peak temperature (T_{peak}) and the temperature difference between onset and peak ($T_{\text{onset-peak}}$) for the D-O events from 28,000 to 44,000 years b2k.....	88

- page left intentionally blank for double sided print -

List of abbreviations

Abbreviation	Meaning
b2k	Before the year 2000
BP	Before Present (1950)
BPR	Back Pressure Regulator
CFA	Continuous Flow Analysis
CIC	Center for Ice and Climate at the University of Copenhagen (now called PICE)
COD	Close-Off-Depth
Dye 3	Ice core from South Greenland used for this study
D-O event	Dansgaard-Oeschger climatic event
FPR	Forward Pressure Regulator
ID	Inner Diameter
IRMS	Isotopic Ratio Mass Spectrometry
LID	Lock-In-Depth
MQ	MilliQ water, clean water without contamination
NGRIP	North GReenland Ice sheet Project (ice core from Central North Greenland)
OD	Outer Diameter
PICE	Department of Physics of Ice Climate and Earth, Faculty of Science of the University of Copenhagen

- page left intentionally blank for double sided print -

Table of contents

Affidavit	Error! Bookmark not defined.
Abstract.....	5
Zusammenfassung	7
Acknowledgements	9
List of figures	11
List of tables	15
List of abbreviations	17
Table of contents	19
Introduction and objectives	23
1. Theoretical background.....	26
1.1 Information about past climates from ice cores	26
1.2 Ice core drilling in Greenland	27
1.3 Important climatic events during the past 50,000 years	28
1.4 Definition of isotopes.....	29
1.5 The delta notation	30
1.6 Mass spectrometry	31
1.7 CFA measurements versus discrete sampling	32
1.8 Firn processes	34
1.8.1 Gravitational settling	35
1.8.2 Thermal fractionation	35
1.9 Age difference between ice and gases	36
2 Literature Review.....	36
2.1 Discrete argon and nitrogen measurements from ice cores	36
2.2 Combined argon and nitrogen measurements.....	37
2.3 CFA measurements.....	38

3	Methodology	40
3.1	General description of the CFA setup.....	40
3.2	Overview over the development challenges	45
3.3	Comparison of the Huber et al. setup the PICE 2019 CFA setup.....	46
3.4	The perovskite membrane.....	47
3.5	Oxygen removal efficiency testing with laboratory air	48
3.6	Ice preparation	51
3.7	Calibration runs.....	51
3.8	Sample measurements.....	52
3.9	Overview of data acquisition times.....	53
3.10	Data processing	54
3.11	Applied corrections.....	55
3.11.1	Background correction	56
3.11.2	Calculation of isotopic ratios.....	56
3.11.3	Pressure imbalance correction.....	56
3.11.4	Chemical slope correction	58
3.11.5	Solubility effect correction	58
3.12	Removal of lab air contamination and smoothing.....	60
3.13	Error calculation	61
3.14	Depth and age assignment	61
3.14.1	Depth scale	61
3.14.2	Gas age scale	61
4	Results and Discussion.....	63
4.1	Combined results overview	64
4.2	Calibration runs.....	66
4.2.1	Calibration results for nitrogen.....	68
4.2.2	Calibration results for argon.....	69
4.3	Removal of CO ₂	71

4.4	Removal of oxygen.....	73
4.5	Comparison of CFA $\delta^{15}\text{N}$ data with discrete Dye 3 $\delta^{15}\text{N}$	75
4.6	Comparison of Dye 3 $\delta^{15}\text{N}$ with NGRIP $\delta^{15}\text{N}$	80
4.7	Temperature reconstruction	84
5	Suggestions for future improvements	91
	Conclusion.....	93
	References	95
	Appendix	99
	Appendix 1. Oven setup showing the potential vacuum solution for oxygen removal	99
	Appendix 2. Main matlab script for data evaluation	99
	Appendix 3. Matlab script for applying the pressure imbalance and chemical slope corrections.....	106
	Appendix 4. Matlab script for applying the solubility effect corrections	109
	Appendix 5. Pressure imbalance slopes found experimentally	111
	Appendix 6. Chemical slopes found experimentally	113
	Appendix 7. Error propagation for $\delta^{29}\text{N}_2$	115
	Appendix 8. Error propagation for $\delta^{40}\text{Ar}$	115
	Appendix 9. Error propagation for $\delta\text{Ar}/\text{N}_2$	116

- page left intentionally blank for double sided print -

Introduction and objectives

Human-induced climate change has the potential to cause significant and adverse effects for society, both now and in the future. The impacts of climate change can already be observed today; some of these effects include an increase in extreme weather events, sea level rise and loss of biodiversity (Masson-Delmotte et al., 2018). Predicting future climate change is important in order to develop mitigation strategies and implement adaptation measures (Masson-Delmotte et al., 2018). One way to identify drivers and feedback mechanisms in Earth's climate system is to study past climate variations, especially abrupt climate transitions over relatively short time periods (Stoller-Conrad, 2017).

The analysis of the chemical composition of gas bubbles trapped in ice cores can be used to reconstruct the Earth's past temperature variations (Lang et al., 1999). The firn is the uppermost part of the ice sheet where snow gradually transforms to ice (Herron and Langway, 1980). The ratios of non-reactive gases such as nitrogen (N_2) and argon (Ar), as well as their isotopic signatures in ice cores contain information about the firn structure back in time (Severinghaus et al., 1998). With the help of a firn model, it is possible to reconstruct past firn column temperatures and depths, as well as past atmospheric temperature variations of ice core drill sites (Landais et al., 2004).

This master thesis project developed a new analytical method for combined gas and wet chemistry measurements using Continuous Flow Analysis (CFA), building from methods previously developed by Huber and Leuenberger (2004) and the existing CFA-setup at the Department of Physics of Ice Climate and Earth (PICE). The measurement setup now allows for simultaneous measurements $\delta^{15}N$, $\delta^{40}Ar$, $\delta Ar/N_2$ as well as the CH_4 concentration and wet chemistry parameters (sodium (Na^+), ammonium (NH_4^+), calcium (Ca^{2+}), pH, conductivity and dust). The Dye 3 ice core from Southern Greenland ($65^{\circ}11'N$, $43^{\circ}50'W$, Figure 0.1) was melted continuously in 1 m sections (as compared to discrete samples of 10 to 45 cm). The isotopic ratios of nitrogen ($\delta^{15}N$) and argon ($\delta^{40}Ar$) were measured and analysed for the purpose of reconstructing the past temperature variations at this location. Dye 3 is the southernmost ice core drill site in Greenland and located relatively far away from other deep ice cores. In a data assimilation approach (i.e., using climate models to match observations), temperature reconstructions at the Dye 3 site provide important constraints for the overall Greenland temperature reconstruction because of its unique location in Southern Greenland (Badgley et al., 2020).

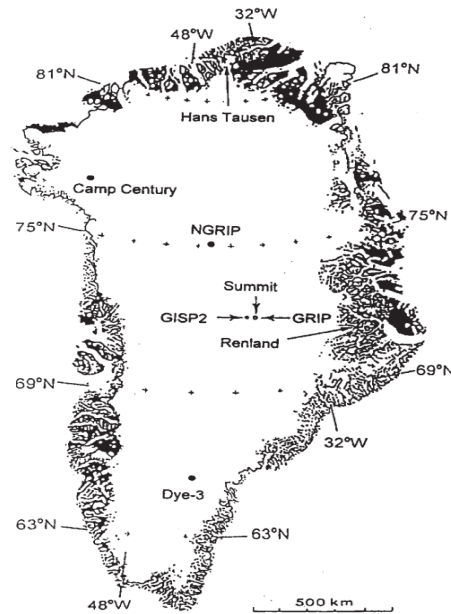


Figure 0.1: Location of the Dye 3 ice core drilling site (Johnsen et al., 2001)

This thesis consists of 5 chapters: (1) Theoretical background, (2) Literature review, (3) Methodology, (4) Results and discussion and (5) Suggestions for future improvements on the measurement system and finishes with a conclusion.

The first chapter (Theoretical background), gives a short overview on the parameters measured from ice cores for different purposes, the history of ice core drilling in Greenland and important paleoclimatic events during the past 50,000 years. Moreover, it provides a review on the basics of isotopes and delta notation, mass spectrometry, advantages and disadvantages of CFA and discrete measurements. Furthermore, the firn layer and its processes (gravitational settling and thermal fractionation) will be defined. This chapter finishes with a sub chapter on the age difference between ice age and gas age.

The second chapter (Literature review) deals with the history of the studies of ice cores based on previously conducted research on $\delta^{15}\text{N}$ and $\delta^{40}\text{Ar}$ with a focus on discrete and CFA measurements and how they developed over time during the past 40 years.

The third chapter (Methodology) gives a general description of the CFA measurement setup, an overview about the development challenges and compares the PICE 2019 setup to the setup of Huber et al. (2004). The perovskite membrane that was used for oxygen removal from the sample stream is presented along with the results of oxygen removal depending on oven temperature, sample flow and helium flow. Following that, the ice preparation process is described. The sample measurements and standard calibrations are presented and an overview about data acquisition times is given. The data processing is described, and the applied corrections such as background, pressure imbalance, chemical slope and solubility effect

correction are shown. The cleaning of the data from lab air contamination and the applied smoothing to get the final dataset is described. Finally, the error correction, the depth and age assignment process are presented.

The fourth chapter (Results) gives an overview of the results obtained by the PICE 2019 measurement campaign and a preliminary interpretation. The results of the daily calibration runs and the removal of O₂ and CO₂ from the sample stream are discussed as a potential factor for anomalies seen in the data. The CFA $\delta^{15}\text{N}$ results are compared with the discrete Dye 3 samples performed by Todd Sowers from Pennsylvania State University (United States) and in a further sub-chapter to the discrete $\delta^{15}\text{N}$ from the NGRIP ice core. The temperature reconstruction based on CFA $\delta^{15}\text{N}$ data from this study as the input for the fitting algorithm by Döring and Leuenberger (2018) is presented and then compared to the Kindler et. al. (2014) temperature reconstruction of the NGRIP ice core.

The fifth chapter (Suggestions for future improvements) gives suggestions for potential improvements on the analytical system to obtain better quality data in the future.

Finally, this thesis finishes with a conclusion on the results obtained by this study and further research opportunities in the field of ice core studies.

1. Theoretical background

In this first chapter, information that can be inferred from ice cores about past climates is presented, followed by a short chapter on ice core drilling in Greenland and important paleoclimatic events. On the analytical side, the basic notions of environmental isotopes, the delta notation and the principles of mass spectrometry are introduced. Furthermore, ice core analysis methods such as discrete sampling and CFA measurements are presented and compared. Moreover, the firn and its underlying fractionation processes e.g. gravitational settling and thermal fractionation will be introduced. Finally, the age difference between the ice age and gas age is presented.

1.1 Information about past climates from ice cores

Ice cores provide a wide range of information about past climates by analysing the gas bubbles trapped in the ice and the chemical composition of the ice (Dansgaard, 2004).

Wet chemistry parameters such as acidity, dust and calcium reveal volcanic events and give evidence about the chemistry of past atmospheres and weather conditions (Dansgaard, 2004). Isotopic analysis of $\delta^{18}\text{O}$ from water isotopes of the ice allow a temperature reconstruction at the time of deposition of precipitation (Dansgaard, 2004). The delta notation will be described further on in chapter 1.5.

The analysis of the gases trapped in the ice yields the concentration of greenhouse gases such as CO_2 and CH_4 indicate the magnitude of the greenhouse effect in past atmospheres (Dansgaard, 2004). $\delta^{15}\text{N}$ and $\delta^{40}\text{Ar}$ (that will be measured during this thesis project) allow a reconstruction of past firn conditions. Subsequently, it is possible to invert past temperatures based on accumulation rate and atmospheric temperatures in combination with a firn model (Severinghaus et al., 1998). Chapter 1.8 *Firn processes* gives a more detailed definition of the ongoing processes in the firn.

1.2 Ice core drilling in Greenland

Ice core drilling in Greenland has a long history of almost 70 years. The first, mostly shallow, ice cores in Greenland were drilled in the 1950s by the US Army Snow, Ice and Permafrost Research Establishment (SIPRE) (CIC, 2008a). From 1963 to 1966, the first deep ice core was drilled and reached bedrock at the *Camp Century* drill site at a depth of 1390 m (Dansgaard, 2004).

In the early 1970's, there were no deep cores drilled in Greenland because the drill used for Camp Century was lost during a drilling operation at Byrd station (Antarctica) and therefore, a new drill needed to be developed which needed time and funding (Dansgaard, 2004).

From 1979 to 1981, the *Dye 3* deep ice core (that was measured for this study) was drilled with the then newly developed ISTUK drill and reached bedrock at a depth of 2,038 m (Dansgaard, 2004).

During the late 1980s, the Greenland Ice core Project (*GRIP*) drilled an ice core and reached bedrock at 3,029 m in 1992 (CIC, 2008b). In 1993, a group of American researchers with the *GISP* project drilled to bedrock around 30 km westwards from the GRIP drill site (CIC, 2008b).

More ice cores were drilled during the 90's and 2000's with the North Greenland Ice sheet Project (*NGRIP*, reached bedrock in 2003 at 3,085 m) and North Greenland Eemian Ice Drilling (*NEEM*, reached bedrock in 2003 at 2,542 m) deep ice cores (CIC, 2008c). Currently, an international research group is drilling into the North East Greenland Ice Stream (NEGIS) with the *EastGRIP* drilling project (Niels Bohr Institute, 2016) and is expected to reach bedrock in 2021.

1.3 Important climatic events during the past 50,000 years

Studies of ice cores and other proxies have shown that the climate varied significantly during the last 50,000 years and beyond as seen in Figure 1.1 (Kindler et al., 2014). However, the climate has been remarkably stable for the last approximately 11,500 years during the *Holocene* period since the end of the last ice age (Rahmstorf, 2002).

Important paleoclimatic events during the last 50,000 years are the Dansgaard-Oeschger (hereafter D-O-events) and Heinrich events (Rahmstorf, 2002). Rapid warming events (the D-O events) over a relatively short time span were identified during the last glacial period and are numbered in black (Kindler et al., 2014). Heinrich events are marked in yellow or red and are identified with “H”. They are assumed to be caused by massive iceberg discharges from the Laurentide ice sheet over North America through the Hudson Strait that resulted in a slowdown of North Atlantic Deepwater Formation which lead to colder temperatures (Bond et al., 1992). The leading hypothesis for D-O and Heinrich events is that they are caused by changes (strengthening or weakening) in ocean circulation in the North Atlantic (Broecker et al., 1985; Rahmstorf, 2002).

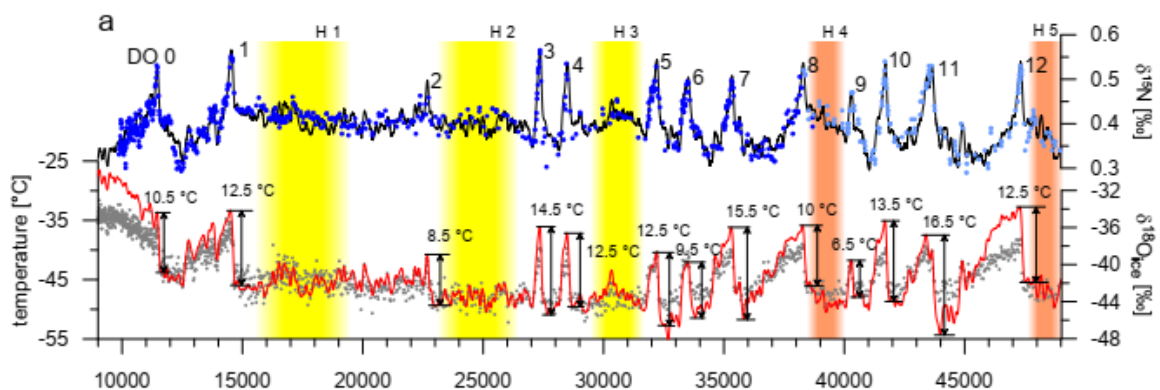


Figure 1.1: NGRIP Temperature reconstruction from 9,000 to 49,000 years b2k on the ss09sea06bm timescale. The temperature reconstruction (red) is done based on $\delta^{15}N$ data (dark and light blue). The modelled temperature amplitude is given for the D-O events. The black line is the modelled $\delta^{15}N$. $\delta^{18}O_{ice}$ data (grey points) and $\delta^{15}N$ data is shown for comparison and the D-O events and Heinrich events (yellow/red) are marked and numbered. (Kindler et al., 2014).

1.4 Definition of isotopes

The number of protons defines an element (Hoefs, 2009). *Isotopes* of elements possess an equal number of protons but differ in number of neutrons (ibid.). As a result, the molecular mass is different between different isotopes of the same element due to the difference in the number of neutrons (ibid.).

The standard isotopic notation is given by:

$${}^{Z+N}_{Z}\text{X}^N \quad (1.1)$$

where **X** is the element, **Z** is the number of protons, **N** is the number of neutrons.

However, for brevity reasons, often only the form of ${}^{Z+N}\text{X}$ is used, in the case for this thesis: ${}^{15}\text{N}$ and ${}^{40}\text{Ar}$.

The natural abundance of isotopes varies. Below, Table 1.1 provides a list of the three most important stable (meaning non-radioactive) isotopes relevant for this thesis: argon, nitrogen and oxygen.

Element	Elemental mass (molecular mass)	Natural abundance
Nitrogen	14 (28)	99.634%
Nitrogen	15 (29)	0.366%
Oxygen	16 (32)	99.762%
Oxygen	17 (34)	0.038%
Oxygen	18 (36)	0.200%
Argon	36 (36)	0.3365%
Argon	38 (38)	0.0632%
Argon	40 (40)	99.6003%

Table 1.1: Natural abundances of relevant isotopes according to (Krebs, 2006). Mass 36 (marked in bold) can be either a clumped isotope of oxygen (${}^{18}\text{O}_2$) or an argon molecule.

The fact of different molecular masses resulting in different charges when ionized can be used in isotopic ratio mass spectrometry (IRMS) to access the isotopic ratios of argon, nitrogen and oxygen (Hoefs, 2009).

1.5 The delta notation

Variations between isotopic ratios in the natural environment are relatively small (changes from the third decimal are common) and therefore, the *delta notation* is used for showing differences in the permille spectrum (Hoefs, 2009).

The sample will be expressed relative to the laboratory air standard and the results will be shown as delta values of the different masses.

As an example, the delta notation for $\delta^{15}\text{N}$ (nitrogen) is given by:

$$\delta^{15}\text{N} = \left(\frac{R_{\text{sample}}}{R_{\text{standard}}} - 1 \right) * 1000 (\text{‰}) \quad (1.2)$$

For $\delta^{15}\text{N}$, $\mathbf{R}_{\text{sample}}$ is the ratio of mass 29/28 of the sample and $\mathbf{R}_{\text{standard}}$ is the ratio of mass 29/28 of the standard.

The same notation principle is valid for the delta values of $\delta^{40}\text{Ar}$ (argon):

$$\delta^{40}\text{Ar} = \left(\frac{R_{\text{sample}}}{R_{\text{standard}}} - 1 \right) * 1000 (\text{‰}) \quad (1.3)$$

For $\delta^{40}\text{Ar}$, $\mathbf{R}_{\text{sample}}$ is the ratio of mass 40/36 of the sample and $\mathbf{R}_{\text{standard}}$ is the ratio of mass 40/36 of the standard.

Additionally, the δ -value of the elemental ratio $\delta\text{Ar}/\text{N}_2$ (mass 40/28) was measured. Similar to the delta notations described above, $\delta\text{Ar}/\text{N}_2$ is given by:

$$\delta\text{Ar}/\text{N}_2 = \left(\frac{R_{\text{sample}}}{R_{\text{standard}}} - 1 \right) * 1000 (\text{‰}) \quad (1.4)$$

For $\delta\text{Ar}/\text{N}_2$, the $\mathbf{R}_{\text{sample}}$ is the ratio of mass 40/28 of the sample and $\mathbf{R}_{\text{standard}}$ is the ratio of mass 40/28 of the standard.

1.6 Mass spectrometry

Mass spectrometry is one of the most widely used analysis techniques in research and used for various disciplines ranging from geology over biology to medical research (Thermo Fisher Scientific, n.d.).

The gas sample arrives through a capillary (to restrict the incoming flow) inside the mass spectrometer driven by a pressure gradient from atmospheric pressure to a vacuum inside the instrument. Once inside the instrument, the sample is ionized, accelerated and deflected by an electric magnet according to the corresponding mass to charge ratio (m/z) of the elements in the air which means that heavier masses get less deflected than lighter masses (Thermo Fisher Scientific, n.d.). The ionized sample hits Faraday detector cups and the registered signal is amplified before being sent to the software showing the intensities [in mV] of the different masses (Thermo Fisher Scientific, n.d.).

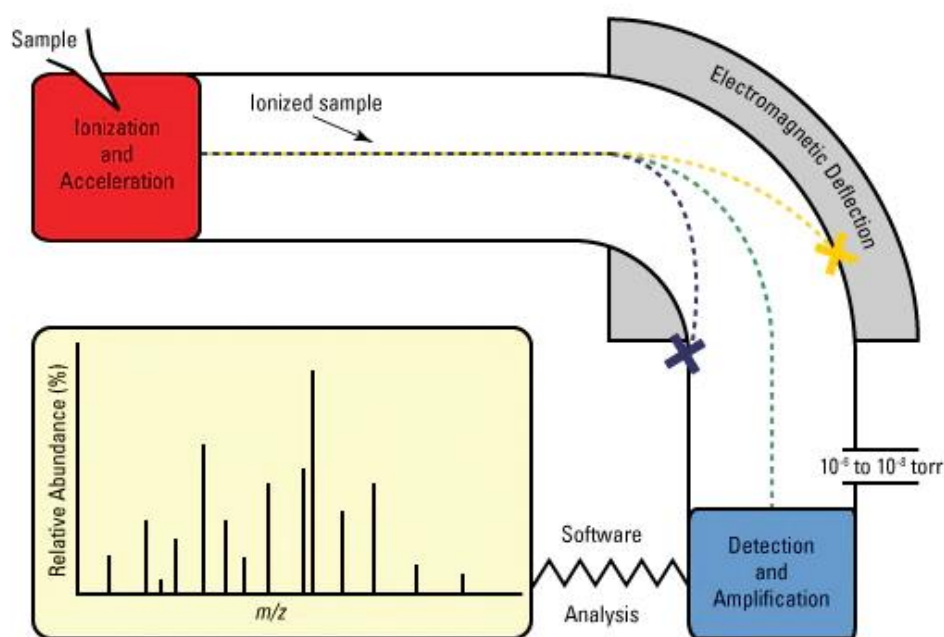


Figure 1.2: The basic functioning principle of a mass spectrometer (Thermo Fisher Scientific, n.d.).

For this project, the Isotopic Ratio Mass Spectrometer (IRMS) Delta V from Thermo Fisher was used to measure the argon and nitrogen isotope ratios of the gas bubbles trapped in the Dye 3 ice core. However, for the ^{36}Ar measurements there is a potential interference from clumped isotopes $^{18}\text{O}_2$ because they have both mass 36 (as already shown in Table 1.1). For this reason, oxygen gas (O_2) was removed from the air stream thanks to a perovskite membrane before entering the IRMS to minimize the potential interference as suggested by Huber et al. (2004) to improve the ^{36}Ar data.

1.7 CFA measurements versus discrete sampling

Two different measurement methods are used to analyse different parameters from ice cores: 1) discrete sampling and 2) continuous flow analysis (CFA). This chapter gives a short overview about the key concepts and components of the two measurement techniques, their advantages and inconveniences.

In discrete sampling, the ice samples are cut into a certain length, usually between 10 and 45 cm and put into an extraction vessel (Kindler et al., 2014). For measurements of non-reactive gases such as N₂, O₂ and noble gases (Argon, Neon, Krypton, Xenon) the ice is melted inside a vacuum vessel with a hot water bath. The gas in the headspace is then passed through different cryogenic traps (liquid nitrogen traps) and catalysts such as an Zr/Al getter material to remove gases that are not needed for measurements (Kobashi et al., 2008). An IRMS is used to obtain the isotopic data (Kobashi et al., 2008). This type of method is generally more accurate and precise when compared to CFA, but more time consuming as every sample must be prepared and passed through the measurement apparatus individually (Kindler et al., 2014).

During the past three decades, continuous flow analysis (CFA) measurement setups were developed which enable a higher resolution than discrete sampling obtained in a shorter time frame (Schüpbach et al., 2009). The first ones were developed by Fuhrer et al., (1993), Sigg et al., (1994) and Röthlisberger et al., (2000). This then novel measurement technique allowed a resolution of 1 cm and measurements of 20 m of ice in one day, which was a huge acceleration compared to conventional discrete sampling (Röthlisberger et al., 2000). It was first designed to measure only wet chemistry parameters (and no gases yet) such as sodium, nitrate, sulfate, electrolytical conductivity, ammonium, calcium, hydrogen peroxide and formaldehyde (Röthlisberger et al., 2000).

The data for this thesis was obtained by using a CFA measurement system. A simplified scheme (Figure 1.3 below) describes the basic principles of this measurement technique. The ice core (usually 1 m long samples with 3.5x3.5 cm in cross-section) is melted continuously at a melthead temperature of around 50°C inside a freezer at -20°C (1). The mixed gas and liquid sample is pumped away with a peristaltic pump (2). A debubbler and a MicroModule (3) separate the liquid and gas flow afterwards, so that the wet sample can be carried to the wet chemistry measurements (4). A Nafion membrane (5) is used to remove the remaining humidity from the gas flow and a liquid nitrogen trap (6) removes heavy molecules (e.g. CO₂) before entering the IRMS.

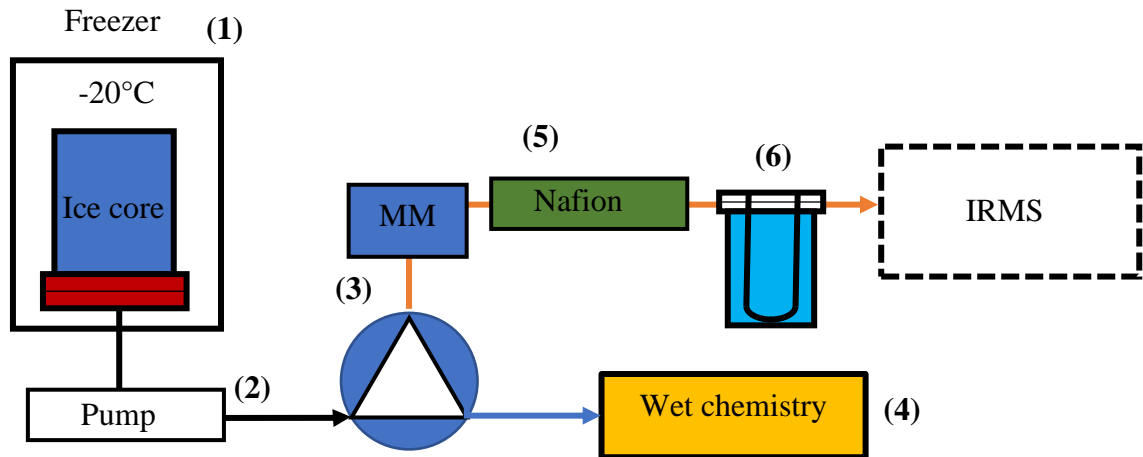


Figure 1.3: A simplified setup scheme for an example of a CFA measurement system based on this study. Dark red is the melthead. Black lines are mixed gas and liquid flows. Orange lines are gas flows and blue lines are liquid flows. MM is the Micromodule that was used for gas extraction from the sample stream.

The main advantages of this type of analysis are that the CFA system can generate results faster and that the data density is significantly higher than in discrete samples (Schüpbach et al., 2009). Furthermore, there is less transport logistics of samples necessary since it is also possible to install a CFA setup at an ice core drilling site for CH₄ concentration measurements (Schüpbach et al., 2009). This is however not relevant for $\delta^{15}\text{N}$ and $\delta^{40}\text{Ar}$ since it is not possible to bring a mass spectrometer to a drill site. Another advantage of this type of measurements is that different wet chemistry parameters and gases can be measured simultaneously and consequently less ice core sample is needed (Vladimirova, 2018).

1.8 Firn processes

The uppermost part of the ice sheet is called *firn* and consists of subsequent snow layers being compacted by their own weight (Herron and Langway, 1980). Gradually and with increasing depth and weight of snow, the snow grains transform into ice, get less porous and denser (Herron and Langway, 1980). At around 60 - 80 m (for Greenland) there is no connection to the atmosphere anymore, the firn layer ends and becomes solid ice (Schwander et al., 1993). This transition zone is called bubble close-off-depth (COD) and happens at a density of around 830kg/m^3 (ibid.).

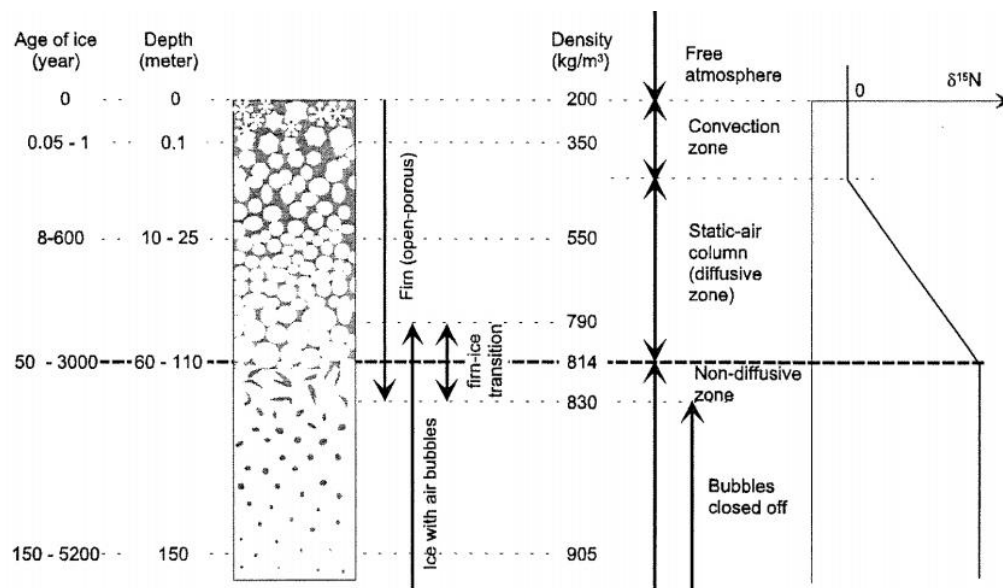


Figure 1.4: A sketch of the firn column and influence on $\delta^{15}\text{N}$ (Blunier and Schwander, 2000).

The firn column can be divided into 3 different zones as seen in Figure 1.4 above. The first zone is the convective zone where molecules can still move freely and exchange with the atmosphere. The $\delta^{15}\text{N}$ in this zone is expected to be similar to the atmosphere because of regular exchange with the atmosphere. The second zone is the diffusive zone and molecules distribute due to molecular diffusion driven by two major processes: 1) gravitational settling and 2) thermal fractionation that will be described further in chapter 1.8.1 and chapter 1.8.2 (Severinghaus et al., 1998); (Schwander, 1989)). The gravitational settling results in an increase of the $\delta^{15}\text{N}$ signal in this zone. These two processes occurring in the diffusive zone allow to reconstruct rapid temperature changes from ice core records based on measured isotopic delta values and firn modelling (Lang et al., 1999). The third zone (non-diffusive zone) is no longer influenced by surface temperatures and atmospheric exchange and the air bubbles are trapped in the ice (Blunier and Schwander, 2000). The $\delta^{15}\text{N}$ signal in this zone is assumed to stay at the level when the gas bubble was formed in the ice (ibid.).

1.8.1 Gravitational settling

Gravitational settling is the process that heavier isotopes accumulate at the bottom end of the firn column near the COD which is approximately 60 m for Dye 3 ((Schwander, 1989),(Craig et al., 1988)). The gravitational settling varies proportionally to changes in the depth of the firn column due to changes in temperature and accumulation rate (Lang et al., 1999). The lower the temperature and accumulation rate at a given location, the deeper the firn column and consequently the bigger the delta value due to gravitational settling.

The gravitational settling is given by the barometric equation according to Schwander (1989):

$$\delta_{grav} = \left[\frac{R}{R_0} - 1 \right] * 1000 = \left(e^{\left(\frac{\Delta m * g * z}{R * T} \right)} - 1 \right) * 1000 \text{ [‰]} \quad (1.5)$$

Where **R** and **R₀** are the ratios of the sample and the standard; **z** is the depth of the firn column; **Δm** is the mass difference of given isotopes; **g** is the gravitational acceleration; **R** is the gas constant; **T** is the mean firn temperature.

For example, the delta value for δ¹⁵N in an 80 m deep firn column at 236K (-37°C) will have increased by 0.4 ‰ due to gravitational settling when comparing top and bottom part of the firn (Severinghaus et al., 1998).

1.8.2 Thermal fractionation

Thermal fractionation is a result of thermal diffusion of molecules due to the temperature gradient between the surface temperature and the temperature at the bottom of the firn column (Severinghaus et al., 1998). The heavier isotopes tend to migrate towards the colder part of the firn (ibid.).

The process of thermal fractionation can be described as follows:

$$\delta_{therm} = \left[\frac{R}{R_0} - 1 \right] * 1000 = \left[\left(\frac{T_{surf}}{T_{bottom}} \right)^\alpha - 1 \right] * 1000 \text{ [‰]} \quad (1.6)$$

Where **R** and **R₀** are the isotopic ratios of the sample and the standard; **α** is the thermal diffusion factor which is dependent on the element; **T_{surf}** and **T_{bottom}** are temperatures in Kelvin.

The thermal diffusion factor **α** for the isotopic pair of ¹⁵N-¹⁴N – ¹⁴N₂ at 298K (25°C) is 0.0065 and results in an enrichment by 0.2 ‰ when comparing the cold part (298K) with the bottom part (308K, 35°C) of a diffusive column (Severinghaus et al., 1998).

Argon and nitrogen measurements from the same ice core section allow the separation of the two effects (gravitational settling and thermal fractionation) because argon is roughly only half as sensitive to thermal fractionation as nitrogen (Severinghaus et al., 1998).

1.9 Age difference between ice and gases

Gas bubbles trapped in the ice are always younger than the surrounding ice because gas diffusion is still possible throughout the firn column until it is closed off completely from the atmosphere through densification and compaction (Schwander and Stauffer, 1984). The climatic signal is stored first in the ice (e.g. ^{18}O of the water molecules) and then can be observed in the gases at a shallower depth (ibid.). This depth difference is called delta depth (Δdepth) and allows to calculate the depth difference for specific climatic events (e.g. D-O events). By doing this, it is possible to calculate the delta age (Δage) and consequently to translate the ice age time scale to a gas age time scale as done by Janani Venkatesh for Dye 3. The general process is described in chapter 3.14.2.

2 Literature Review

2.1 Discrete argon and nitrogen measurements from ice cores

A lot of research has been conducted to obtain nitrogen and argon data from ice cores over the past decades using mostly discrete and more recently also CFA measurement techniques.

Sowers et al. (1989) measured 13 discrete samples from different ice core sites in Greenland and Antarctica for $\delta^{15}\text{N}$, $\delta\text{O}_2/\text{Ar}$, $\delta^{18}\text{O}$. The samples cover a time period younger than 2000 years before present (BP) and were cut into 2 x 2 cm ice cubes, put into an extraction vessel and were melted with a wet extraction technique using mass spectrometry (Sowers et al., 1989). The precision of the measurements was $\pm 0.02\text{‰}$ for $\delta^{15}\text{N}$ which is the only parameter measured relevant for this study (ibid.).

Severinghaus et al. (2003) developed a measurement setup to analyse $\delta^{40}\text{Ar}$ and krypton/argon elemental ratios from ice cores. The discrete samples were cut into 9 cm long pieces that were melted in a an extraction vessel and passed through a water trap, a getter inside an oven at 900°C to take out N_2 and O_2 before entering the mass spectrometer (Severinghaus et al., 2003). The measurement process is relatively complicated, and each sample needs to be passed through the whole system individually, but the precision is high ($\pm 0.012\text{‰}$) and therefore well reproducible (ibid.).

Kindler et al. (2014) analysed and partly measured $\delta^{15}\text{N}$ from the NGRIP ice core. Data from the Holocene back to D-O event 17 was obtained with an on-line measurement system from (Huber and Leuenberger, 2004), which is described in detail below in chapter 3.3. D-O events 18-25 were measured with a discrete sampling method of melt-refreeze technique (Kindler et al., 2014). 384 samples were analysed with sample lengths between 10 and 25 cm each (ibid.). The uncertainties for the on-line (CFA) system were $\pm 0.02\text{‰}$ and for the discrete sampling $\pm 0.006\text{‰}$ (ibid.).

2.2 Combined argon and nitrogen measurements

Kobashi et al. (2008) were the first to develop a discrete measurement system for simultaneous $\delta^{40}\text{Ar}$, $\delta^{15}\text{N}$ and the elemental ratio of $\delta\text{Ar}/\text{N}_2$ seen in Figure 2.1. These combined argon and nitrogen measurements result in more time efficient measurements that additionally consumed less sample (Kobashi et al., 2008). The samples were between 10 and 30 cm long depending on the depth, the climatic transitions analysed and the resolution needed (Kobashi et al., 2008). 1006 samples were analysed corresponding to 670 different depths (Kobashi et al., 2008). The sample inside a vessel was melted by hot water, then passed through 2 cryogenic traps (-100°C and -196°C respectively), a heated copper mesh (500°C) taking out ^{18}O to avoid interference with ^{36}Ar measurements and finally passed another cryogenic trap (-196°C) (Kobashi et al., 2008). The precision for $\delta^{15}\text{N}$ measurements lies between 0.003‰ to 0.005‰ , the precision for $\delta^{40}\text{Ar}$ is $0.1 - 0.2\text{‰}$ (Kobashi et al., 2008).

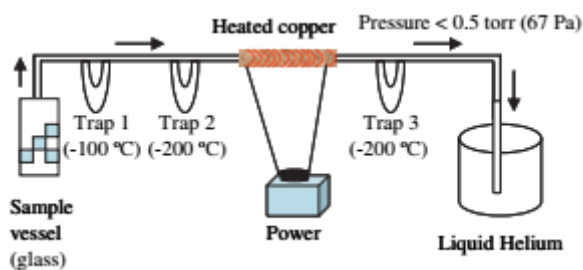


Figure 2.1: An example of a discrete measurement system based on Kobashi et al., (2008).

2.3 CFA measurements

During the past three decades, continuous flow analysis (CFA) measurement setups were developed which enable a higher resolution than discrete sampling obtained in a shorter time frame (Schüpbach et al., 2009). The first ones were developed by Fuhrer et al., (1993), Sigg et al., (1994) and Röthlisberger et al., (2000). The CFA measurement setup allowed a resolution of 1 cm and measurements of 20 m of ice in one day, which was a huge acceleration compared to conventional discrete sampling (Röthlisberger et al., 2000). This method was designed to measure only wet chemistry parameters (and no gases) such as sodium, nitrate, sulfate, electrolytical conductivity, ammonium, calcium, hydrogen peroxide and formaldehyde (Röthlisberger et al., 2000).

Huber and Leuenberger established in 2003 a CFA setup to measure $\delta^{15}\text{N}$ and $\delta^{36}\text{Ar}$ using mass spectrometry. A degassing unit was used to separate the gas and liquid sample stream flushed with helium (Huber and Leuenberger, 2004). The sample passed a Nafion membrane which dried the sample flow and a cryogenic trap to freeze out heavy molecules like CO_2 before entering the mass spectrometer (ibid.). The resolution was approximately 3 cm and uncertainty for $\delta^{15}\text{N}$ was $\pm < 0.02\text{‰}$ (ibid.) and for $\delta^{36}\text{Ar}$ $\pm 0.2\text{-}0.3\text{‰}$. The setup will be described in detail in the methodology section and will be compared to the PICE 2019 CFA setup to obtain the data for this thesis.

Following that, CFA was mostly used for analysis of past CH_4 concentrations from ice cores. Schüpbach et al., (2009) developed a method for measurements of CH_4 concentrations in the field. The sample passes through a debubbler, a Nafion membrane and a cryotrap to a gas chromatograph to get measured (Schüpbach et al., 2009). Wet chemistry parameters and gas measurements were performed simultaneously (ibid.). The resolution of this setup for the measurements is in the order of 15 cm and the uncertainty is ± 15 ppb which was comparable to discrete measurements at that point of time (ibid.).

Stowasser et al. (2012) developed a CFA system that used a Picarro Wavelength Scanned-Cavity Ring Down Spectrometer to measure CH_4 concentrations in air bubbles from ice cores. A combination of a debubbler and a MicroModule has been used to separate gas and liquid stream (Stowasser et al., 2012). The sample passed then a Nafion membrane which takes residual humidity out before entering the modified Picarro WS-CRDS that measured the CH_4 concentration (ibid.). Stable water isotopes ($^{18}\text{O}_{\text{ice}}$) were measured

simultaneously (ibid.). The resolution of this system was approximately 5 cm and precision was ± 0.8 ppb (ibid.).

Vladimirova (2018) used a CFA system for simultaneous CH₄ and wet chemistry parameters at the Center for Ice and Climate (CIC) that is now PICE. The system used a debubbler and a modified Picarro G1101-i Wavelength Scanned-Cavity Ring Down Spectrometer to measure the CH₄ concentration from the air bubbles in the ice (Vladimirova, 2018). The uncertainty for this system is ± 10 ppb (ibid.).

The current state of research in the field of the ice core studies is to combine CFA of wet chemistry parameters with gas measurements of CH₄ and nitrogen and argon isotopes. The measurement setup used for this thesis will be described in the next chapter.

3 Methodology

A large part of this thesis project was dedicated to the development of the CFA measurement system, especially regarding the isotope measurements. The existing PICE CFA setup was modified to be able to measure not only wet chemistry parameters and CH₄ concentrations but also the argon and nitrogen isotopes from ice cores simultaneously (Baldtzer Liisberg, 2020). To get better argon isotopic CFA measurements, Huber and Leuenberger (2004) suggested to use an oxygen removal system. In this setup, the oxygen extraction is achieved with a perovskite membrane sitting inside an oven heated to 850°C.

In this chapter, the PICE 2019 CFA setup and the sample measurement process are illustrated followed by an overview of the development challenges. Moreover, the PICE 2019 CFA system is compared to the on-line measurement system of Huber and Leuenberger (2004). Then the perovskite membrane that was used for oxygen removal and its properties are described and the correlations between oven temperature, BPR pressure setpoint, helium flow and resulting oxygen removal are presented. Following that, a description of the preparation of the ice cores, calibration runs, and sample measurements are given followed by an overview of data acquisition times. Subsequently, the data processing is presented, and the corrections applied to the raw data including eventual removal of lab air contamination to get the final data are shown. Furthermore, the error calculation is described. Lastly, the process of depth and age assignment to the data is shown.

3.1 General description of the CFA setup

The detailed methodology for the PICE CFA system was described by Stowasser et al. (2012) and Vladimirova (2018). A short summary of this system, with a focus on the gas extraction component is given in this section.

The ice core CFA stick was mounted vertically top-down in a plastic frame above the melthead (i.e. the “youngest” ice section got melted first) which had a temperature of approximately 50°C sitting inside a freezer at -20°C. An automatic encoder registered the height of the ice stick while melting which was used for the depth and age assignment later on (described in chapter 3.14). The melthead temperature resulted in a meltspeed of 4 to 4.5 cm of ice per minute.

From the melthead, the combined gas and liquid flow was pumped away with a peristaltic pump at 23 ml/min. After having passed the debubbler, 3-4 ml/min of the sample were taken away for

dust measurements. The majority of the sample continued through a 20 μm dust filter to prevent damage and clogging of the MicroModule gas extraction unit. This MicroModule unit (Liqui-Cel MM-0.75X1 Series Membrane Contactor, 3M) separated the gas from the liquid in the sample stream. Afterwards, the liquid flow passed on to wet chemistry measurements. The extracted gas moved on driven by a pressure difference from atmospheric pressure (1 bar) towards 300 mbar (EL-PRESS P-702CV, Bronkhorst) before it was split for methane and isotope measurements with a T-piece.

The isotope measurement flow (0.15 ml/min) passed on to a Nafion membrane (TT 30, Perma Pure) which dehumidified the gas flow. A liquid nitrogen trap froze out the heavy molecules such as CO_2 and N_2O , and finally the perovskite membrane inside the oven (850°C) removed O_2 molecules from the sample stream. The perovskite membrane (and its associated oven setup) is a novel addition to the CFA setup and described in more details below. The speed of the gas stream was controlled with a Bronkhorst back pressure regulator (BPR) at a setpoint of 200 mbar. Finally, the sample entered the mass spectrometer through a capillary (ID: 100 μm , L: 1,670 mm). The capillary was used to introduce a small amount of sample and prevent damage to the ion detector of the IRMS.

The masses of nitrogen (28 and 29), argon (36 and 40) and the elemental ratio of argon/nitrogen (40/28) were measured simultaneously while the ice core was melted continuously. Due to constraints of the mass spectrometer cups, it was not possible to measure mass 38 of argon simultaneously with the other isotopes (Thermo Fisher Scientific, n.d.). However, because of its low natural abundance (0.0632%), argon 38 is neglectable for the purpose of this evaluation (Krebs, 2006). Mass 32 of oxygen and mass 44, 45 and 46 of CO_2 were measured additionally, to confirm that the liquid nitrogen trap and the perovskite membrane worked as expected.

The IRMS allows standard calibrations through the dual inlet function. A mix of pure nitrogen and argon matching the atmospheric (e.g. laboratory air) elemental ratio was used as a dynamically mixed standard to compare the sample measurements with laboratory air (chapter 3.11). The flow of nitrogen was approximately 10 ml/min and of argon was 0.127 ml/min (Baldtzer Liisberg, 2020). The pressure towards the standard inlet of the IRMS was regulated with a forward pressure controller (EL-PRESS P-602CV, Bronkhorst). A FPR setpoint to 145 mbar was found to match the lab air intensities closely. The fraction of the dynamically mixed standard that was not passed through the FPR was released into the laboratory (vent). Using a standard capillary (ID 100 μm , 368 mm) alone did not ensure a constant pressure of 145 mbar

at FPR, consequently the FPR was additionally connected to a vacuum pump to increase the gas flow. The standard capillary was pushed upstream into the T-piece so that the pump did not influence the standard measurements. The standard entered the IRMS through a capillary corresponding to a flow of 0.02 ml/min.

The standard line setup can be seen in Figure 3.1 below.

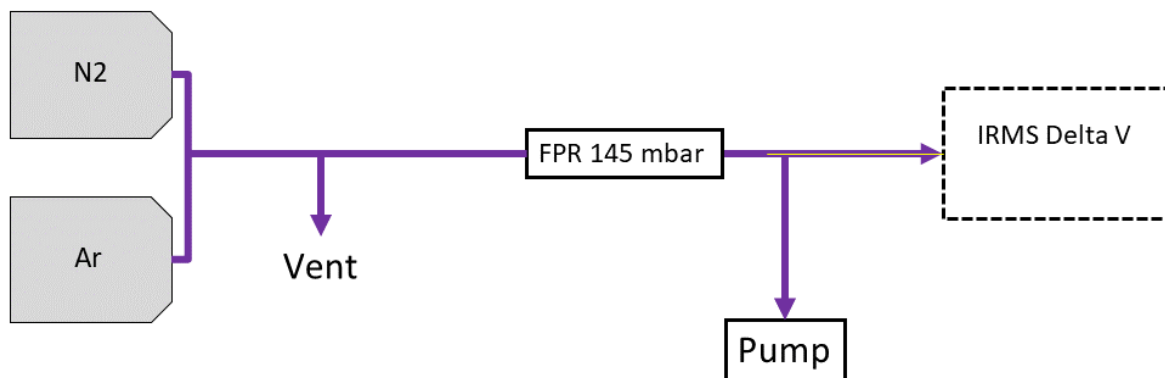


Figure 3.1: Zoom on the standard line setup: The flow passed to the IRMS was controlled by the forward pressure controller at 145 mbar. The standard capillary (yellow) was passed through the T-piece so that it reached the upstream end of it and could measure the standard.

The lab air was used to bind the measurements to an absolute scale and the dynamically mixed standard was mainly used for potentially necessary drift corrections.

The full PICE 2019 combined CFA setup is shown in Figure 3.2.

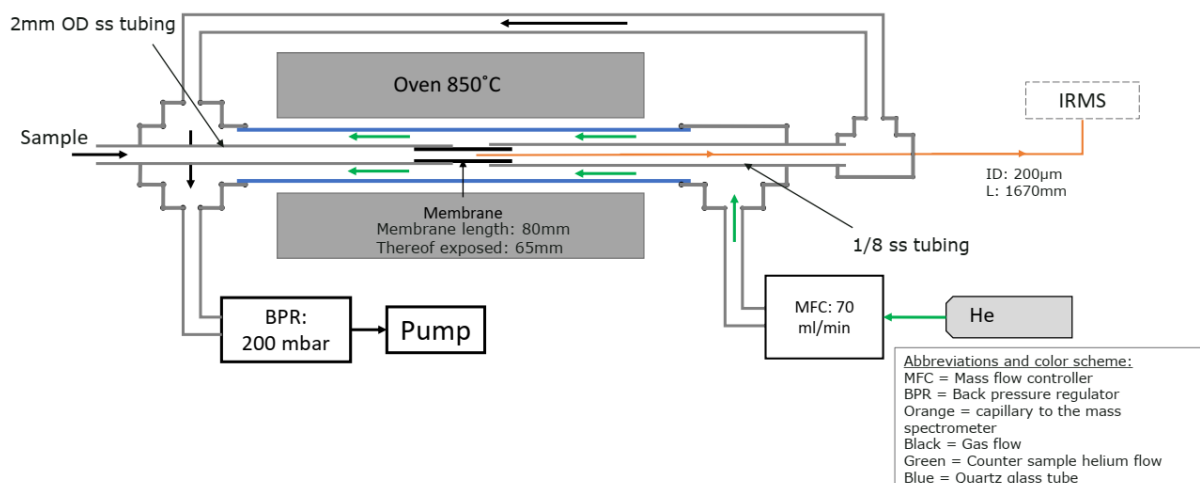


Figure 3.3: Zoom on the oven setup with the BCFZ membrane that extracted the oxygen from the sample stream.

Figure 3.3 shows a close-up on the oven setup to illustrate the sample treatment inside the oven. The sample passed from the Nafion membrane and cryogenic trap (liquid nitrogen trap at -196°C) to the oven heated to 850°C . The pressure was maintained at 200 mbar for the whole oven system. The 2 mm OD stainless steel tubing sat inside a quartz glass tube and the membrane piece was sealed to the upstream end from which the sample arrived. The downstream end was open and the sample capillary leading to the IRMS was pushed 2 cm inside the membrane. A counter sample helium flow of 70 ml/min transported the extracted oxygen away creating a high partial pressure across the membrane. The helium is introduced through the glass tube in counter-sample flow direction so that the extracted oxygen could be carried away.

3.2 Overview over the development challenges

The focus of this master thesis is on the development of the isotope measurement system that was attached to the rest of the CFA system. It is important to keep in mind that the whole system has been modified and improved. Numerous challenges were encountered and overcome during this development process. This overview focuses only on the isotope part of the setup.

In order to get the highest possible oxygen removal, a maximum partial pressure across the membrane is needed (Liang et al., 2010). Two different options were available for the perovskite membrane and oven setup. The first option relied on a vacuum to create a partial pressure gradient across the membrane and the second option used a counter helium flow to transport the extracted oxygen away from the sample stream.

In the beginning, we tried to implement the vacuum option, since it was supposedly more efficient in terms of removal due to a higher partial pressure gradient (300 mbar to vacuum) and less expensive because there was no helium consumption involved. The setup overview for this solution can be seen in Appendix 1. After several unsuccessful attempts, it proved to be impossible to seal the membrane to the stainless-steel tubing on both ends to the degree needed e.g. gas leak tight. Consequently, the open, counter sample helium flow option was implemented. A conductor gold paste (Heraeus type C5754 B) was used as the sealant. The sealing of the membrane turned out to be challenging because it is very fragile and therefore easily breakable, especially when assembling or disassembling the setup.

Two ovens were available with different temperature ranges and sizes. We initially tried to use the smaller oven because a smaller system was supposedly more efficient and easier to handle. It turned out that the smaller oven could only heat up to 600°C, so it could not reach the temperature range needed for optimal oxygen removal (850 to 950°C). The bigger oven was tested later, and the removal seemed to work from around 600 to 950°C. However, in one of the first attempts, the glass melted due to the high temperatures and destroyed the membrane inside. It was assumed beforehand that the glass tube was quartz glass; however it turned out to be borosilicate glass with a melting point of 820°C (Weissler and Carlson, 1979). Consequently, a special quartz glass tube was ordered and used afterwards which was able to withstand higher temperatures up to 1,600°C (Technical Glass Products Inc., n.d.).

Another challenge was that the analogue flow controllers for the counter-sample helium flow did not deliver a stable flow after having been set to a specific setpoint manually. As a result, they were changed to two digital mass flow controllers (GE50 with 50 SCCM + GE50 with

20 SCCM, MKS) which resulted in a more constant flow. The combined helium flow was 70 ml/min provided by two combined MFCs with 50 ml/min and 20 ml/min each.

With these challenges solved, we were finally able to setup and measure with the PICE 2019 CFA system.

3.3 Comparison of the Huber et al. setup the PICE 2019 CFA setup

Huber and Leuenberger (2004) developed an online measurement system (CFA system) similar to the one used to obtain the data from the Dye 3 ice core with the PICE 2019 CFA system. The main difference is the degassing unit used, which was flushed with helium in the Huber setup and the PICE 2019 setup used a MicroModule (Liqui-Cel MM-0.75X1 Series Membrane Contactor, 3M) and a debubbler instead (Huber and Leuenberger, 2004). The sample and reference received the same treatment in the Huber setup, meaning that both flows travel through the degassing unit, the Nafion membrane, the cryogenic trap and reached the IRMS through an open split (ibid.). In the PICE 2019 setup, the reference flow was introduced directly into the IRMS instead via an open split. In the Huber setup, no removal of oxygen was implemented, but it was suggested that this might lead to improved $\delta^{36}\text{Ar}$ measurements due to reduced interference with a clumped molecule of $^{18}\text{O}_2$ (ibid.). Furthermore, the PICE 2019 system measured wet chemistry parameters as well as CH_4 concentration continuously while the Huber setup focused only on gases $\delta^{15}\text{N}$, $\delta^{18}\text{O}$, $\delta^{36}\text{Ar}$ and elemental ratios of $\delta\text{Ar}/\text{O}_2$, $\delta\text{O}_2/\text{N}_2$ and $\delta\text{Ar}/\text{N}_2$ (ibid.). Figure 3.4 below shows the CFA measurement setup developed by Huber and Leuenberger (2004).

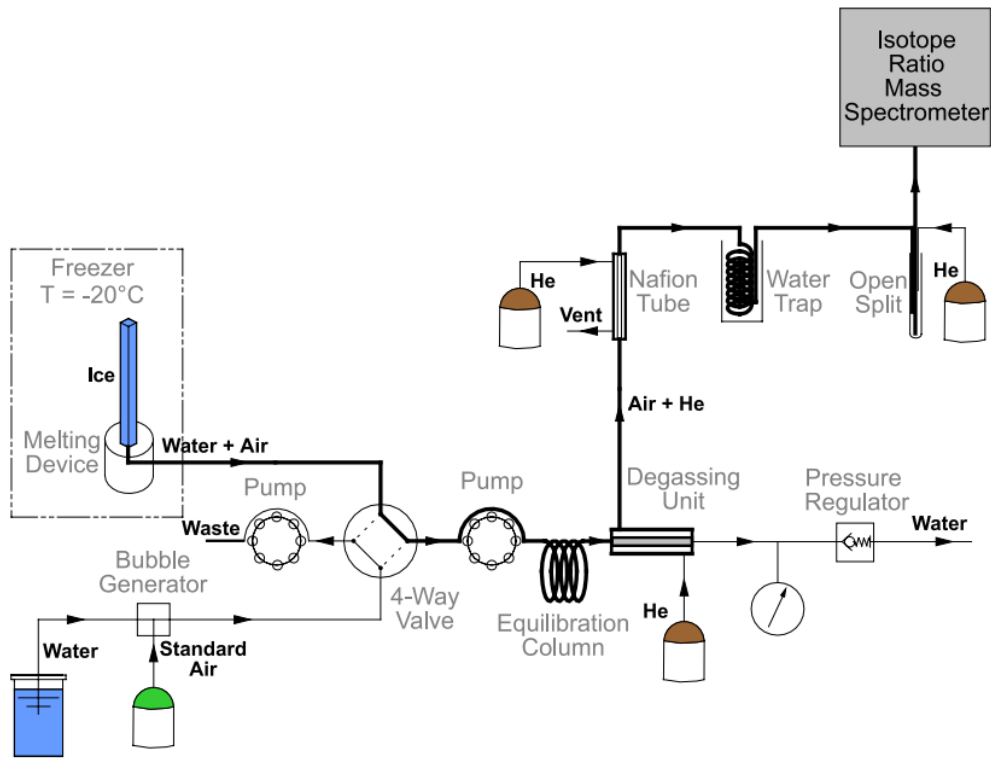


Figure 3.4: Scheme of the on-line measurement system according to Huber and Leuenberger, (2004).

3.4 The perovskite membrane

A perovskite hollow fiber membrane ($\text{BaCO}_x\text{Fe}_y\text{Zr}_{1-x-y}\text{O}_{3-\delta}$, BCFZ) was used to extract oxygen from the sample stream in order to get more accurate argon and nitrogen isotopic measurements. It is tubular in shape and has 1.1 mm outer diameter (OD) and 0.8 mm inner diameter (ID) (Liang et al., 2010). The membrane works with the process of permeation for oxygen (e.g. it lets only the oxygen pass through with the help of molecular diffusion) at high temperatures from 500°C to 1000°C (ibid.). The membrane acts as a barrier for all other gases (ibid.). The optimal temperature range for a maximum removal is from 850°C to 950°C which allows a removal of up to 99.9% of oxygen (ibid.). A high partial pressure gradient across the perovskite membrane is required for high levels of oxygen removal (ibid.).

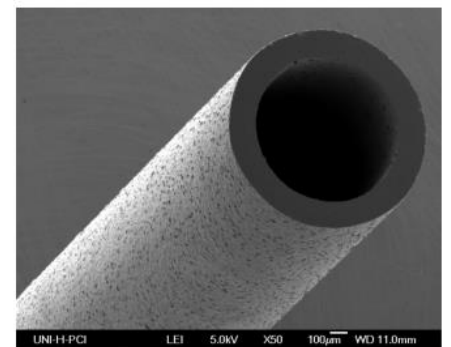


Figure 3.5: Picture of the BCFZ hollow fiber membrane under a micrograph (Liang, 2010).

3.5 Oxygen removal efficiency testing with laboratory air

As a proof of concept of the oxygen removal system, three different parameters were varied to see how they affect the oxygen removal from laboratory air. Three tests were performed in order to evaluate the correlation between oven temperature, counter sample helium flow, BPR pressure setpoint (e.g. the sample flow into the IRMS) on the oxygen removal and finally being able to choose the most efficient setting for the sample measurements. Oven temperature, helium flow and pressure setpoint were varied, and the results shown below were obtained.

A three-port valve in front of the oven was used to perform the oxygen removal tests. The tests were done without passing the Nafion membrane and cryogenic trap. A capillary (ID: 50 μm , L:165 mm) was used to restrict the incoming laboratory air flow to the oven.

An oxygen removal test with varying oven temperatures, a BPR setpoint of 150 mbar for the oven system and a helium flow of 50 ml/min gave the results seen in Figure 3.6:

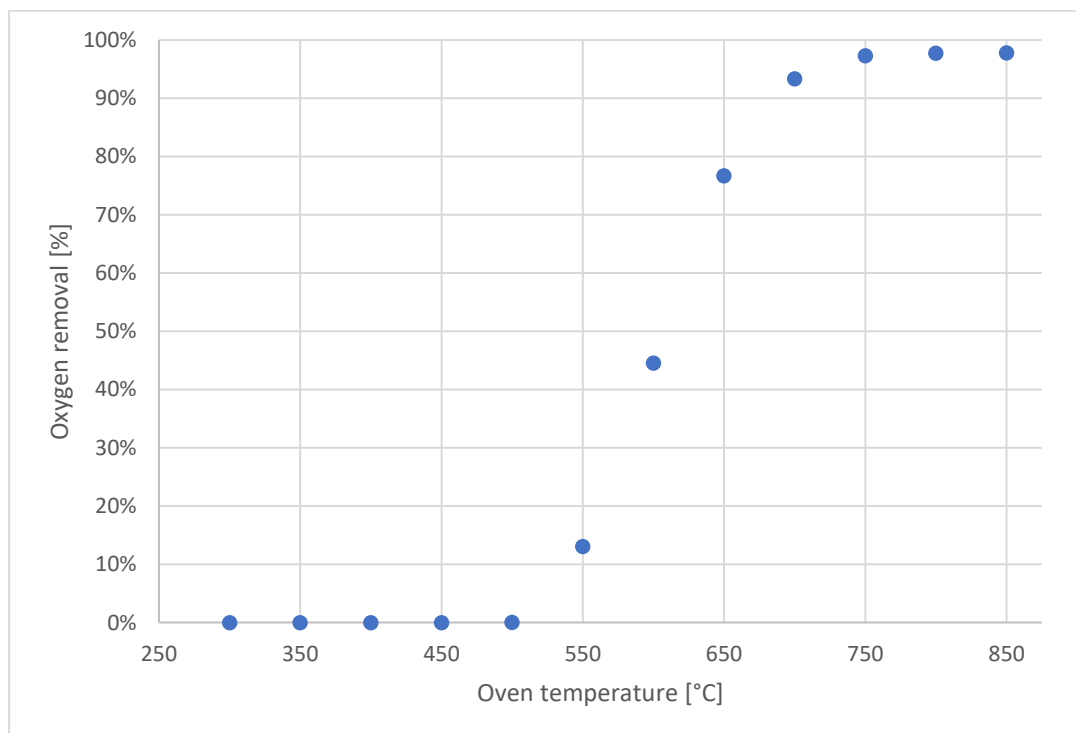


Figure 3.6: Graph showing the oxygen removal dependency on the oven temperature. The temperature was increased in 50°C steps from 250°C to 850°C.

A higher oven temperature resulted in a higher removal rate. The biggest increase in removal is between 500°C and 700 °C. The removal stabilizes around 97.8% at an oven temperature of 850°C. Unfortunately, tests with higher temperatures were not performed, but it seems to stabilize around 98% based on the data obtained until 850°C.

A higher BPR setpoint leads to a lower sample flow through the membrane due to a smaller pressure gradient from atmospheric pressure but a higher flow towards the IRMS. The gas stays a slightly longer time inside the membrane, lowering the partial pressure on outside of the membrane and this results in a higher oxygen removal. Furthermore, a higher BPR setpoint leads to more motion due to a higher density so that more oxygen is removed through the membrane.

To test this assumption, an oxygen removal test with varying BPR setpoints, an oven temperature set to 700 °C and a constant helium flow of 60 ml/min was done and resulted in the data seen in Figure 3.7:

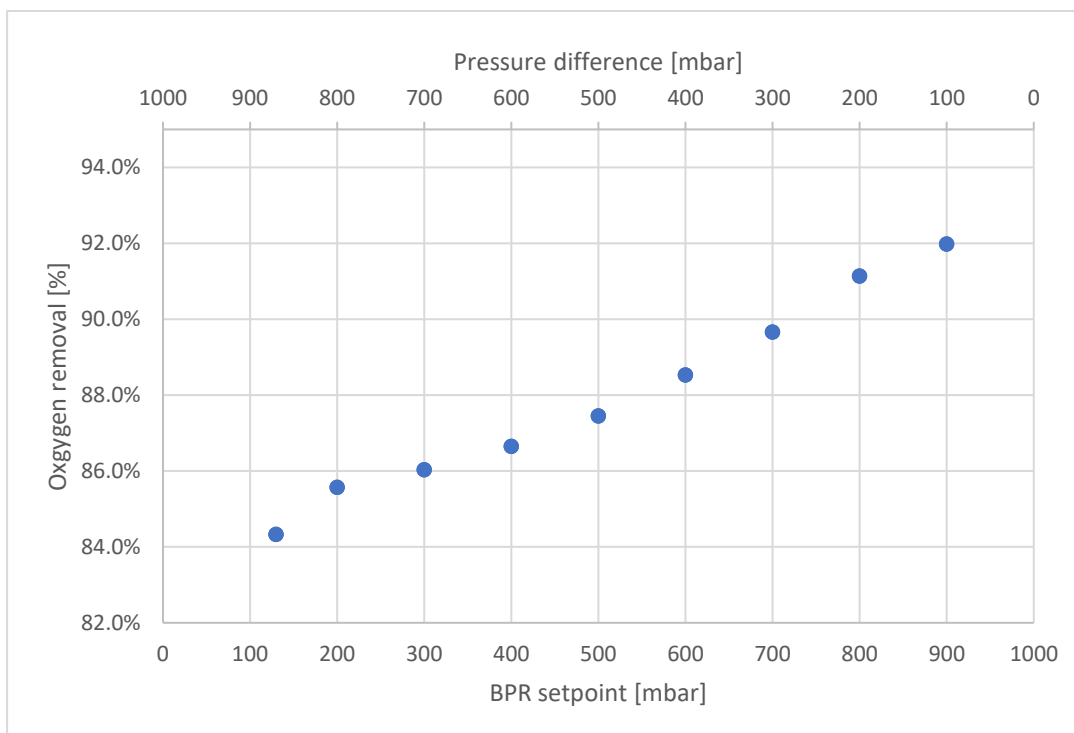


Figure 3.7: Graph showing the oxygen removal dependency on the BPR setpoint of the oven setup. The pressure setpoints were varied between 130 mbar and 900 mbar. Additionally, the pressure difference between total atmospheric pressure and BPR setpoint is shown (1000 mbar – pressure setpoint).

The smaller the pressure difference between total atmospheric pressure and the BPR setpoint of the oven setup, the higher are the removal rates of the membrane. To summarize, the slower the incoming gas flow passes through the membrane and therefore the longer the residence time inside the membrane, the higher is the removal and potentially lower the partial pressure on the

outside of the membrane. A BPR setpoint of 900 mbar (e.g. a pressure difference of only 100 mbar compared to atmospheric pressure) resulted in a removal of 92% as compared to approximately 84% at a BPR setpoint of 130 mbar (a pressure difference of 870 mbar).

An oxygen removal test with a varying helium flow, an oven temperature set to 750 °C and a pressure setpoint of 200 mbar gave the results seen in Figure 3.8:

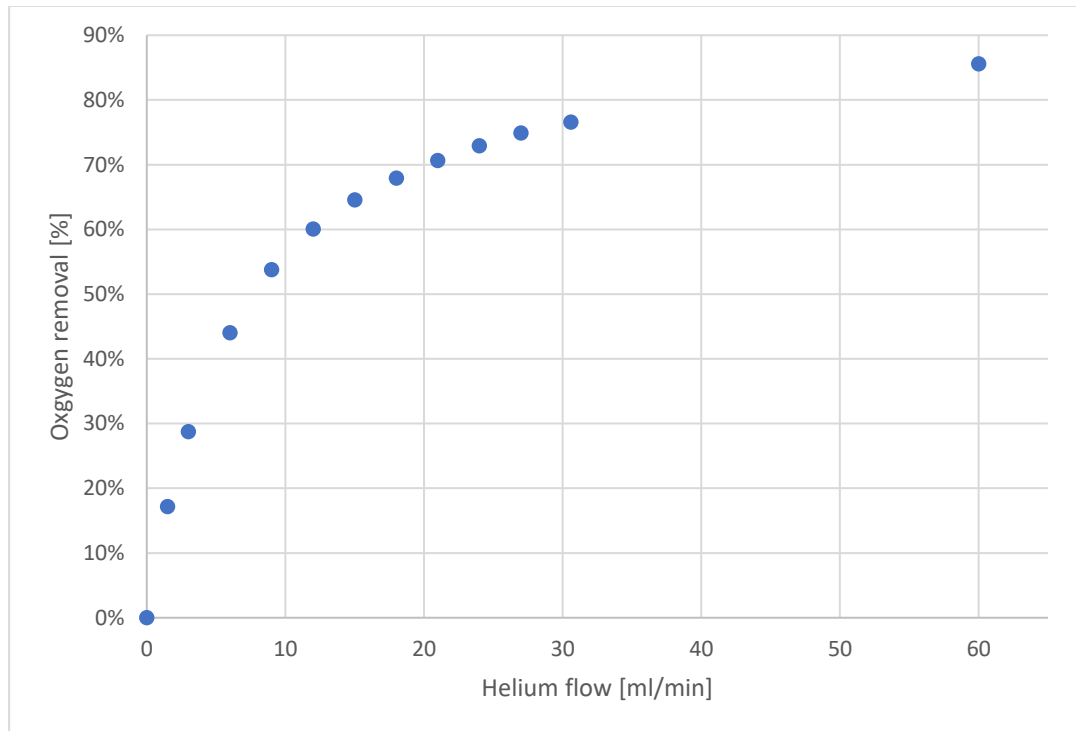


Figure 3.8: Graph showing the oxygen removal dependency on the counter-sample helium flow.

A higher helium flow is positively correlated to a higher removal rate of oxygen. The measurements until ~30 ml/min have been performed on the same day (26/09/2019), the one with 60 ml/min was done on the 29/09/2019. A flow of around 45 ml/min could have confirmed the observed trend, which was unfortunately not done.

The correlation tests have not been performed under the same conditions (more than one factor has been changed for each test), consequently, it is not possible to compare them directly with each other, but they give indications on relative dependencies between the three factors on the oxygen removal: oven temperature, BPR setpoint and helium flow.

In the end, two digital mass flow controllers have been available for the setup with a combined helium flow of 70 ml/min. It was decided to heat up the oven only to 850°C to reduce the pressure on the equipment. The pressure setpoint for the oven setup was decided to be at 200 mbar which created a pressure difference of 100 mbar from the previous BPR at the

MicroModule set to 300 mbar. Higher temperatures, an increased helium flow and a smaller pressure gradient would likely have resulted in a slightly higher oxygen removal which could be taken into consideration for future work.

3.6 Ice preparation

The ice core samples were prepared in a working freezer next to the CFA laboratory at -20°C before the actual measurement process. The samples were first cut into CFA sticks having a cross section of 3.5*3.5 cm by using a clean bandsaw. Then, breaks in the ice core were removed to avoid potential contamination of drilling fluid for the wet chemistry measurements. Artificial ice on the surface of the ice core due to the long storage in the freezer (approximately 40 years since drilling) was removed as well. Afterwards, the breaks were aligned using a trimmer and/or a clean bandsaw to avoid contamination from modern air for the gas measurements. Breaks and missing pieces were noted down manually and were accounted for during the depth assignment afterwards. In the end of the process, the 1 m long ice sticks were put in plastic frames and stored in the working freezer until shortly before the sample measurements. The plastic frame with the CFA stick inside was mounted vertically inside the freezer and then was melted to obtain the data.

3.7 Calibration runs

In the morning and evening of each measurement day, calibration runs were performed for the gas measurements. First, the CH₄ calibrations were done, because there was no argon in the methane standard gas and therefore, it was necessary to do separate calibrations.

For the isotopes, the nitrogen and argon mix was calibrated against laboratory air. The calibration procedure was carried out in Dual-Inlet mode (and automated in *Isodat* (the IRMS software) as a method script):

1. The predelay for background intensity measurements with both inlet valves closed was 30 seconds.
2. 5 cycles (switching between laboratory air and standard gas mix (pure nitrogen and argon gas mix)) were done. The integration time was 20 seconds for each cycle.
3. The results have been averaged for all cycles and were combined given automatically as delta values and isotopic ratios. Additionally, standard deviation and standard error were calculated automatically. The background intensity has been subtracted automatically from the data. If necessary, the calibration was repeated, so that standard

error and standard deviation were as close to zero as possible. The mean standard deviation for $\delta^{15}\text{N}$ was 0.014 and for $\delta^{40}\text{Ar}$ 0.115.

In total, 13 calibration runs were carried out, 3 of those were done on the 5th November 2019 (morning, lunch break and evening calibration). For the rest of the days, only two calibration runs were done (in the morning and evening).

3.8 Sample measurements

The sample measurements were done in continuous flow mode of the IRMS. The data acquisition was started when the MQ ice cubes (gas free ice with purified water and a length of 7 cm; 2 cubes of 3.5 cm stacked on top of each other) were put on the melthead.

The inlet valves were closed for the first 30 seconds of the measurements to measure the background which is why the signal increases rapidly towards reference intensity levels seen in orange. 2 minutes of reference (nitrogen and argon gas mix) are followed by the sample measurements with varying durations (depending on length of the ice core bags, missing pieces and potential analytical challenges) and then again followed by at least two minutes of reference measurements in the end of the run (normally longer than 2 minutes). This allows for a potential drift correction to detrend the data, if necessary.

In general, the sample measurements followed the scheme for each mass measured seen in Figure 3.9:

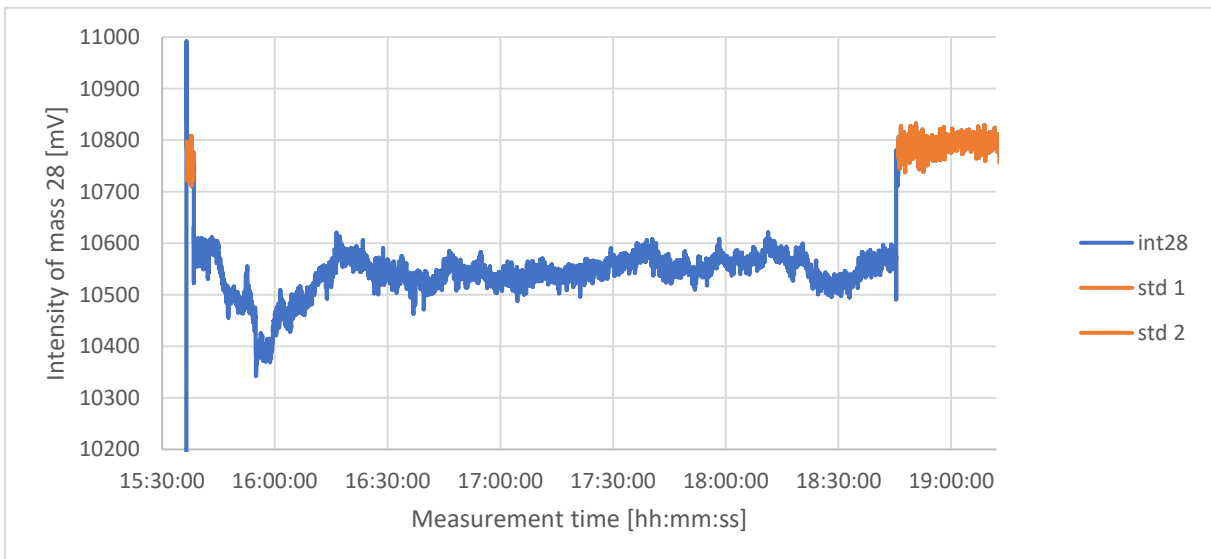


Figure 3.9: Graph showing the intensity of nitrogen (mass 28) during the measurement run of the 5th November 2019.

The intensities of mass 28 are raw as they come out of the mass spectrometer. This means that they are not corrected for background, pressure imbalance, chemical slope and solubility effect. The data was not smoothed and is plotted only on a measurement time scale and not on a depth or age scale.

The linear drift correction based on the reference period before and after the actual measurements was not used (Baldtzer Liisberg, 2020), as it introduced an artificial trend into the data which was judged not to be realistic.

3.9 Overview of data acquisition times

Bag number	Date	Start time	End time	Start depth	End depth	Melt/run	Isotope data?
1704	29 th Oct	14:22	17:21	1753.53	1761.52	7.99	No
1712	30 th Oct	09:42	12:51	1761.54	1769.53	8.00	No
1720	30 th Oct	14:21	18:23	1769.53	1779.45	9.92	No
1730	31 st Oct	11:36	14:30	1779.47	1787.47	8.00	Yes
1738	31 st Oct	16:11	19:19	1787.79	1800.38	12.59	Yes
1752	04 th Nov	11:50	15:31	1801.99	1820.40	18.41	Yes
1816	04 th Nov	17:45	21:00	1865.32	1874.31	8.99	Yes
1825	05 th Nov	09:39	10:35	1874.31	1877.22	2.91	Yes
1828	05 th Nov	10:53	12:06	1877.31	1880.30	2.99	Yes
1831	05 th Nov	12:39	13:41	1880.30	1883.27	2.97	Yes
1834	05 th Nov	15:41	18:43	1883.30	1892.33	9.03	Yes
1843	06 th Nov	09:46	13:08	1892.33	1902.33	10.00	Yes
1853	06 th Nov	15:08	18:23	1902.34	1911.27	8.93	Yes
1862	07 th Nov	09:39	10:30	1911.52	1914.32	2.80	Yes
1865	07 th Nov	10:55	12:19	1914.38	1918.33	3.95	Yes
				Total meters melted*		117.47	

Table 3.1: Overview of the data acquisition times and total meters melted. *The total meters melted are based on the finalized depth assignment and therefore include missing parts and pieces that were too small for the gas CFA (<3.5x3.5 cm in cross-section). The actual melted sample from Dye 3 was approximately 108 m.

In the beginning of the Dye 3 measurement campaign, it was still necessary to improve and adapt the isotope part of the CFA setup and therefore, no data was acquired on the 29th October

2019. The data from the 30th October 2019 is offset by +43‰ in terms of delta values for $\delta^{15}\text{N}$ (and then slowly declined over time), therefore it has not been processed, corrected and taken into further consideration for this study. The total meters melted of 117.47 m are based on the theoretical length assignment which includes missing pieces or pieces that were smaller than 3.5x3.5 cm in cross section. The actual length excluding those missing sections was approximately 108 m.

3.10 Data processing

The sample data was collected in continuous mode and gave the raw intensities (m/z value [mV]) for masses 28, 29, 30, 31, 32, 36, 40, 44, 45 and 46. The lab air standard calibration runs were done in the morning and evening of a measuring day in dual inlet mode. A matlab script (Appendix 2-4) was used to assign depth to the measurements and apply the necessary corrections (background, pressure imbalance, chemical slope and solubility effect) to obtain the final dataset.

The following procedure was carried out for each measurement run to obtain the final data.

1. The raw sample measurement data was exported from the Thermo Fisher software “Acquisition” in one ASCII file per measurement run.
2. An average of the standard calibration runs of laboratory air against nitrogen/argon mix (excluding the 31st and 4th because they were unstable) was established, which - in combination with the daily calibrations - gave relative daily air calibration values in terms of isotopic ratios, delta values, standard deviation and standard errors. The morning and evening calibrations were averaged. This relative daily air standard was the input for the matlab script for the daily ratios, daily offsets and uncertainties as seen in Table 3.2.

Date	Daily ratio			Daily offset (‰)			Uncertainty (‰)		
	r_{29}	r_{36}	r_{Ar/N_2}	$\delta^{29}\text{N}$	$\delta^{36}\text{Ar}$	$\delta\text{Ar}/\text{N}_2$	$\delta^{29}\text{N}$	$\delta^{36}\text{Ar}$	$\delta\text{Ar}/\text{N}_2$
31-Oct	0.740291	0.321742	0.846356	-0.007	0.95	2.57	0.007	0.06	0.2
04-Nov	0.740093	0.323380	0.832760	-0.023	7.53	-12.21	0.015	0.14	0.4
05-Nov*	0.740174	0.320725	0.841558	0.114	-0.65	-1.63	0.013	0.12	0.3
05-Nov**	0.740117	0.320564	0.841625	0.020	-1.24	-1.63	0.012	0.11	0.2
06-Nov	0.740061	0.320241	0.843527	-0.072	-2.35	0.54	0.011	0.09	0.2
07-Nov	0.740007	0.319905	0.844153	-0.031	-3.07	1.35	0.006	0.09	0.2

Table 3.2: Daily ratio, daily offset and uncertainty of $\delta^{29}\text{N}$, $\delta^{40}\text{Ar}$ and $\delta\text{Ar}/\text{N}_2$ following Baldtzer Liisberg (2020). For the 5th November two averages were generated, one for the morning run (*) and one for the afternoon run (**).

3. The isotopic sample measurements and the depth-assigned CH₄ data at the MicroModule were matched taking into account a constant delay of 138 seconds from the MicroModule gas extraction unit in order to assign depth to the isotope measurements. The T-piece after the MicroModule was the point in the measurement system, where the flow was split for isotope and CH₄ measurements. Furthermore, the matlab script removed the background for each isotope (3.11.1), calculated ratios and delta values for each sample data point (3.11.2) which were then corrected for the pressure imbalance (3.11.3), the chemical slope (3.11.4) and the solubility effect (3.11.5).
4. The single measurement run files were finally combined into one file so that the isotopic data could be plotted on depth and once available on a preliminary gas age scale provided by Janani Venkatesh based on the measured methane matched with $\delta^{18}\text{O}$ (ice) data for Dye 3 (Venkatesh, 2020) as described in chapter 3.14.2.
5. Contamination of modern air was removed by matching up the elemental ratio spikes ($\delta\text{Ar}/\text{N}_2$) with spikes of the methane record. Once identified, they were removed manually from the onset of the suspected air spikes until the values gets back down to expectable δ -values similar to the onset values. Additionally, data at the beginning of the runs was removed since the IRMS measured included remains of the CH₄ standard in the system (that had no argon). A more detailed description of the contamination removal process is given in chapter 3.12.
6. A smoothing of 30 seconds (running average) was applied to the final delta values.

3.11 Applied corrections

The raw data needed to be corrected for background intensity (3.11.1), pressure imbalance (3.11.3), chemical slope (3.11.4) and the solubility effect (3.11.5) to get the final dataset which will be described in the following sub-chapters following Baldtzer Liisberg (2020). Additionally, the calculation of the isotopic ratios will be described in chapter 3.11.2.

3.11.1 Background correction

The raw intensities were corrected for the background intensity which was measured for the first 30 seconds of each run with both inlet valves closed. The following equation was used to correct for the background:

$$int_{bc} = int_{mea} - int_{bg} \quad (3.1)$$

Where int_{bc} = background corrected intensity; int_{mea} = measured intensity; int_{bg} = background intensity.

To have stable values, only data points from 15-28 seconds after measurement start were taken into account and averaged as the background intensities. The order of magnitude was on average < 1 mV for all measured masses and consequently the effect of background removal is minor.

3.11.2 Calculation of isotopic ratios

The isotopic ratios were calculated based on the background corrected intensities from each sample point and then using the following equations:

$$r_{29} = \frac{int_{bc}(29)}{int_{bc}(28)} \quad (3.2)$$

$$r_{36} = \frac{int_{bc}(36)}{int_{bc}(40)} \quad (3.3)$$

$$r_{\frac{Ar}{N_2}} = \frac{int_{bc}(40)}{int_{bc}(28)} \quad (3.4)$$

Where r_x = ratio of isotope x; $int_{bc}(y)$ = intensity with background correction in mV; $x = 29, 36, Ar/N_2$; $y = 28, 29, 36, 40$

3.11.3 Pressure imbalance correction

The *pressure imbalance* needs to be determined because the measured isotopic ratios are sensitive to changes of the signal intensity of the ion beam (Huber and Leuenberger, 2004). This correction also normalizes the flow of the standard and sample into the mass spectrometer which are slightly different (ibid.). Furthermore, the sample flow varies slightly in reality

because of small changes in the gas content of the ice core. This effect is assumed to be minor but is also taken into account with the pressure imbalance correction.

The pressure imbalance was determined by varying inlet pressures on the standard inlet (the nitrogen and argon mix). This was achieved by changing the gas flow using the installed forward pressure regulator (FPR) to simulate different flows coming into the mass spectrometer while the sample inlet with lab air was kept at a constant pressure of 200 mbar. The acquisition was run for 5 cycles and then averaged.

From these data, a linear calibration scheme (slopes p_{29} , p_{36} , p_{Ar/N_2} and corresponding intercepts) was calculated in order to correct the isotopic ratios for this effect:

$$\delta_{p_{29}} = \left(\left(\frac{r_{29}}{r_{29std}} \right) - 1 \right) - p_{29} * (int_{28bc} - 10500 \text{ mV}) \quad (3.5)$$

$$\delta_{p_{36}} = \left(\left(\frac{r_{36}}{r_{36std}} \right) - 1 \right) - p_{36} * (int_{40bc} - 8900 \text{ mV}) \quad (3.6)$$

$$\delta_{p_{\frac{Ar}{N_2}}} = \left(\left(\frac{\frac{r_{Ar}}{N_2}}{\frac{r_{Ar}}{N_{2std}}} \right) - 1 \right) - p_{Ar/N_2} * (int_{28bc} - 10500 \text{ mV}) \quad (3.7)$$

δ_{px} = pressure imbalance corrected delta value; $x = 29, 36$ or Ar/N_2 ; r_x = ratio of the sample; r_{xstd} = ratio of the standard from the daily calibration input file (Table 3.2); p_x = average slope of the pressure imbalance found; int_{xbc} = intensity background corrected.

Calculating the slope of the pressure imbalance, the following values were found (Appendix 5):

$$\left[p_{29} = 1.05 * 10^{-4} \frac{\text{‰}}{\text{mV}} \right] \quad \left[p_{36} = 6.76 * 10^{-4} \frac{\text{‰}}{\text{mV}} \right] \quad \left[p_{\frac{Ar}{N_2}} = 5.59 * 10^{-4} \frac{\text{‰}}{\text{mV}} \right]$$

The intensities we standardize our measurements to are subjectively chosen to be 10,500 mV for mass 28 (nitrogen) and 8,900 mV for mass 40 (argon).

The pressure imbalance is corrected by subtracting the pressure imbalance fractionation from the measured delta value.

3.11.4 Chemical slope correction

The intensities of gases measured by mass spectrometry are sensitive to slight changes in the gas composition (Sowers et al., 1989). The measured intensities of nitrogen and argon isotopes are therefore sensitive to changes in the elemental ratio of Ar/N₂. This effect has been termed *chemical slope*. It was experimentally determined, and the pressure imbalance corrected sample data was corrected for this effect.

The chemical slope was determined by varying the argon fraction in the nitrogen and argon mix and dual inlet measurements with 5 cycles against laboratory air were done. The argon pressure was varied from 1.0 bar to 2.2 bar while the usual setpoint was at 1.6 bar. The sample inlet (lab air) was kept at 200 mbar and the standard inlet (nitrogen and argon mix) was kept at 145 mbar on a constant basis.

The plotted the chemical slope measurements and gave the following correction equations:

$$\delta_{c29} = \delta_{p29} - (\delta_{p40} * a_{29}) \quad (3.8)$$

$$\delta_{c36} = \delta_{p36} - (\delta_{p(\frac{Ar}{N_2})} * a) - (\delta_{p(\frac{Ar}{N_2})} * b)^2 \quad (3.9)$$

Where δ_{cx} = chemical slope corrected delta value; δ_{px} = pressure imbalance corrected delta value; x = 29 or 36

The following chemical slope coefficients were found (Appendix 6):

$$\left[a_{29} = 4.97 * 10^{-5} \frac{\text{‰}}{\text{‰}} \right] \quad \left[a = -1.78 * 10^{-2} \frac{\text{‰}}{\text{‰}} \right] \quad \left[b = 9.59 * 10^{-6} \frac{\text{‰}}{\text{‰}^2} \right]$$

3.11.5 Solubility effect correction

The *solubility effect correction* accounts for a fraction of the gas sample that got dissolved in the meltwater and the fractionation of the isotopes before reaching the MicroModule and during the extraction process. That means consequently that the gas extraction efficiency of the MicroModule was lower than 100%. A correction for this effect was done based on Henry's law by Jesper Baldtzer Liisberg (Baldtzer Liisberg, 2020). Another issue that needs to be considered is that N₂ is only half as soluble in water as oxygen and argon which results in the depletion of Ar in the elemental ratio (Baldtzer Liisberg, 2020).

Two different tests were done to assess this effect. The first one was done by Janani Venkatesh with pure nitrogen where liquid pump speed, pressure setpoints at the MicroModule extraction unit were varied from 250 to 500 mbar and input gas ratios were changed between 1.25 ml and 3.75 ml in 0.25 ml steps to determine the extraction efficiency of the MicroModule (Venkatesh, 2020). The extraction efficiency was calculated by dividing the measured by the introduced gas flow. The maximum achievable extraction efficiency of the MicroModule would be 98.2% and would be achieved with a shellside pressure of 0 mbar based on the intercepts with the y-axis. The extraction efficiency at the used 300 mbar setpoint is between 92.5% and 96.3%. The extraction efficiency depends on the pressure setpoint (e.g. the flow) and the fraction of gas in the sample prior to extraction (gaspercent).

A second test was performed by Jesper Baldtzer Liisberg to determine the fractionation throughout the whole system for the different isotopes. He introduced the nitrogen/argon standard mix throughout the whole system (including Nafion, cryotrap and perovskite membrane), the pressure was held constant at 200 mbar and the input gas ratio, and the pump speeds were varied. The isotopic intensities were measured to assess and correct for this effect. A logarithmic correlation was found and consequently, the logarithm of the gas ratio is taken to get a linear relationship. With the results of these two tests, it is possible to correct for the dissolution and fractionation of the gases based on the following equations:

$$\delta_{s29} = \delta_{c29} - sc_{29} * \ln (g\%) \quad (3.10)$$

$$\delta_{s36} = \delta_{c36} - sc_{36} * \ln (g\%) \quad (3.11)$$

$$\delta_{s\frac{Ar}{N_2}} = \delta_{c\frac{Ar}{N_2}} - sc_{\frac{Ar}{N_2}} * \ln (g\%) \quad (3.12)$$

Where δ_{sx} = solubility effect corrected delta values; δ_{cx} = chemical slope corrected delta value; sc_x = slope constants for the solubility correction, \ln = logarithm; $g\%$ = general gas ratio in the sample stream; x = 29 or 36 or Ar/N₂.

$$[sc_{29} = 5.8 * 10^{-3}\%] \quad [sc_{36} = -0.30 \%] \quad \left[sc_{\frac{Ar}{N_2}} = 27.3 \% \right]$$

It is important to note that the coefficient sc_{29} is substantially smaller (and has also a worse R² value of only 0.18) than the two other coefficients which results in a smaller correction for $\delta^{15}N$

values. A potential explanation for this observed effect is that the MQ-water in which the nitrogen and argon mix is introduced was degassed with pure nitrogen. Consequently, the MQ water was already enriched beforehand with pure nitrogen resulting in a lower dissolution of $\delta^{15}\text{N}$. The expected correction coefficient is assumed to be higher than the one found by the tests, resulting in an overall higher CFA $\delta^{15}\text{N}$ value.

After the background, pressure imbalance, chemical slope and solubility effect correction, the δ -values are final. In the following, the data were cleaned for lab air contamination and afterwards smoothed.

Please note that the final data is converted from $\delta^{36}\text{Ar}$ to $\delta^{40}\text{Ar}$ since it is more frequently used in the science community. The following conversion equation was used:

$$\delta^{40}\text{Ar} = \left(\frac{1}{\delta^{36}\text{Ar} + 1} - 1 \right) \quad (3.13)$$

3.12 Removal of lab air contamination and smoothing

Lab air contamination entered occasionally the CFA system at the melthead while melting the ice core due to misaligned breaks in the ice or at the starts of new CFA sticks. This contamination was removed from the data based on simultaneous spikes in the elemental ratio ($\delta\text{Ar}/\text{N}_2$) and CH_4 data. Due to the previously discussed solubility effect, the elemental ratio of the sample is depleted in terms of argon compared to the lab air, which results in a spike in the $\delta\text{Ar}/\text{N}_2$. Intrusion of lab air gives clear marks in the elemental ratio because it differs from the fractionation in the firn (thermal fractionation and gravitational settling) in contrast to the elemental ratio in lab air is consistently higher and considered stable over a millennial time scale. When the two spikes of elemental ratio and CH_4 data aligned at the same depth, it was additionally a good confirmation that our depth assignment was accurate.

Finally, a smoothing of a 30 seconds running average was applied to make variations in the data more visible without losing too much precision. Especially the $\delta^{40}\text{Ar}$ data had a lot of noise which makes variations better visible after the applied smoothing.

3.13 Error calculation

The uncertainties of the intensities are the basis for the error estimation of the delta values and are taken into consideration while processing the data. A Gaussian error propagation was used to calculate the errors with a 1σ distribution (Baldtzer Liisberg, 2020).

The used equations can be found in Appendix 7-9.

3.14 Depth and age assignment

3.14.1 Depth scale

The encoder data and ice core logs (for starting and end depth of each bag, breaks and missing pieces) were used by Janani Venkatesh to calculate the melt speed and assign a depth to each datapoint at the melt head (Venkatesh, 2020). Taking into account the flow and pressure variations of the sample stream, the delay time was calculated to get a depth assignment for the CH₄ measurements at the Picarro. In a third step, the travel time of the sample to the MicroModule was calculated as it is the shared path from the melthead for both, isotope and CH₄ measurements. Methane and isotope measurements used the same measurement time scale to facilitate this depth assignment. The flow towards the IRMS is considered constant because the pressure gradient between the MicroModule and the perovskite oven setup was kept constant. The depth assignment for the isotopes was done by adding a constant delay of 138 seconds to the MicroModule time and the delay from the assigned depth at the melthead. The depth assignment can be described with the following equation:

$$D_{isotopes}(t) = D_{MH}(t) + d_{MH-MM} + d_{MM-MS} \quad (3.14)$$

Where $D_{isotopes}$ = depth for the isotopes measurements at time t ; D_{MH} = depth at the melt head calculated based on ice core logs and encoder data at measurement time t ; d_{MH-MM} = varying delay between the melt head and MicroModule; d_{MM-MS} = constant delay between MicroModule and IRMS: 138 seconds

3.14.2 Gas age scale

The existing $\delta^{18}O$ ice age scale from Dye 3 (provided through personal communication with Bo Vinther) was used to match up spikes of $\delta^{18}O$ with the spikes seen in the CH₄ data to get a gas age time scale (Baldtzer Liisberg, 2020). By doing this, it is possible to get a Δ depth between

ice spikes seen in the $\delta^{18}\text{O}$ and CH_4 which can be converted into a delta age and the age scale is then shifted to match the $\delta^{18}\text{O}$ peaks. This assignment is preliminary and certainly not perfect since it shows a leading gas age in some sections which is impossible. As specified in chapter 1.9, the ice is always older than the air bubbles trapped in it due to the fact that gases still can diffuse freely in the firn column until they are closed off completely from the atmosphere. For this preliminary gas age scale, the gas age leads in some sections over the ice age. It is planned to match the methane data with a methane gas scale with another ice core to get a more accurate gas age assignment.

The depth-gas age assignment is shown below.

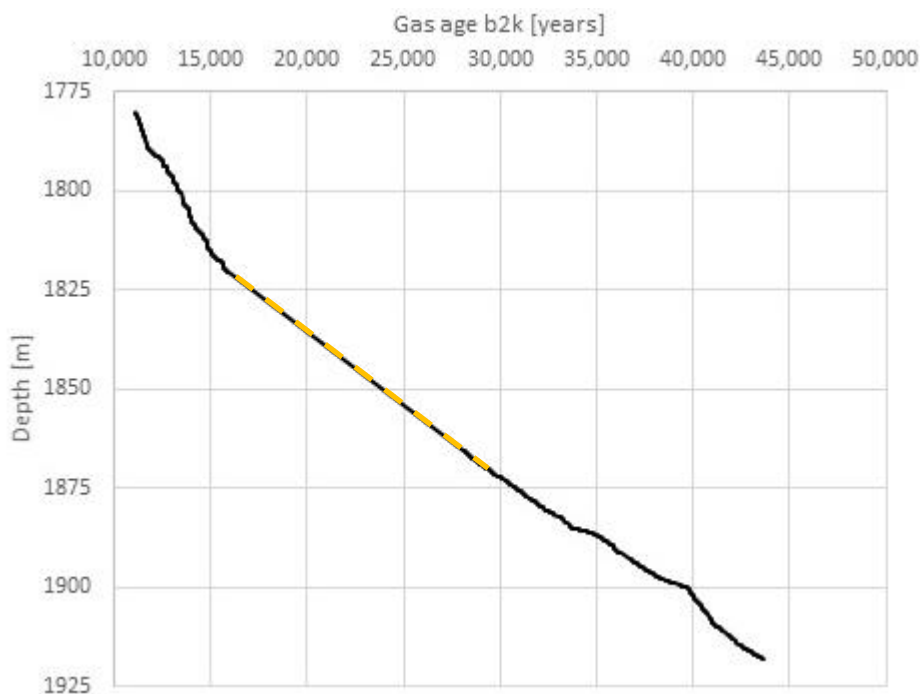


Figure 3.10: The gas age before the year 2000 (b2k) and depth assignment based on the methane measurements. The dashed yellow line indicates a linear extrapolation between the two depth sections of Dye 3 that were measured.

4 Results and Discussion

In this chapter, an overview about the results of $\delta^{15}\text{N}$, $\delta^{40}\text{Ar}$, $\delta^{18}\text{O}$ (ice) and the elemental ratio $\delta\text{Ar}/\text{N}_2$ and CH_4 is given. Furthermore, the daily calibration runs will be evaluated as a source of potential instability. The removal of CO_2 and O_2 will be analysed to confirm that they were constant during the measurement campaign. Additionally, the measured CFA $\delta^{15}\text{N}$ data are compared with discrete measurements of $\delta^{15}\text{N}$ from Dye 3 taken by Todd Sowers (Pennsylvania State University, US). Moreover, the CFA $\delta^{15}\text{N}$ data is compared to NGRIP $\delta^{15}\text{N}$ data to confirm the data quality and seen D-O events. Finally, the temperature reconstruction for the Dye 3 CFA $\delta^{15}\text{N}$ values is presented, analysed and compared to the NGRIP temperature reconstruction done by Kindler et al., (2014).

4.1 Combined results overview

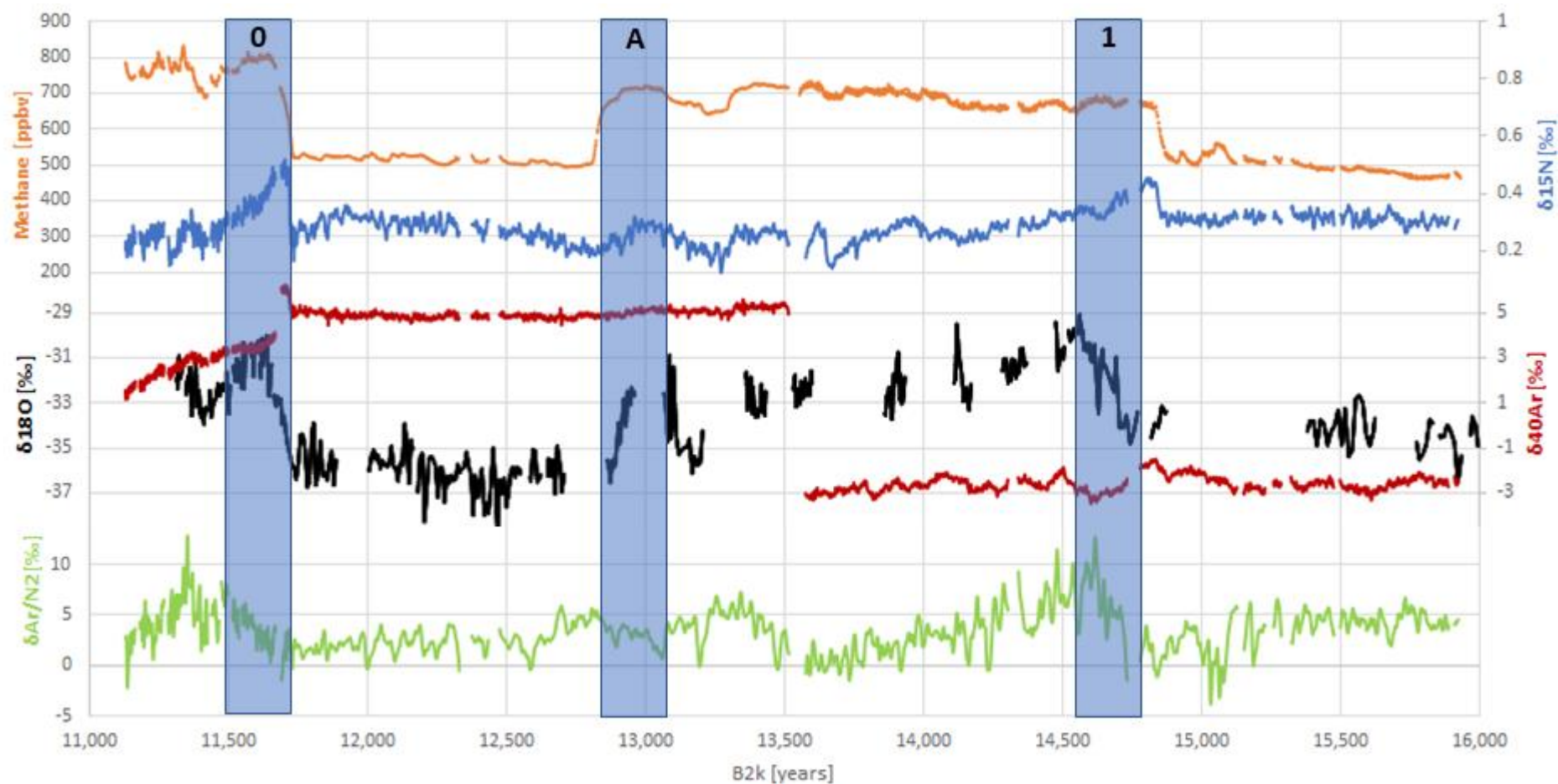


Figure 4.1: Combined results from 11,000 to 16,000 years b2k showing CH_4 , $\delta^{15}N$, $\delta^{40}Ar$, $\delta Ar/N_2$ on the preliminary gas age scale. $\delta^{18}O$ (ice) is shown for comparison on the assigned ice age scale (GIC05) and was provided by Bo M. Vinther (PICE). This first section corresponds to depths from 1780 m to 1821 m.

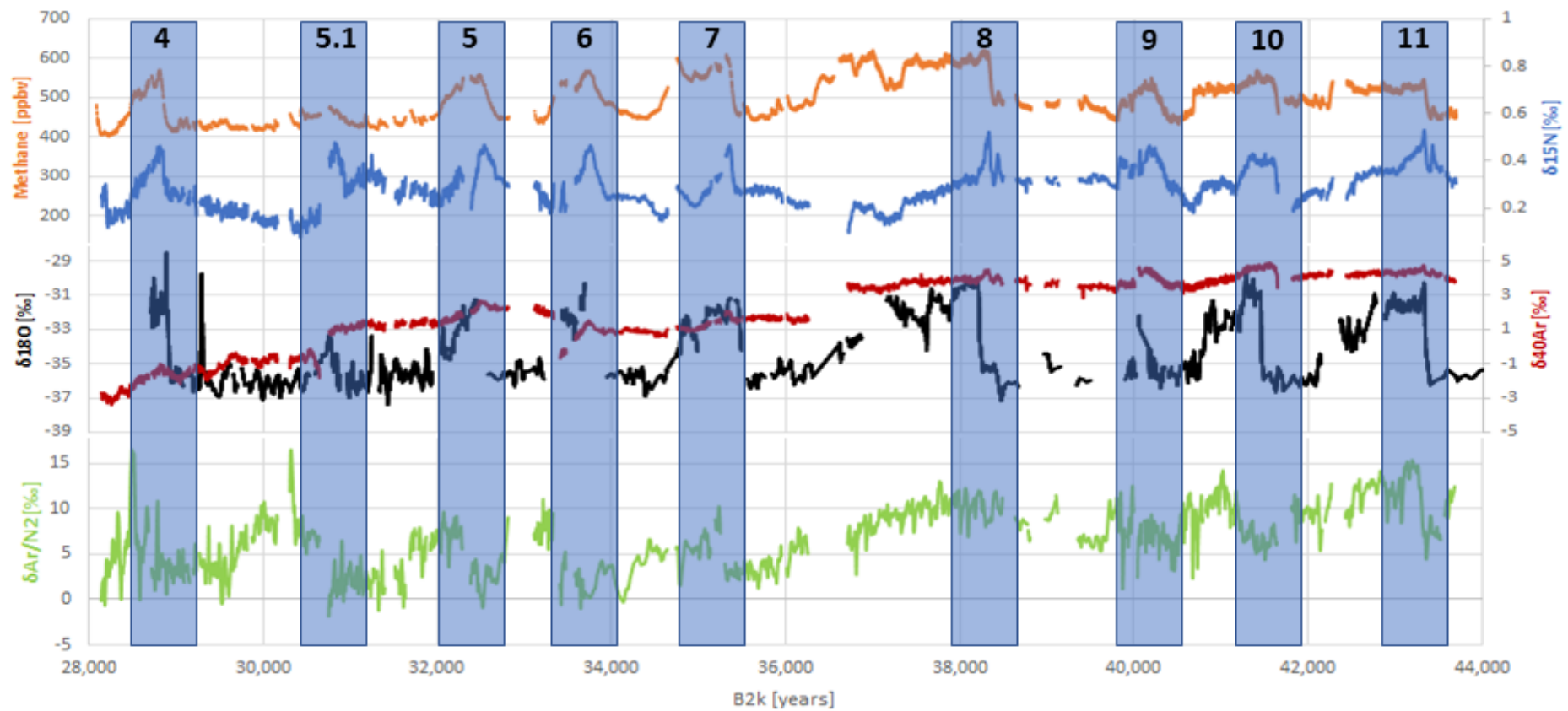


Figure 4.2: Combined results from 28,000 to 44,000 years b2k showing CH_4 , $\delta^{15}\text{N}$, $\delta^{40}\text{Ar}$, $\delta\text{Ar}/\text{N}_2$ on the preliminary gas age scale. $\delta^{18}\text{O}$ is shown for comparison on the assigned ice age scale (GIC05) and was provided by Bo M. Vinther (PICE). This second section shown corresponds to depths from 1865 m to 1920 m.

In this combined dataset seen in Figure 4.1 and Figure 4.2, the important climatic events are marked: The Younger Dryas transition to the Holocene period (0), the Bølling-Allerød (A) event, D-O event 1, and D-O events 4-11 were identified, numbered and marked in light blue. They align generally well between the CH₄, δ¹⁵N, δ⁴⁰Ar, meaning that the gas age assignment generally agrees well. A slight delay is seen between the δ¹⁸O (ice) and the beforementioned gas parameters which is also to be expected.

For the Bølling-Allerød, D-O event 8 and D-O event 10, the gas measurements seem to lead the δ¹⁸O (ice) signal which is impossible and therefore the preliminary gas age assignment needs to be improved.

The δ¹⁵N record is the most precise of the isotope measurements of this campaign and it was possible to correct for the impact of potentially unstable lab air. All climatic transitions observed in other cores during that time period can be seen in the measured data from Dye 3.

The δ⁴⁰Ar record is heavily impacted by the variations in the lab air - as it is more sensitive - and it was not possible to correct for this effect because of too large variations seen and some unexplainable effects in the data. When comparing CFA δ⁴⁰Ar and CFA δ¹⁵N signals of the D-O events, the δ⁴⁰Ar signal is generally less pronounced than the δ¹⁵N. A potential explanation for this low δ⁴⁰Ar is argon gas loss due to long storage time in the freezer since argon is supposed to leak from the ice matrix due to its smaller molecule size (Kobashi et al., 2008).

The observed variations in δ¹⁵N and δ⁴⁰Ar highlight changes in the firn column conditions. The changes seen in δ⁴⁰Ar and δ¹⁵N are due to the previously introduced firn processes e.g. gravitational settling which relates to changes in the firn depth and thermal fractionation due to changes in temperatures.

CH₄ and δ¹⁸O (ice) are plotted for comparison and to confirm the climatic events which agree generally well. δ¹⁸O (ice) leads for most climatic events, as it would be expected.

4.2 Calibration runs

As it can be seen in the combined results, there are massive and likely unrealistic shifts in the isotopic data, especially for δ⁴⁰Ar which could not be corrected for. One possible reason for these unrealistic shifts is an unstable composition of lab air (which was assumed to be constant) during calibration runs between measurement days. This chapter investigates this theory further. The daily calibrations are plotted to identify potential drifts in Figure 4.3.

Calibration data will be presented in two datasets because the weekend was in between the two measurement weeks, and therefore no sample data was generated for that period. A zoom on the second week of measurements from the 4th November 2019 evening run until 7th November 2019 with relatively stable δ -values was done to show the variation during those relatively stable conditions.

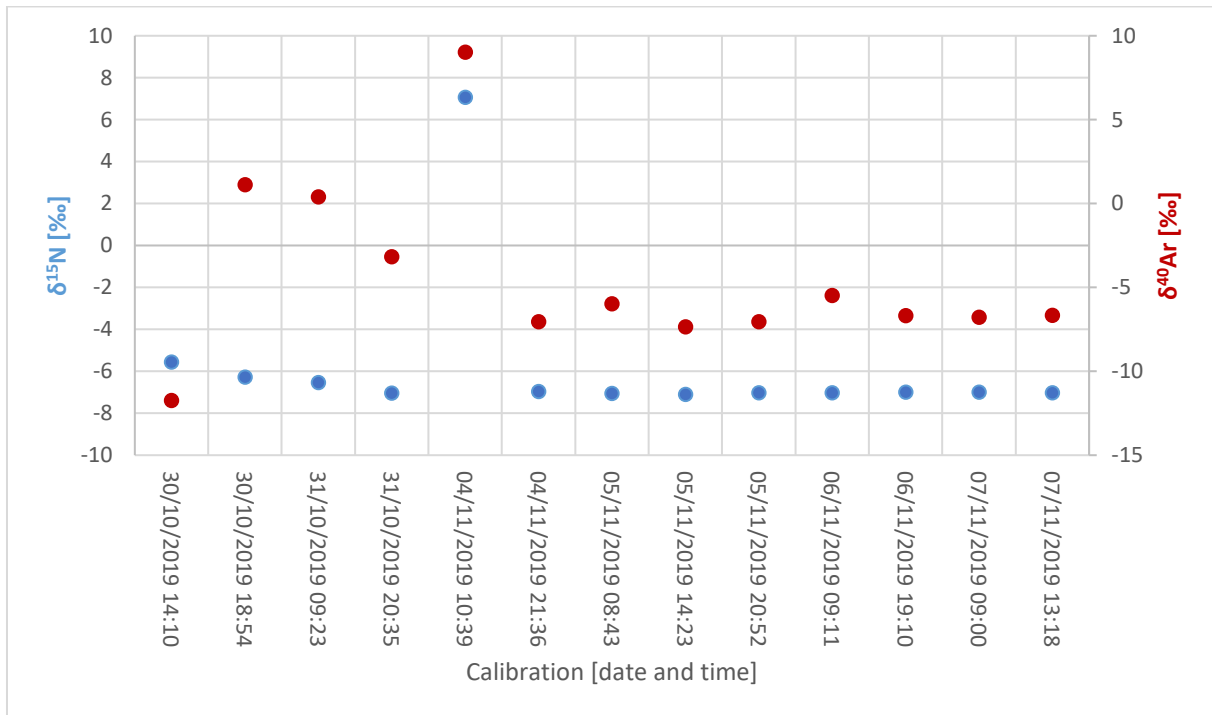


Figure 4.3: Overview of variations observed on $\delta^{15}\text{N}$ and $\delta^{40}\text{Ar}$ during the daily calibrations of standard (nitrogen-argon mix) against lab air.

Figure 4.3 gives an overview about the observed variations during the calibrations. The 30th and 31st October are generally unstable and the period from the 4th to the 7th shows less variation for both δ -values. The measurement system was not fully ready to be used on the 30th October 2019 and is just shown for comparison. Unfortunately, there is no explanation for the observed trend on the 31st October 2019. The results of the morning calibration run of the 4th November 2019 are sticking out and will be explained further on. Generally, the calibration values get more stable towards the end of the measurement campaign during the second week of measurements.

4.2.1 Calibration results for nitrogen

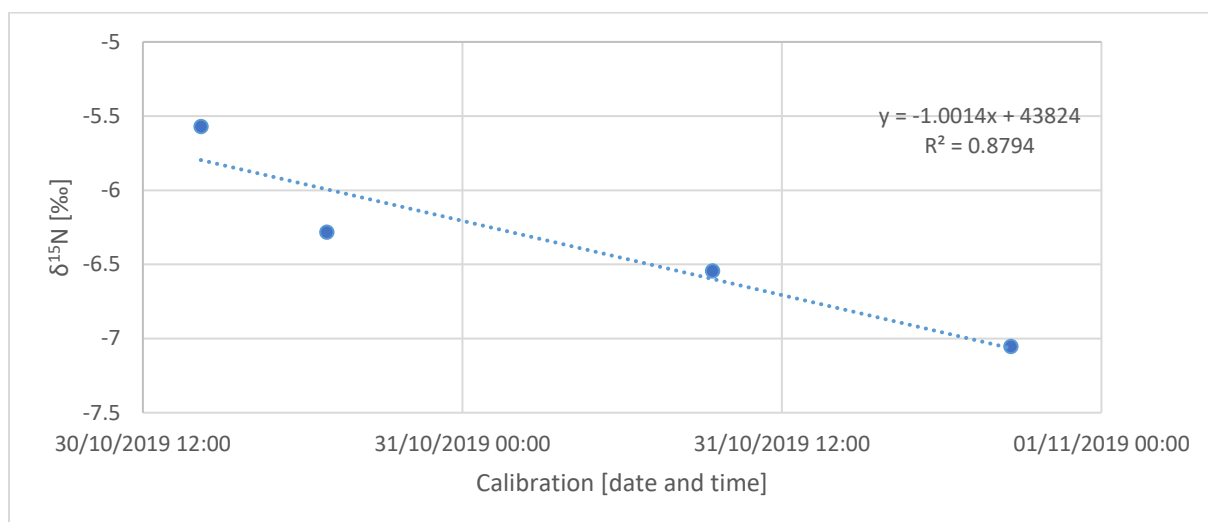


Figure 4.4: Daily $\delta^{15}\text{N}$ calibrations of the 30th and 31st October 2019.

On the 30th and 31st October the $\delta^{15}\text{N}$ values dropped over time from -5.5 to -7‰ as seen in Figure 4.4. There is no explanation for this decreasing trend. The 30th October 2019 has been excluded from further processing because there was an analytical problem with the analyser heater turned on accidentally. The mean for these two days is 6.36 ‰ with a high standard deviation of ± 1.24 ‰ (2σ).

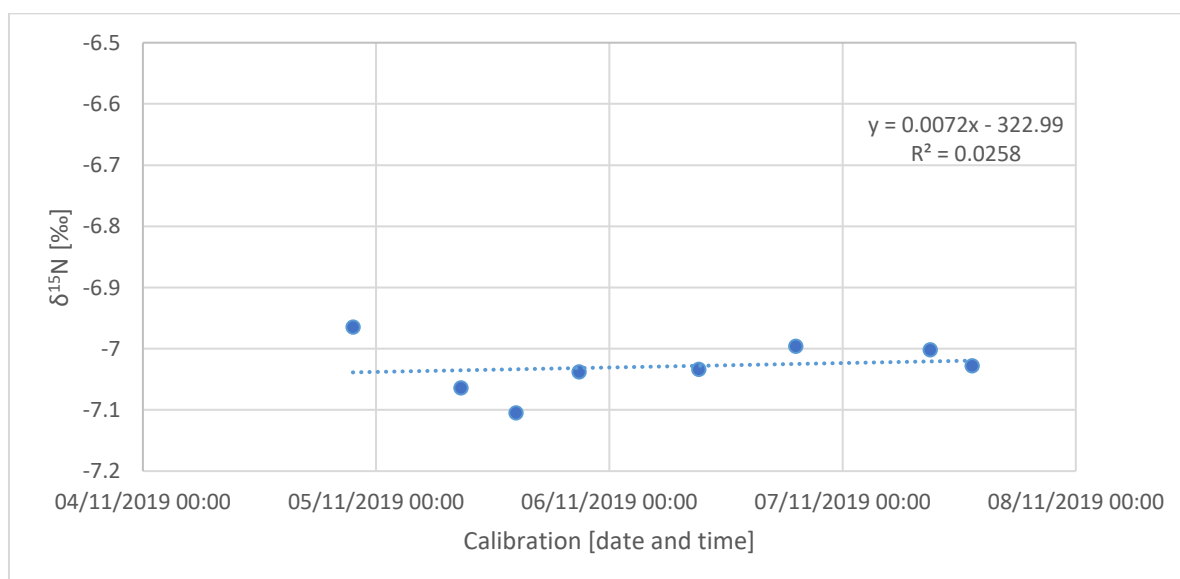


Figure 4.5: Daily $\delta^{15}\text{N}$ calibrations of the second measurement week (4th to 7th November 2019) excluding the morning calibration of the 4th November when the Argon was turned off accidentally.

For the morning calibration of the 4th November 2019, the argon pressure was turned off accidentally which resulted in $\delta^{15}\text{N}$ of +7.059 ‰. A zoom on the calibration runs on the from the 4th (evening calibration) to the 7th of November 2019 in Figure 4.5 shows that the $\delta^{15}\text{N}$ values

are more stable with a mean of $-7.029 \text{ ‰} \pm 0.086 \text{ ‰}$ (2σ) which is a rather high standard deviation for a supposedly stable standard. Over the course of the second week of measurements there was a low increase (0.0072) of the values of $\delta^{15}\text{N}$ but with a low R^2 value of 0.0258.

4.2.2 Calibration results for argon

Figure 4.6 shows the $\delta^{40}\text{Ar}$ calibration runs for the 30th and 31st October 2019.

Please note that the y-axis is adjusted to show the variation in the daily calibrations and is not plotted on the same scales for the y-axis.

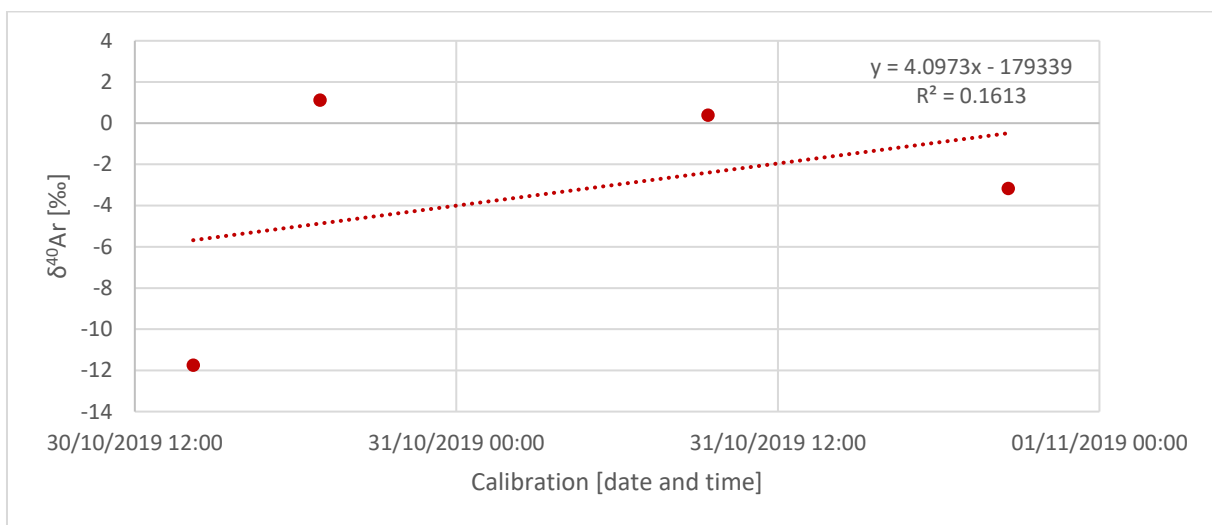


Figure 4.6: $\delta^{40}\text{Ar}$ calibration values of the 30th and 31st October 2019.

A large variation can be seen for $\delta^{40}\text{Ar}$ between the first two measurement days in the calibrations against lab air. As already mentioned, the 30th October as was excluded from further data evaluation due to analytical problems and is just shown for comparison. The variation of more than 3 ‰ on the 31st October is also high between the two calibration runs. The mean of these two days is $3.324 \text{ ‰} \pm 11.80\text{‰}$ (2σ) which is very high.

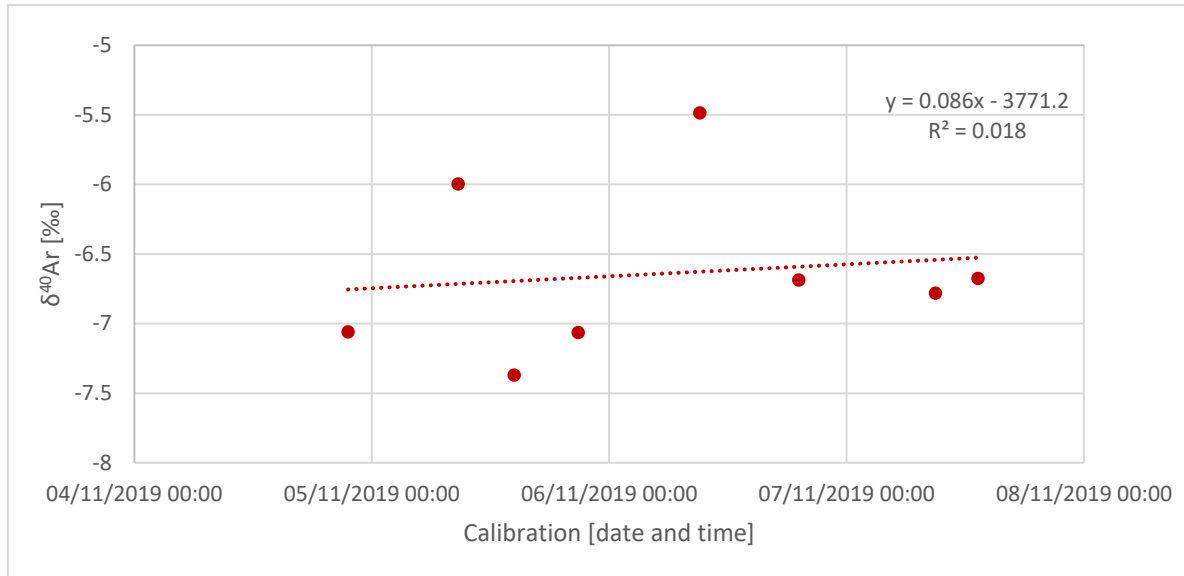


Figure 4.7: $\delta^{40}\text{Ar}$ calibration values of the second measurement week excluding the morning calibration of the 4th November when the argon was turned off.

The mean of $\delta^{40}\text{Ar}$ during the second week of measurements excluding the morning calibration of the 4th November is $-6.58 \text{ ‰} \pm 1.27 (2\sigma)$ which implies that the variation to be seen between the calibrations is large.

The overall mean is $6.98 \text{ ‰} \pm 0.32 (2\sigma)$ for $\delta^{15}\text{N}$ and $-5.59 \text{ ‰} \pm 4.85 (2\sigma)$ for $\delta^{40}\text{Ar}$ taking into account the 31st October and the evening calibration of the 4th and the calibrations of the 5th, 6th and 7th November 2019. For both $\delta^{15}\text{N}$ and $\delta^{40}\text{Ar}$ a lot of variation during the daily calibrations can be seen which are sometimes due to analytical problems as for the 30th October and the 4th November and sometimes the cause remains unknown. For the main fraction of the variability seen in the $\delta^{15}\text{N}$ and $\delta^{40}\text{Ar}$ calibrations, we suspect an unstable noble gas ratio of our laboratory air. Potential explanations for these observed variations are that there was not enough ventilation in the lab, temperature variations in the laboratory might have played a role, and over the course of 5 weeks the lab air was enriched in nitrogen (from flushing the Nafion membranes) as well as evaporated liquid nitrogen from the cryogenic trap. For the $\delta^{15}\text{N}$, it was possible to correct the sample data decently for the shifts seen, but the lab air does not seem stable enough for precise $\delta^{40}\text{Ar}$ measurements with this type of setup and the lab air variations experienced.

4.3 Removal of CO₂

CO₂ was removed from the sample stream with a liquid nitrogen trap. To confirm a steady removal over the measurement campaign, the CO₂ intensity (mass 44) is plotted against $\delta^{15}\text{N}$ and $\delta^{40}\text{Ar}$ to visualize the potential effect on the delta values. A smoothing of 30 seconds was applied for the CO₂ intensity, the $\delta^{15}\text{N}$ and $\delta^{40}\text{Ar}$. Unfortunately, no baseline level of CO₂ was measured (laboratory air measurements without the liquid nitrogen trap) and consequently it is not possible to quantify the exact CO₂ removal (in %) and whether the removal of CO₂ leads to an overall better data quality.

Figure 4.8 and Figure 4.9 give an overview about the CO₂ intensities as well as the measured $\delta^{15}\text{N}$ and $\delta^{40}\text{Ar}$ to assess the potential impact of CO₂ removal on the data visually.

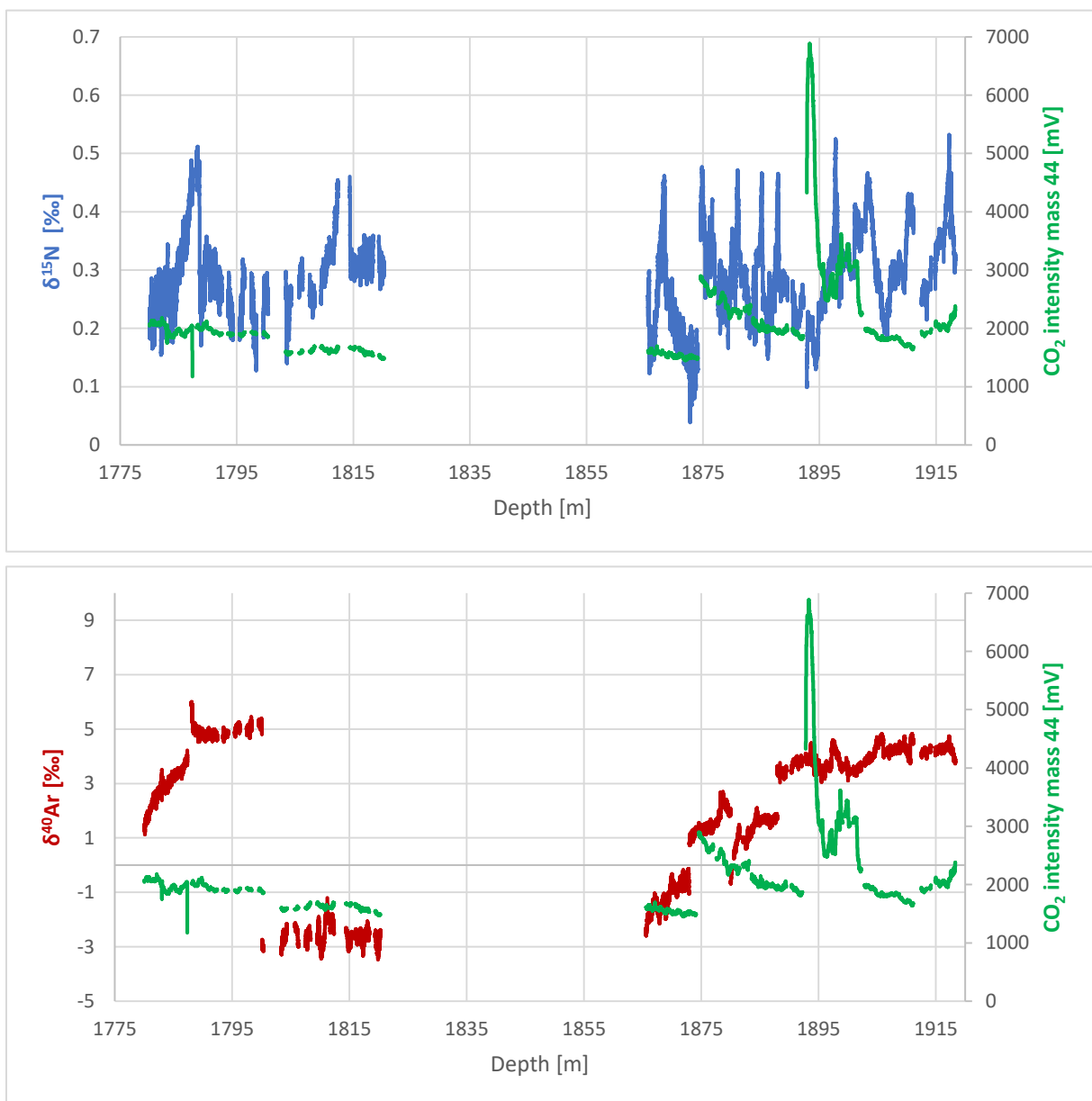


Figure 4.8 and Figure 4.9: The impact of CO₂ removal on the $\delta^{15}\text{N}$ and $\delta^{40}\text{Ar}$ data on a depth scale.

The measured CO₂ intensities were mostly below 2500 mV and are relatively constant, although small daily variations can be observed. The variations seen depend probably on the amount of liquid nitrogen that was added to the trap and consequently on the temperature of the trap. The CO₂ spike at 1893 m of about 6,900 mV is very surprising and has no explanation according to our knowledge. The most likely explanation is that not enough liquid nitrogen was added to the trap. Fortunately, this spike did not seem to have influenced the sample in terms of δ -values. It is also unusual that the decrease of CO₂ takes almost 2 meters, equal to approximately 50 minutes of sampling time. The normal observed effect after having added liquid nitrogen is that the CO₂ signal drops immediately. Another potential explanation would be a leak that closed itself gradually. But in the $\delta\text{Ar}/\text{N}_2$ there is no indication of an intrusion of lab air, so this hypothesis can be discarded.

To get a closer look on the CO₂ spike, it was zoomed in for the two relevant δ -values in Figure 4.10 and Figure 4.11.

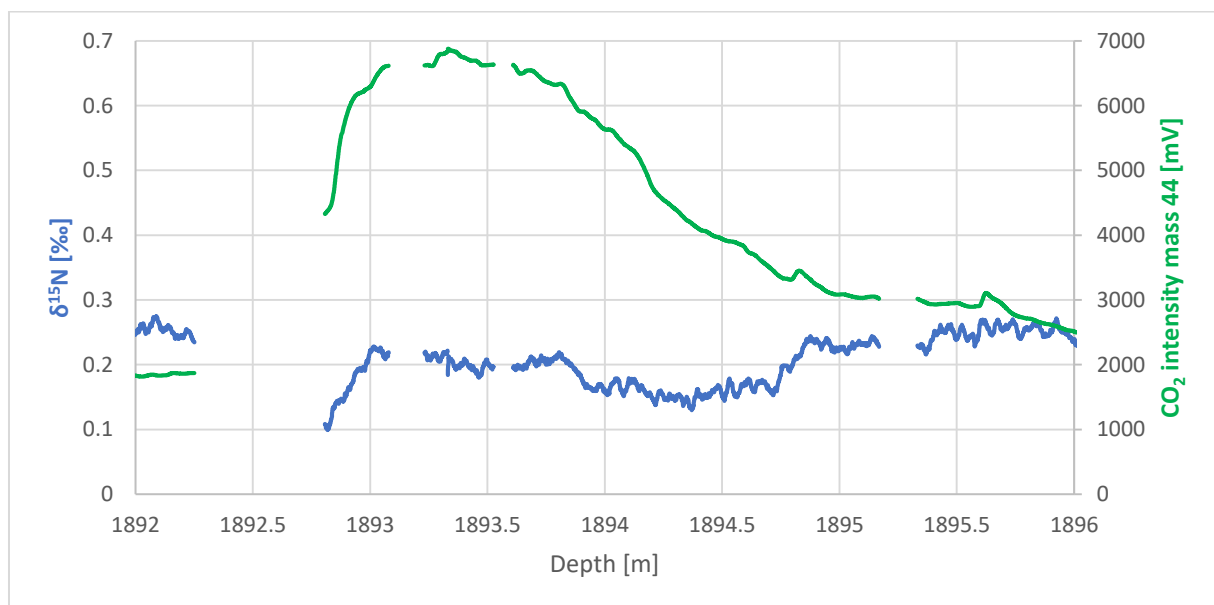


Figure 4.10: Graph showing the impact of the CO₂ spike on the $\delta^{15}\text{N}$ data on a depth scale.

The level of CO₂ seems to correlate with some changes seen in $\delta^{15}\text{N}$, whereas in the $\delta^{40}\text{Ar}$ there is no effect seen on the data.

The CO₂ spike seems to have a small influence on the $\delta^{15}\text{N}$ and results in lower values, but the change in delta values could be also due to a change in the sample independently from the CO₂.

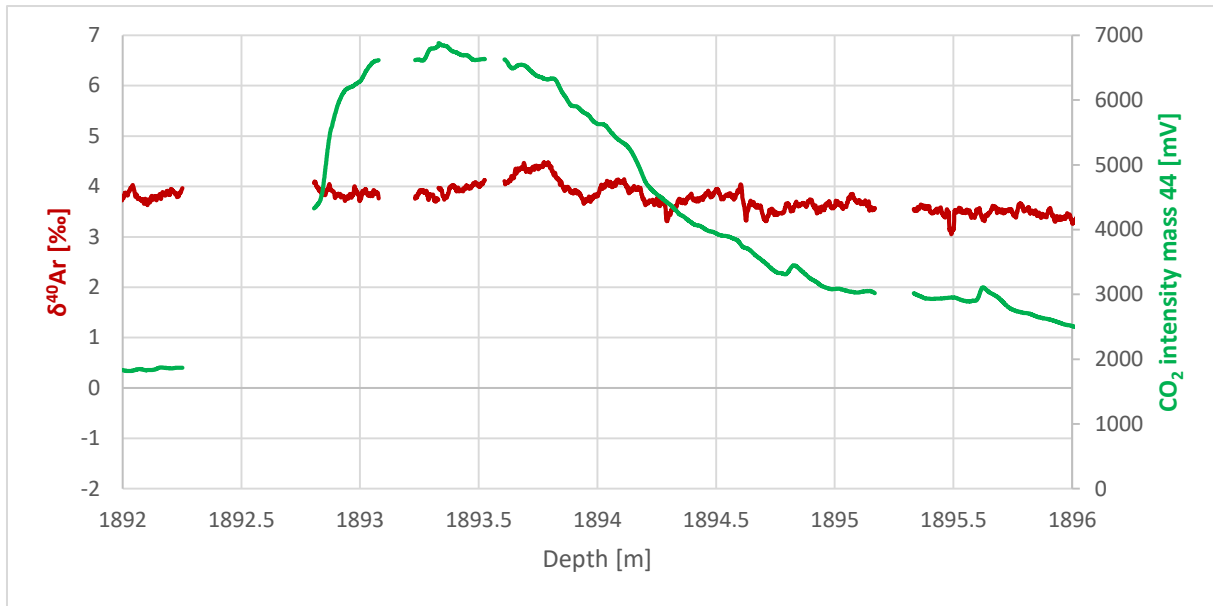


Figure 4.11: Graph showing the impact of the CO₂ spike on the $\delta^{40}\text{Ar}$ data on a depth scale.

Fortunately, the CO₂ spike did not seem to have affected $\delta^{40}\text{Ar}$. It remains unknown to what caused this sudden increase of CO₂ especially because it lasts over several meters (approx. 50 minutes of melting time). No explanation was found in the lab book that could explain this. Further tests would be necessary to analyse this strange effect on the delta values and also to assess whether a CO₂ removal from the sample leads to a better data quality.

4.4 Removal of oxygen

Oxygen was removed from the sample stream before entering the IRMS by the perovskite membrane to avoid interference with clumped oxygen $^{18}\text{O}_2$ on ^{36}Ar data and therefore get an overall better data quality. It is therefore necessary to assess the potential impact of oxygen on the isotope data of $\delta^{15}\text{N}$ and $\delta^{40}\text{Ar}$ and confirm a steady oxygen removal.

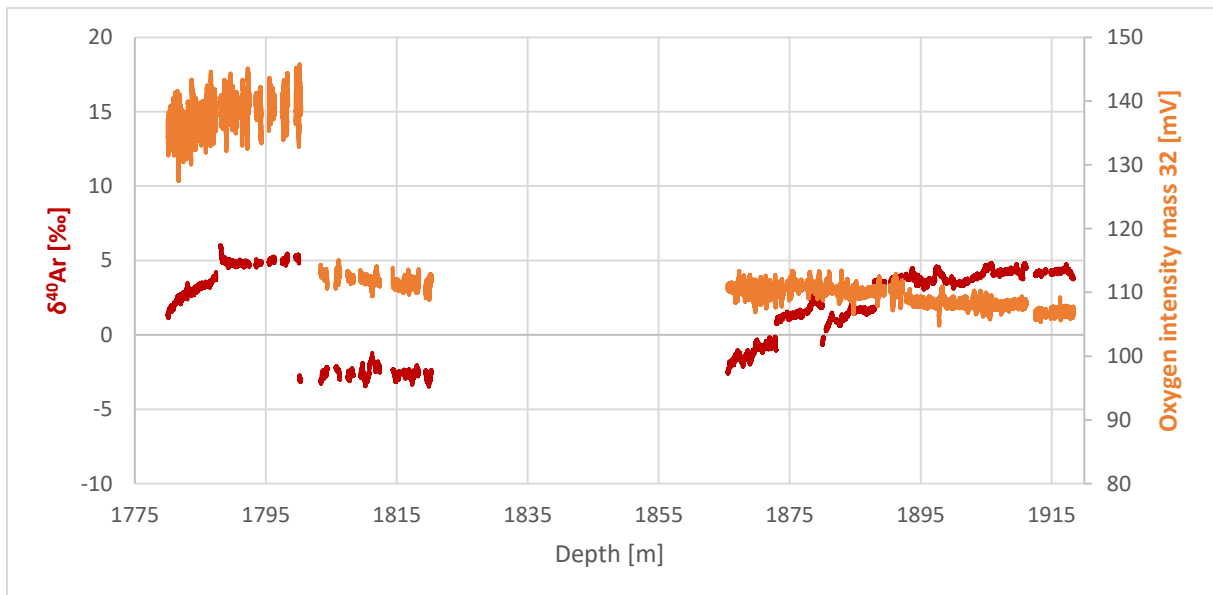
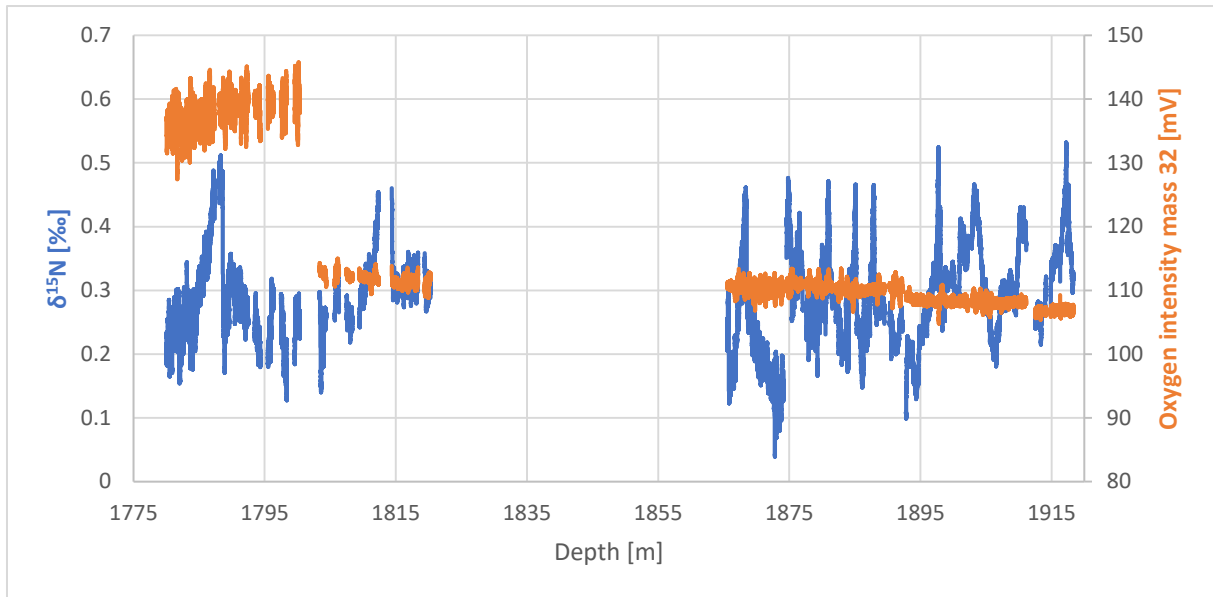


Figure 4.12 and Figure 4.13: Graphs showing the impact of the oxygen removal on $\delta^{15}\text{N}$ and $\delta^{40}\text{Ar}$ data.

There is no indication in the $\delta^{15}\text{N}$ and $\delta^{40}\text{Ar}$ data that the oxygen removal level had an influence on $\delta^{15}\text{N}$ and $\delta^{40}\text{Ar}$ based on figure 4.12 and figure 4.13. The oxygen removal is generally very high with more than 99% on average (based on $1.04 \times \text{intensity of mass 28}$ which was determined beforehand with tests on lab air without oxygen removal), so also the barometric interference of $^{18}\text{O}_2$ on ^{36}Ar is minimal. Based on a natural abundance of ^{18}O of 0.02% (Krebs, 2006) and an observed oxygen removal of >99%, the degree of interference with ^{36}Ar is 0.002%. There is no explanation to our knowledge for the observed higher removal from 1807 m and the further slight downward trend towards the end of the measurements at 1920 m.

4.5 Comparison of CFA $\delta^{15}\text{N}$ data with discrete Dye 3 $\delta^{15}\text{N}$

Todd Sowers from Pennsylvania State University (US) measured 100 discrete $\delta^{15}\text{N}$ samples from Dye 3 with a wet extraction technique. He provided his data for comparison with the Dye 3 $\delta^{15}\text{N}$ CFA measurements from this study. Discrete data is until now only available for measurements in 4 different depth zones. Due to the covid-19 pandemic, the remaining discrete samples have not been measured yet and were consequently not available for comparison.

Figure 4.14 below gives an overview about the available discrete and CFA measurements of $\delta^{15}\text{N}$ on a depth scale.

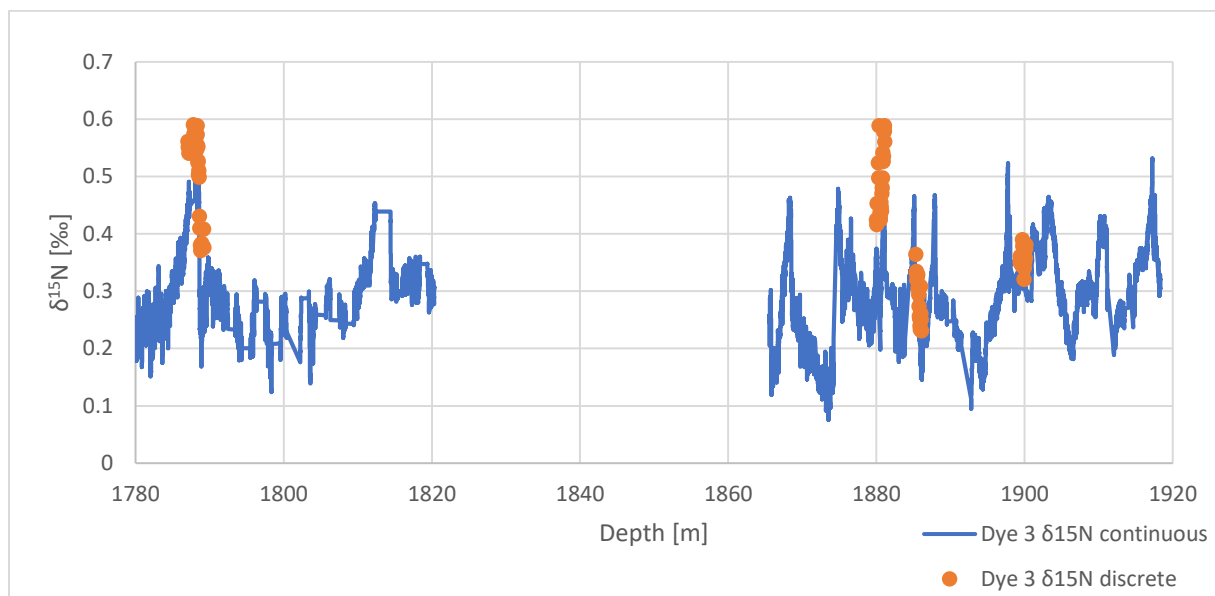


Figure 4.14: Overview of the discrete $\delta^{15}\text{N}$ and CFA $\delta^{15}\text{N}$ measurements from Dye 3 on a depth scale.

Zoom on the first depth zone

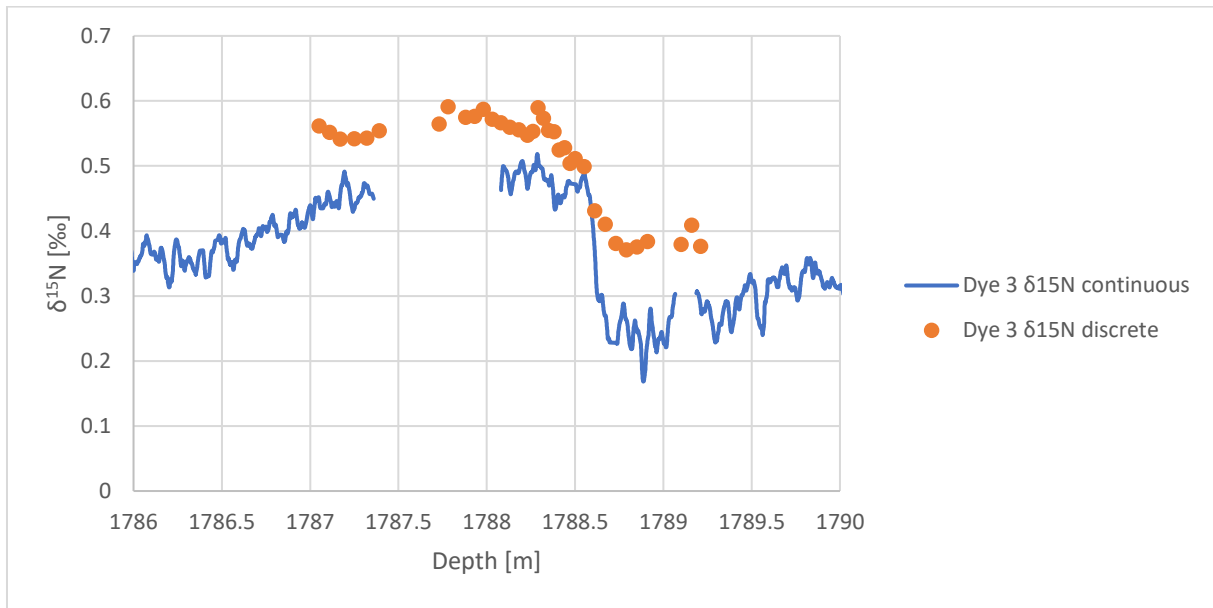


Figure 4.15: Comparison of $\delta^{15}\text{N}$ of discrete and CFA measurements in depth zone 1 ranging from 1786 m to 1790 m.

In the first depth zone, it is well visible that the discrete measurements have generally higher $\delta^{15}\text{N}$ values which is probably due to the solubility of the nitrogen in the liquid (as explained previously in the *solubility correction* chapter). The depth assignment seems to agree very well and in line with the observed trends. The deviation between the continuous and discrete measurements lies between 0.009 ‰ and 0.153 ‰. The offset is not constant between the discrete and continuous samples. The mean offset between discrete and CFA $\delta^{15}\text{N}$ for this depth zone is $0.09 \text{ ‰} \pm 0.07 \text{ ‰}$ (2σ).

Zoom on the second depth zone

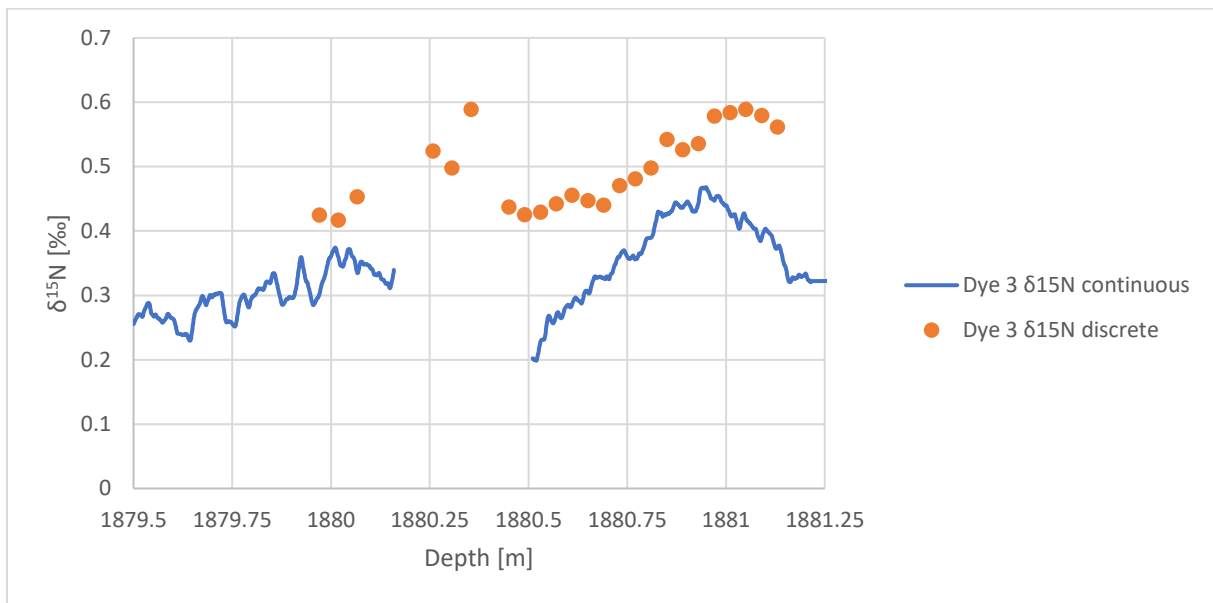


Figure 4.16: Comparison of $\delta^{15}\text{N}$ of discrete and CFA measurements in depth zone 2 ranging from 1879.5 m to 1881.25 m.

In this second depth zone, the deviation between the two datasets lies between 0.062 ‰ and more than 0.2‰ while the discrete measurements are constantly higher than the continuous measurements. Some more discrete measurements were available where the ice was too small in cross section for CFA measurements. Trend-wise there is some agreement but for the CFA data, the increase from 1880.5 m seems to be much steeper than the discrete measurements. The same observation is true for the downturn after the peak at 1880.94 m, the CFA decreasing trend is much steeper than the discrete data which just shows a slight downwards trend. The mean offset between discrete and CFA $\delta^{15}\text{N}$ for this depth zone is $0.14 \text{ ‰} \pm 0.08 \text{ ‰}$ (2σ).

Zoom on the third depth zone

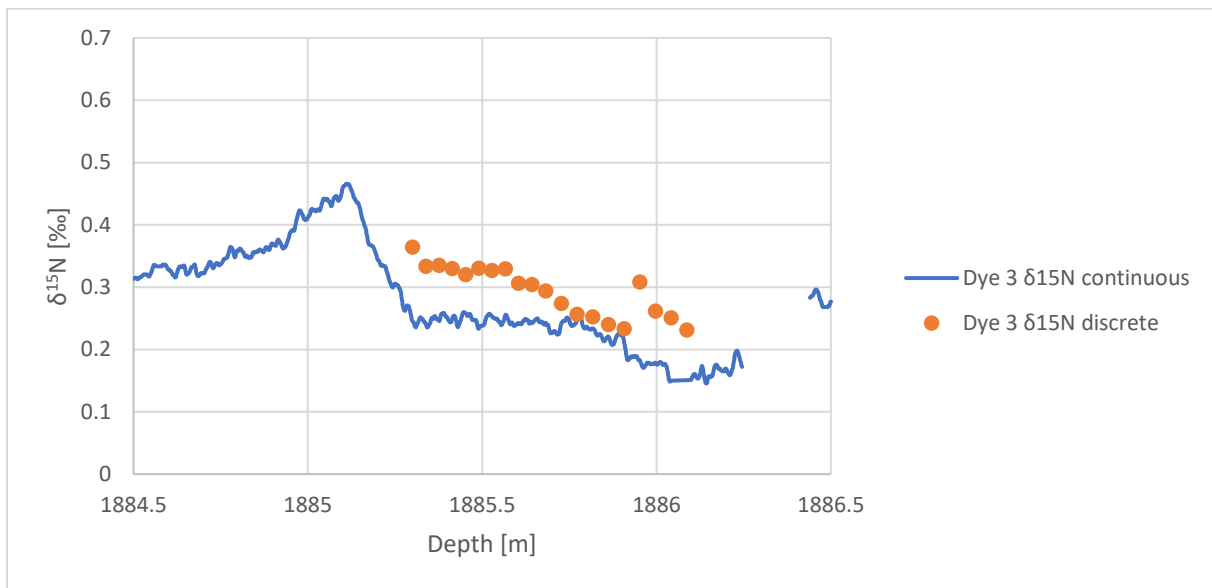


Figure 4.17: Comparison of $\delta^{15}\text{N}$ of discrete and CFA measurements in depth zone 3 ranging from 1884.5 m to 1886.5 m.

For this third depth zone, the offset between CFA and discrete measurements is smaller in a part of the dataset around 1885.75 m and almost agree with the CFA data. The correlation seems to be affected by daily variation of the lab air. Generally, the data points agree trend-wise, but again the discrete samples are higher than the continuous data. Some data points in the discrete data show a steep downward trend that is not visible to that extent in the CFA data (around 1886 m). The offset for the last 4 discrete data points is higher than for the rest of the dataset and the trend seems steeper than in the CFA data. The difference between the two datasets is between 0.001 ‰ and 0.125 ‰. The mean offset between discrete and CFA $\delta^{15}\text{N}$ for this depth zone is $0.07 \text{ ‰} \pm 0.07 \text{ ‰}$ (2σ).

Zoom on the fourth depth zone

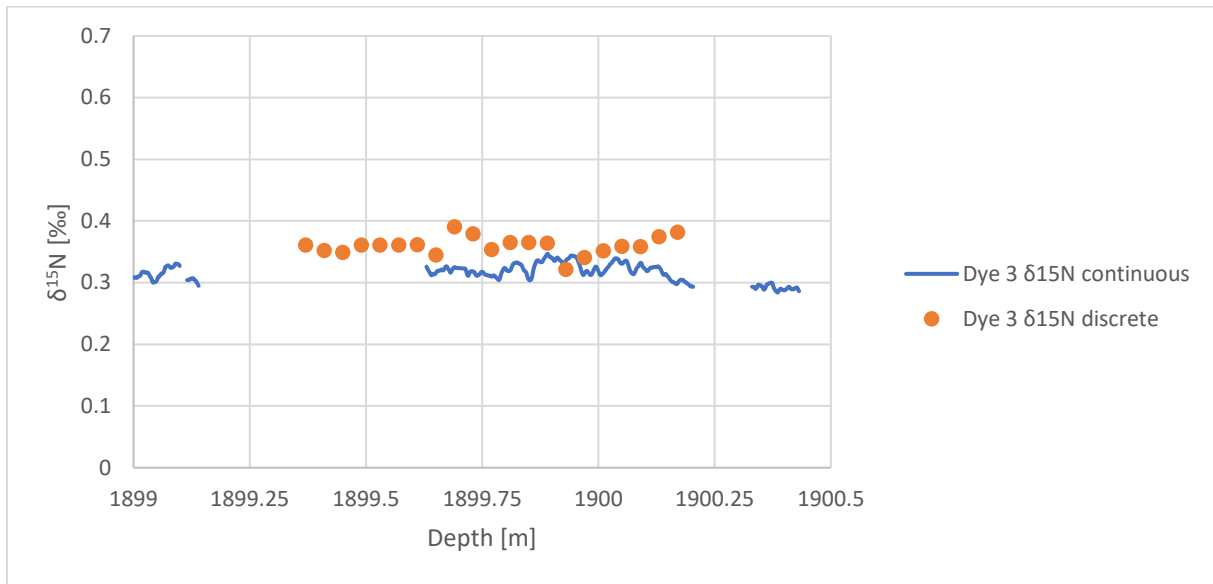


Figure 4.18: Comparison of $\delta^{15}N$ of discrete and CFA measurements in depth zone 4 ranging from 1899.0 m to 1900.5 m.

For this fourth depth zone, the discrete data agree visually relatively well with the CFA data. Some differences can be seen in the trends and generally the discrete data has higher values. The only exception is the point at 1899.96 m that lies even below the CFA data. While the CFA data shows a slight downward trend or stagnation, the discrete data indicates an increasing trend in $\delta^{15}N$ around 1900 m. The minimum offset between the two datasets is -0.015 ‰ and the maximum offset is 0.065 ‰. The mean offset between discrete and CFA $\delta^{15}N$ for this depth zone is $0.04\text{‰} \pm 0.07$ (2σ).

The overall mean offset over all 4 depth zones is $0.085\text{‰} \pm 0.094\text{‰}$ (2σ) and can be seen in Table 4.1, consequently the standard deviation even higher than the calculated mean offset.

The deviation between discrete and CFA $\delta^{15}N$ measurements is between 0.04 and 0.14 ‰ and the offset is not constant for the 4 analysed depth zones.

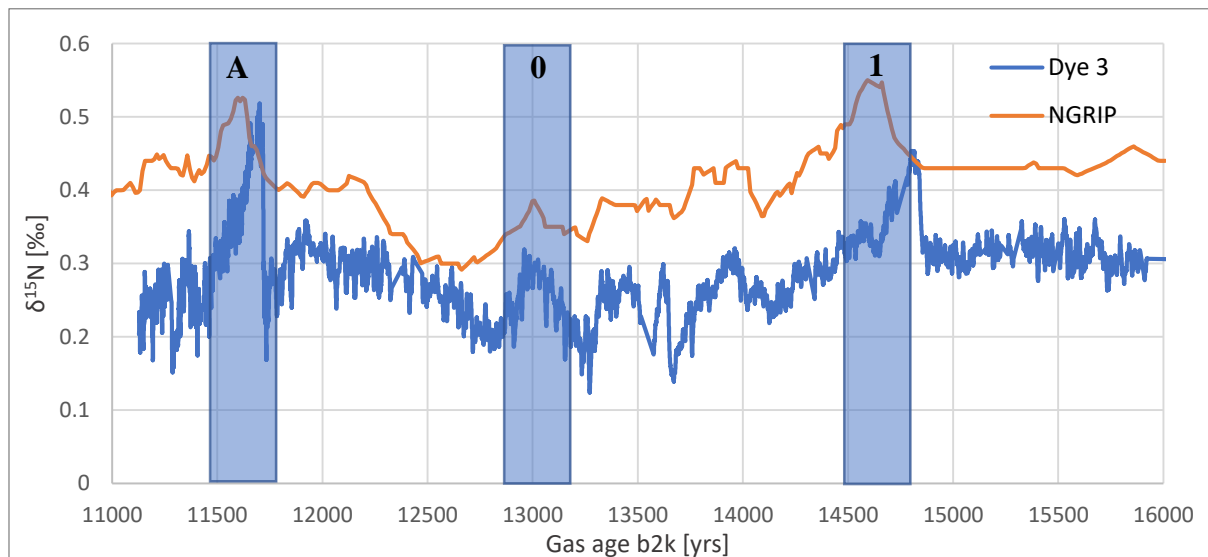
Depth zone	mean offset	2σ
1	0.09	0.07
2	0.14	0.08
3	0.07	0.07
4	0.04	0.04
Overall	0.09	0.09

Table 4.1: Mean offsets for the different depth zones and the 2σ standard deviation.

In principle, the discrete measurements could help to calibrate the CFA data and correct for the potential dissolution offset, but this requires more discrete measurements to bind it to. Additionally, a more stable laboratory air would probably result in a more stable offset that can be corrected for afterwards.

4.6 Comparison of Dye 3 $\delta^{15}\text{N}$ with NGRIP $\delta^{15}\text{N}$

The North GRenland Ice sheet Project (NGRIP) ice core was drilled in Northern-Central Greenland at 75.1°N 42.3°W between 1996 and 2004 (Andersen et al., 2004). The NGRIP $\delta^{15}\text{N}$ and gas age assignment of NGRIP were provided by Bo Vinther through personal communication and the data was published by Kindler et al., (2014). The CFA $\delta^{15}\text{N}$ record of Dye 3 is plotted against the preliminary gas age scale.



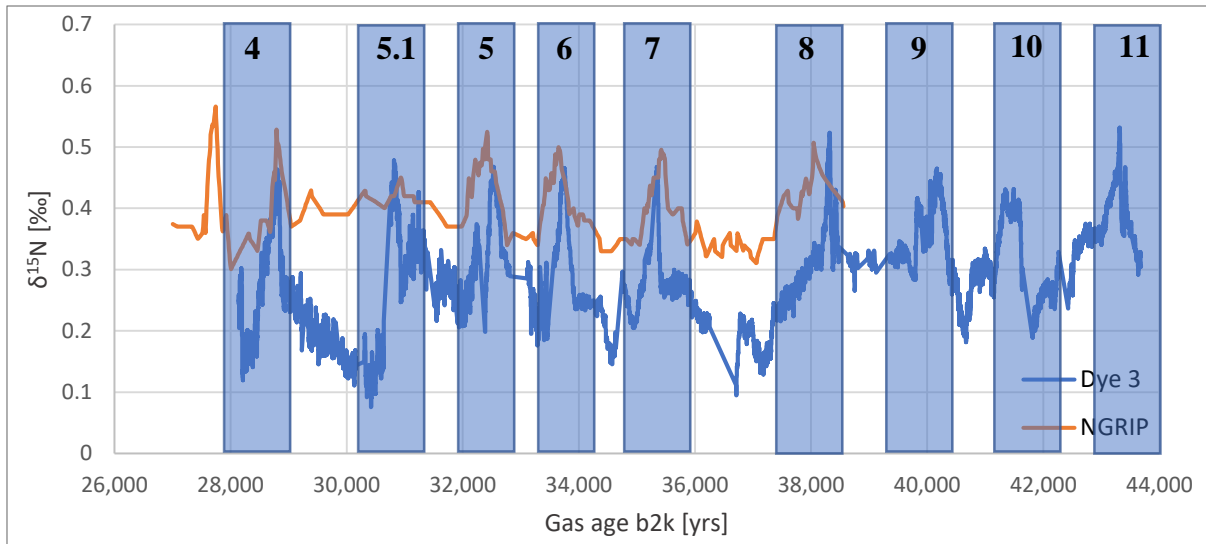


Figure 4.19 and Figure 4.20: $\delta^{15}\text{N}$ from this study plotted on a (preliminary) gas age scale for Dye 3. NGRIP $\delta^{15}\text{N}$ is plotted for comparison for the period 11,000 to 16,000 years b2k (Figure 4.19) and 26,000 to 44,000 years b2k (Figure 4.20)

As it can be seen in Figure 4.19 and Figure 4.20, the $\delta^{15}\text{N}$ values are generally lower for CFA measurements of Dye 3 because of differences in location, firn column depth, accumulation and temperatures of the two ice core drilling sites. The observed variations $\delta^{15}\text{N}$ for both ice core drill sites are mainly a result of thermal fractionation and gravitational settling (Severinghaus et al., 1998).

The present-day conditions show a mean annual temperature of -20°C for Dye 3 and -31.1°C for NGRIP whereas a lower temperature (and accumulation) results in a deeper firn column and therefore higher $\delta^{15}\text{N}$ values due to gravitational settling (Severinghaus et al., 1998).

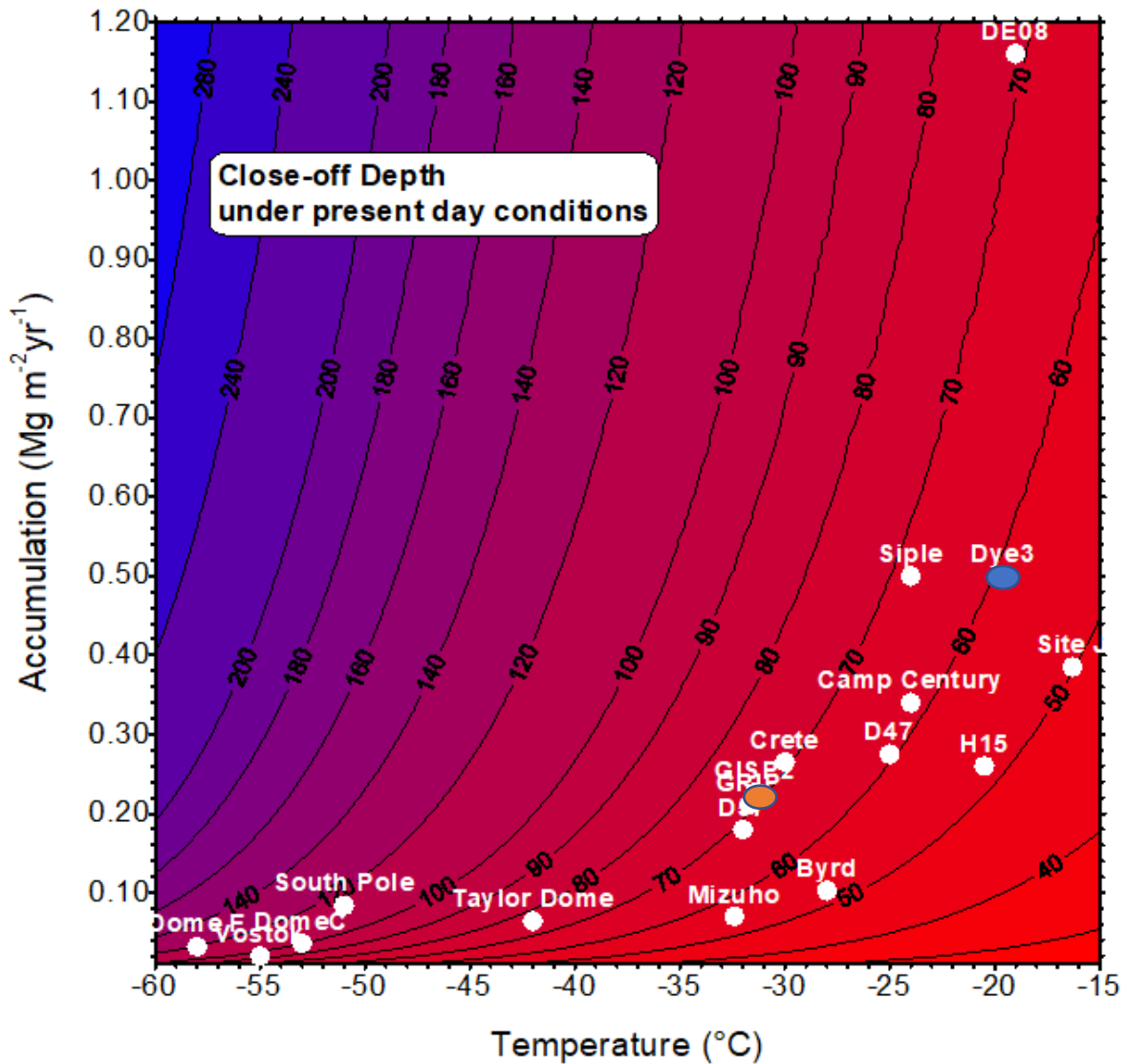


Figure 4.21: Accumulation rates, mean annual temperature and firn depth at different ice core drill sites in Antarctica and Greenland. NGRIP is expected to be at a firn depth and temperature similar to GRIP and Crete at approximately 70 m and marked in orange. Dye 3 is marked in blue. (Provided by Thomas Blunier through personal communication, 2019 calculated in steady state with the Schwander model (Schwander et al., 1993)).

The present-day firn depth differs between both sites by approximately 10 meters, the close-off-depth (COD) for Dye 3 being approximately 60 m and for NGRIP approximately 70 m. This means that there is a higher gravitational settling due to the deeper firn column for NGRIP which additionally favours higher $\delta^{15}\text{N}$ values which can be seen as well in the Figure 4.22.

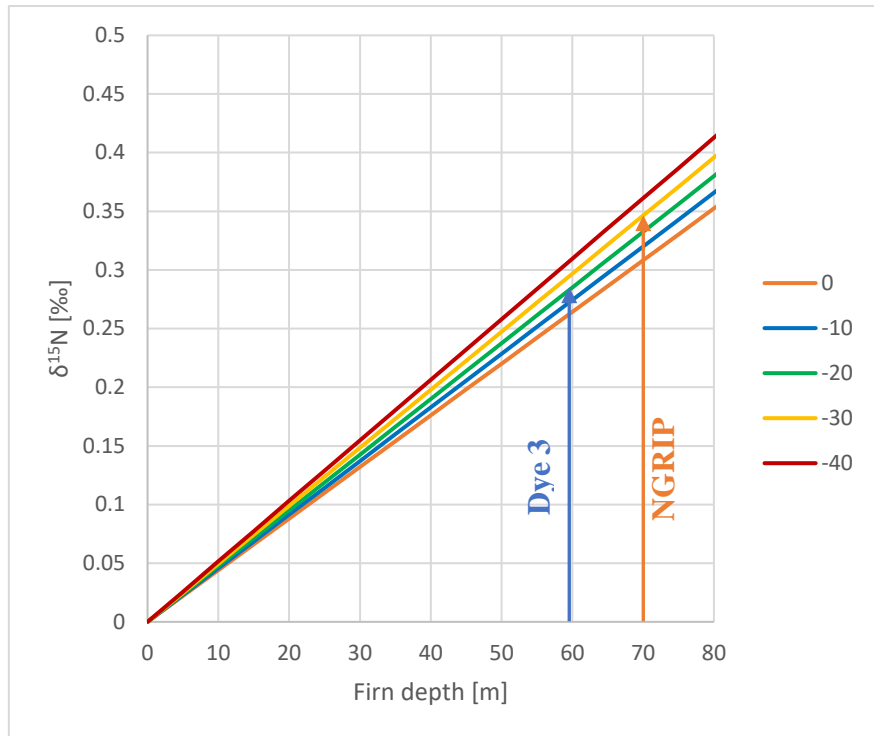


Figure 4.22: A calculation based on firn depth and surface temperatures calculated assuming steady state conditions taking into account gravitational settling and molecular diffusion. Calculated after equation 1.5 (gravitational settling).

Based on this model, the $\delta^{15}\text{N}$ values for NGRIP should be on average higher by 0.06 ‰ compared to Dye 3 if the present-day conditions are put into the model. The temperature is shown in 10°C-steps, consequently for NGRIP -30°C was chosen and therefore the actual difference might be slightly bigger as the mean surface temperature at NGRIP is -31.1°C.

	Dye 3 (60m, -20°C)	NGRIP (70m, -30°C)	NGRIP-Dye 3
Modelled $\delta^{15}\text{N}$	0.285 ‰	0.346 ‰	0.061 ‰

Table 4.2: Modelled $\delta^{15}\text{N}$ for Dye 3 and NGRIP based on present day firn properties and temperatures.

Another factor that might influence the difference in $\delta^{15}\text{N}$ between the two ice cores is probably the fact that the CFA $\delta^{15}\text{N}$ are lower than the discrete $\delta^{15}\text{N}$ samples for Dye 3 as shown before. The CFA $\delta^{15}\text{N}$ data will need to be corrected for this offset once the full Dye 3 discrete dataset is available. The measured mean $\delta^{15}\text{N}$ is 0.284 ‰ \pm 0.15 ‰ (2 σ) for Dye 3 and 0.400 ‰ \pm 0.08 ‰ (2 σ) for NGRIP indicates an average offset of 0.127 ‰ (including thermal fractionation and gravitational settling) between the two datasets.

It is assumed that a $\delta^{15}\text{N}$ difference was present as well during the last glacial period (including D-O events), but the extend may have varied. Further research is necessary to investigate the actual differences between the $\delta^{15}\text{N}$ signal of the two ice cores.

There are still some issues with the gas age assignment for Dye 3 for some events, as for example for D-O #1, the age assignment seems to be inappropriate so the gas age assignment needs to be improved so that it matches the NGRIP gas assignment more closely.

The Δ age is smaller for Dye 3 compared to NGRIP, because there is less mixing possible in the firn column due to a shallower firn column as a consequence of higher temperatures and higher accumulation rates for the Dye 3 site. This shallower firn column results in steeper increases seen for the D-O events and the Younger Dryas transition which brings up Dye 3 up to or even higher $\delta^{15}\text{N}$ values than NGRIP. Another reason for this steeper increase is the larger smoothing of the NGRIP data which makes transitions less pronounced and less steep.

4.7 Temperature reconstruction

The temperature reconstruction was done by inverting the Schwander et al., (1997) firn densification and heat diffusion model to fit the measured CFA $\delta^{15}\text{N}$ data from Dye 3. Hereby the model inversion was performed by using the fully automated fitting algorithm presented in Döring and Leuenberger (2018). Michael Döring has performed the temperature reconstruction for this thesis and provided the results for analysis.

In a first attempt, the second section of the measured $\delta^{15}\text{N}$ data covering the time period of 28,000 years to 44,500 years b2k was used for a preliminary temperature reconstruction from Dye 3 CFA $\delta^{15}\text{N}$.

The fitting algorithm needs two input values to model the surface temperature:

1) $\delta^{15}\text{N}$ and 2) accumulation rate.

- 1) The measured CFA $\delta^{15}\text{N}$ from this study was used as $\delta^{15}\text{N}$ input values. The final $\delta^{15}\text{N}$ was low-pass filtered by 200 years with a 200 year cut-off period to reduce noise being fitted for the reconstructed temperature.
- 2) The accumulation data for Dye 3 was provided by Bo M. Vinther through personal communication based on $\delta^{18}\text{O}$ by calculating a separate thinning function for the Holocene and glacial period to ensure a smooth transition for the whole ice core. The accumulation was fixed in the fitting process.

The algorithm changes the temperature iteratively with the aim to minimize the mismatch between measured and modelled $\delta^{15}\text{N}$ data. If a temperature solution generated the modelled $\delta^{15}\text{N}$ in a suitable way was found, this temperature estimate is a solution of the temperature

reconstruction procedure that is then used for the next attempt to further minimize the mismatch between modelled and observed $\delta^{15}\text{N}$.

The firm model by Schwander et al. (1997) was used to generate the modelled $\delta^{15}\text{N}$ based on the temperature and accumulation as input values. It then calculates the parameters (z_{LID} , T , T_{bottom} and T_{surf}) based on the following equations.

The equations in the model are the ones introduced previously for gravitational and thermal fractionation, whereas the $\delta^{15}\text{N}_{\text{mod}}$ is the sum of $\delta^{15}\text{N}_{\text{therm}}$ (equation 4.1) and $\delta^{15}\text{N}_{\text{grav}}$ (equation 4.2) as shown in equation 4.3.

$$\delta^{15}N_{\text{grav}}(z_{\text{LID}}, t) = \left(e^{\left(\frac{\Delta m * g * z_{\text{LID}}(t)}{R * T(t)} \right)} - 1 \right) * 1000 \quad (4.1)$$

$$\delta^{15}N_{\text{therm}}(t) = \left[\left(\frac{T_{\text{surf}}(t)}{T_{\text{bottom}}} \right)^{\alpha_T} - 1 \right] * 1000 \quad (4.2)$$

$$\delta^{15}N_{\text{mod}} = \delta^{15}N_{\text{grav}}(t) + \delta^{15}N_{\text{therm}}(t) \quad (4.3)$$

Where $\delta^{15}\text{N}_{\text{grav}}$ = part of the isotopic fractionation due to gravitational settling, z_{LID} = Lock-in-depth of the firm column, Δm = molecular mass difference between the light and heavy isotope, g = gravitational acceleration, R = ideal gas law constant, T = mean temperature of the firm column.

$\delta^{15}\text{N}_{\text{therm}}$ = part of the isotopic fractionation due to thermal fractionation, T_{surf} = surface temperature, T_{bottom} = temperature at the bottom of the firm column, α_T = thermal diffusion constant for nitrogen.

$\delta^{15}\text{N}_{\text{mod}}$ = the modelled $\delta^{15}\text{N}$.

The measured and modelled $\delta^{15}\text{N}$ data are shown below in Figure 4.23.

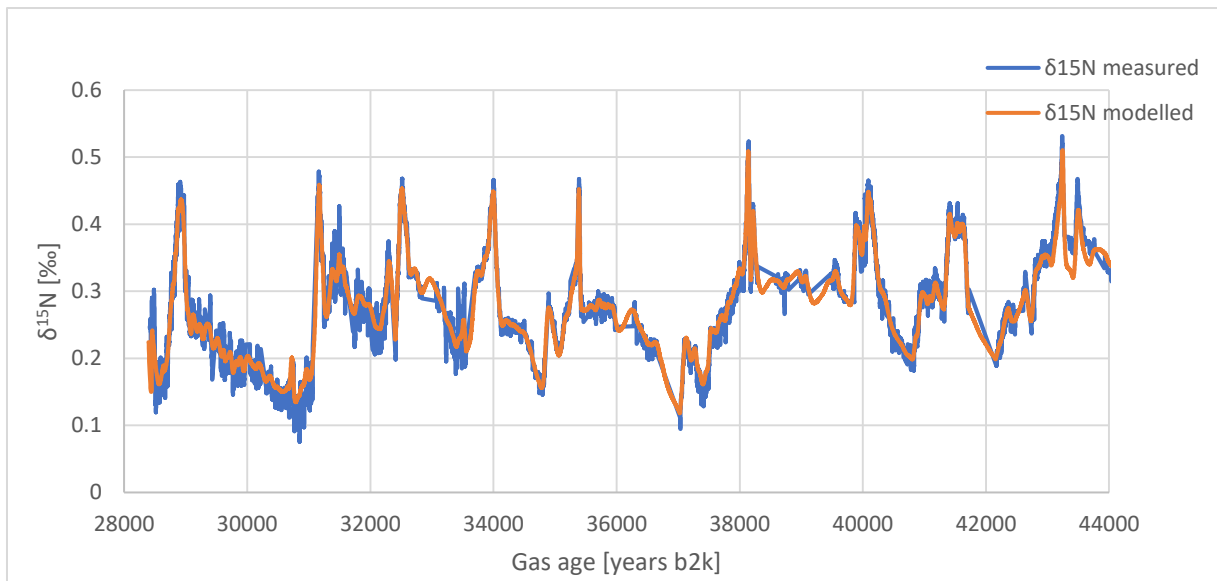


Figure 4.23: The measured and modelled $\delta^{15}\text{N}$ data on a gas age scale for 28,000 to 44,000 years b2k. Orange is the modelled data, blue is measured data.

The modelled $\delta^{15}\text{N}$ agrees very well with the measured CFA $\delta^{15}\text{N}$. The standard deviation of the modelled $\delta^{15}\text{N}$ is 30 per meg (0.030 ‰ based on 2σ) and therefore considerably smaller than the analytical uncertainty which is 100 per meg (0.1 ‰ based on 2σ). The input surface temperatures to model the previously shown $\delta^{15}\text{N}$ from 28,000 to 44,500 years b2k are shown in Figure 4.24 below.

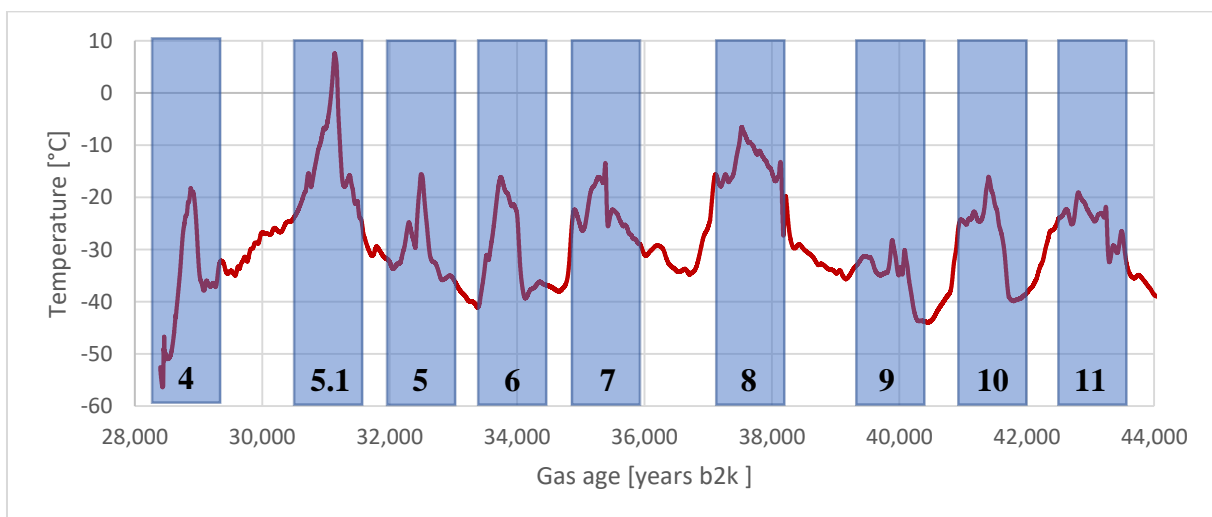


Figure 4.24: The temperature reconstruction based on the observed Dye 3 $\delta^{15}\text{N}$ values. The reconstructed temperature is shown in red. The observed D-O events 4-11 are marked in light blue and numbered.

The temperature amplitude for D-O event 5.1 seems unrealistic and is likely due to an error in the $\delta^{15}\text{N}$ data rather than in the fitting algorithm because it seems to be caused by a shift in the $\delta^{15}\text{N}$ data between the 4th November evening run and the 5th November in the morning. The lock-in-depth (LID) shown in Figure 4.25 is also unrealistically low (approximately 27 m) which

indicates that there is a problem with the $\delta^{15}\text{N}$ data. There could be a drift in the $\delta^{15}\text{N}$ data as well because there was a constant decrease during this run, maybe a drift correction might lead to more realistic results.

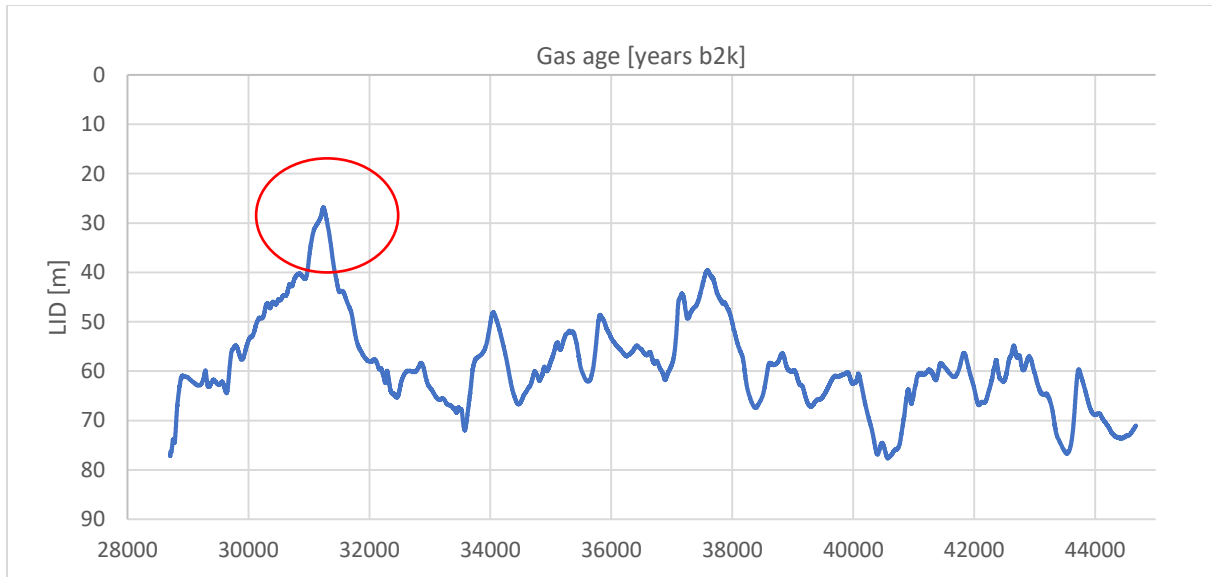


Figure 4.25: The modelled Lock-In-Depth (LID) based on the CFA $\delta^{15}\text{N}$ values. The LID for D-O event 5.1 is marked in red.

In the following section, the temperature amplitude for the observed D-O events was calculated and is shown in Table 4.3 below. The onset and peaks of the D-O events were chosen visually, and the amplitude was calculated by subtracting the peak temperature from the onset temperature:

$$\Delta T_{P-O} = T_{onset} - T_{peak} \quad (4.4)$$

D-O event	$T_{onset}[^{\circ}\text{C}]$	$T_{peak}[^{\circ}\text{C}]$	$T_{onset-peak}[^{\circ}\text{C}]$
4	-50.82	-18.92	31.9
5.1	-37.16	7.85	45.01
5	-33.69	-15.56	18.13
6	-40.35	-16.22	24.13
7	-37.62	-14.12	23.5
8	-34.34	-6.69	27.65
9	-34.87	-28.56	6.31
10	-43.95	-16.19	27.76
11	-39.59	-19.66	19.93
Average D-O event warming			22.41

Table 4.3: Onset temperature (T_{onset}), peak temperature (T_{peak}) and the temperature difference between onset and peak ($T_{onset-peak}$) for the D-O events from 28,000 to 44,000 years b2k.

D-O event 5.1 (marked in red) was excluded from this evaluation due to unrealistically high temperature values (approx. $+7^{\circ}\text{C}$ peak temperature and 45°C warming from the onset). The LID for this event is also extremely low with approximately 27 m.

D-O event 4 should be also looked at with precaution, as it was the evening run from the 4th November with argon turned off in the morning which was still slightly off in terms of delta values. On average, the warming for D-O events is 22.41°C from the onset to the peak (excluding D-O event 5.1). If D-O event 4 is excluded as well, the average warming between onset and peak is 21.05°C .

In the following section, the NGRIP temperature reconstruction by Kindler et al. (2014) based on $\delta^{15}\text{N}$ is compared to the previously presented Dye 3 temperature reconstruction to quantify the modelled temperature difference between the two locations. The NGRIP temperature amplitude for D-O events was subtracted from the previously calculated temperature amplitude for Dye 3 to get the difference between the two ice cores.

$$\Delta T_{Dye\ 3-NGRIP} = \Delta T_{Dye\ 3} - \Delta T_{NGRIP} \quad (4.5)$$

The calculated differences between NGRIP and Dye 3 modelled temperatures are shown in Figure 4.26 below.

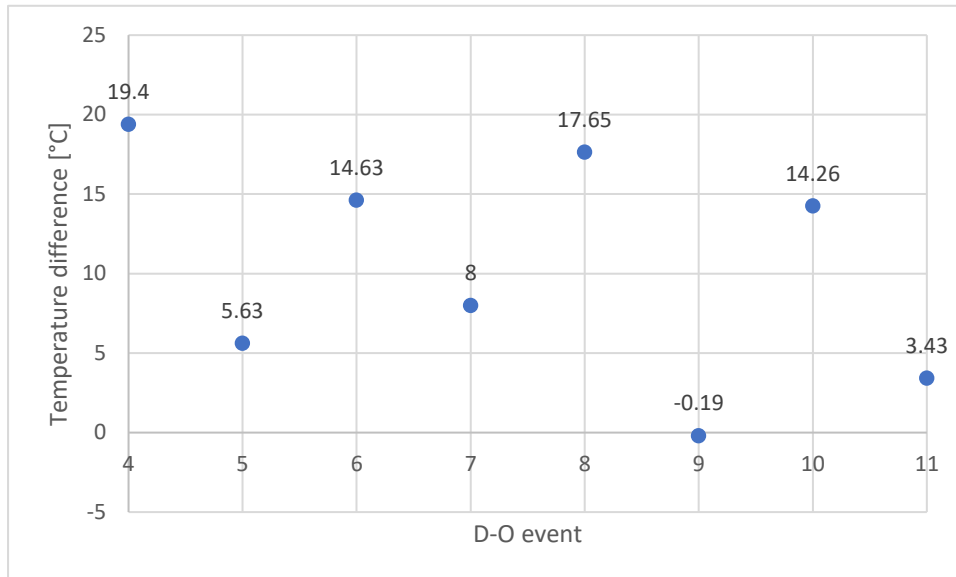


Figure 4.26: The temperature amplitude difference from Dye 3 to NGRIP for the measured D-O events (28,000 to 44,000 b2k). The NGRIP temperature reconstruction was done by Kindler et al. (2014). The NGRIP temperature reconstruction can be seen in Figure 1.1,

Variation in the temperature amplitude of the D-O events can be seen between the two ice core drill sites. The temperature amplitudes vary between similar temperatures for D-O event 9 and 19.4°C higher temperatures for Dye 3 for D-O event 4. The average temperature amplitude for Dye 3 compared to NGRIP based on $\delta^{15}\text{N}$ is 10.35°C higher (9.06°C when excluding D-O 4 and D-O event 5.1 from the average value). Higher temperature variation would be expected for Dye 3 because of the lower altitude and latitude of the drill site and a relative proximity to the ocean (as explained in chapter 4.6 and chapter 1.3). A larger influence of changes in ocean circulation can be observed for Dye 3 which results in more pronounced temperature and accumulation changes. D-O event 9 also deserves attention because the observed temperature difference shows a slightly higher temperature for NGRIP against the general trend of Dye 3 having higher temperatures for all other D-O events. The difference is rather small, so based on the current temperature reconstruction, both ice cores have similar temperatures for D-O event 9 which could be investigated more in the future.

The uncertainty of the temperature reconstruction was not calculated yet because many of the depending uncertainties were not available. It depends on the accumulation uncertainty (1) which is unknown because the accumulation data is preliminary. Furthermore, it depends on the firn model uncertainty (2). The analytical uncertainty of the CFA $\delta^{15}\text{N}$ was calculated to be $\pm 0.1 \text{ ‰}$ (2 σ). (3) The drifts in the $\delta^{15}\text{N}$ data between measurement runs are not well understood

and add to the uncertainty of the temperature reconstruction. And finally, there is an age uncertainty (4) of the gas age assignment because there are some sections with leading gas ages. This needs to be fixed before the final uncertainty of the temperature reconstruction can be calculated. Furthermore, the discrete Δ age can help to improve the temperature estimate and accumulation rate. The CFA $\delta^{15}\text{N}$ can be corrected based on the discrete samples by Todd Sowers so that the temperature reconstruction becomes more accurate. Independently from all the potential improvements and uncertainty estimations, the first section including the Younger Dryas transition, the B-A event and the first D-O event 1 will be modelled in future work.

5 Suggestions for future improvements

With this study, it was shown that simultaneous gas CFA measurements (CH_4 and $\delta^{15}\text{N}$, $\delta^{40}\text{Ar}$, $\delta\text{Ar}/\text{N}_2$) in addition to wet chemistry parameters are possible and lead to reliable results. This was done by melting a 108 m long section of the Dye 3 ice core in two weeks in fall 2019 and a high-resolution isotopic record was obtained.

A few challenges were identified during the measurements of the isotopes and data evaluation and therefore points of improvements for future research projects are suggested to get a more accurate record, especially in terms of $\delta^{40}\text{Ar}$, from isotopic CFA measurements:

- A better planning beforehand is necessary regarding what data we need e.g. measurements with and without CO_2 removal and with or without the perovskite membrane to confirm the baseline of the measurements with and without these removals. The objective of these tests is to confirm that improved data quality is achieved by implementing those removals.
- A more consistent and descriptive lab book is required with more detailed descriptions what was done and when to be able to better identify drivers of variation in the data that were observed.
- Another attempt could be made to implement the vacuum solution for the oxygen removal setup which would result in higher removal efficiencies and would also benefit the extraction efficiency of the MicroModule due to a higher pressure gradient from the gas extraction to the IRMS.
- A stable reference air is needed to bind the results to an absolute scale. The air could be better ventilated or taken from outside the laboratory.
- Additionally, it would be suggested to include the CH_4 , argon and nitrogen in one single and stable bottled standard, so that the standard calibration can be done simultaneously to have more time efficient calibrations. This would also reduce the potential “human error” as seen with the argon being turned off after the weekend in the morning of the 4th November 2019.
- The same treatment of the standard gas and sample would be suggested in order to have similar fractionation processes both for standard and sample like in the Huber et al. (2004) setup. Both standard and sample should go through the perovskite membrane, the cryotrap and Nafion membrane.

- Furthermore, it is suggested that no changes should be implemented while the system is running and already collecting sample data to facilitate the correction process afterwards.

With these improvements implemented, it should be possible to get better quality data and additionally a more time efficient sampling process.

Conclusion

The firm of ice sheets and glaciers retains information about past atmospheric temperatures stored in the gas bubbles trapped of the ice caused by thermal fractionation and gravitational settling. These changes can be observed when an ice core is melted and the gas bubbles are analyzed by mass spectrometry.

This thesis project developed successfully a system to access simultaneously $\delta^{15}\text{N}$, $\delta^{40}\text{Ar}$, $\delta\text{Ar}/\text{N}_2$, CH_4 and wet chemistry parameters from the Dye 3 ice core. It was shown that the simultaneous sampling of the pre-mentioned parameters works well and that the obtained data is generally of appropriate quality. The $\delta^{15}\text{N}$ results reflect generally the expected signals for rapid climate changes during the last glacial period (D-O events) in the firm. DO events 0,1 and 4-11 as well as the Younger Dryas transition were identified and confirmed based on a comparison with $\delta^{18}\text{O}$ (ice) and the methane record from this melting campaign. The measurement uncertainty for $\delta^{15}\text{N}$ was 0.1 ‰ (2 σ).

In comparison with the discrete $\delta^{15}\text{N}$ measurements by Todd Sowers, the CFA $\delta^{15}\text{N}$ were constantly slightly too low by on average 0.09 ‰. The CFA data could be corrected once the full discrete dataset is available.

A comparison with NGRIP $\delta^{15}\text{N}$ was done to see the differences between the ice two cores. The NGRIP values were constantly higher than Dye 3. According to a simple firm model, the difference for between the two cores should be in the order of 0.06 ‰ based on present day close-off-depth and mean annual temperature at the two drill sites (only accounting for gravitational settling in steady state conditions). The measured difference in $\delta^{15}\text{N}$ between NGRIP and Dye 3 is 0.13 ‰.

The $\delta^{40}\text{Ar}$ data were unfortunately highly influenced by a potentially unstable laboratory air standard and were consequently not analyzed further. Consequently, they were excluded for the temperature reconstruction.

The removal of oxygen and CO_2 was relatively constant over the measurement period. The only exception is a spike in the CO_2 removal which did not seem to have influenced the sample data of $\delta^{15}\text{N}$ and $\delta^{40}\text{Ar}$. There was a slight downward trend visible for the O_2 removal during the two measurement weeks with no explanation based on our current base of knowledge. Further investigation is necessary to identify the potential cause for this increase of oxygen removal over time.

Based on the fitting algorithm by (Döring and Leuenberger, 2018) and the firm model by (Schwander et al., 1997), the $\delta^{15}\text{N}$ data from this study was used as the target values to invert temperatures of Dye 3 back in time from 28,000 to 44,000 years b2k. D-O event temperatures were calculated by subtracting the peak temperatures and the mean D-O event warming was found to be approximately 22°C between onset and peak of the D-O event. D-O event 5.1 was not taken into consideration due to unrealistically high temperature values ($+7.5^\circ\text{C}$ peak temperature). This Dye 3 temperature reconstruction was compared with the $\delta^{15}\text{N}$ temperature reconstruction of NGRIP done by Kindler et al., (2014). The mean offset between the D-O events found for NGRIP and Dye 3 is 10.35°C which is comparable to the mean annual temperature difference for present day conditions.

The temperature reconstruction could be extended for both depth sections of Dye 3 that were analyzed. Moreover, the accuracy of the reconstruction can be further improved with an updated accumulation record, corrected $\delta^{15}\text{N}$ values based on the discrete $\delta^{15}\text{N}$ measurements and an improved gas age scale. Several future improvements were identified on the analytical part, notably a more stable laboratory air to bind the results to an absolute scale and a combined standard including argon with the CH_4 standard for more time efficient calibrations. Another attempt could be made to implement the vacuum solution for the oven setup for oxygen removal to have higher removal and a better gas extraction efficiency of the MicroModule.

Combined CFA measurements with gases (isotopes and concentrations) and wet chemistry parameters are more time efficient and give a higher resolution when compared to discrete sampling methods. Furthermore, less sample is needed to analyze many parameters simultaneously such as wet chemistry as well as CH_4 and nitrogen and argon isotopes in the same sample. Consequently, it represents an interesting area of research that deserves more investigation in the future.

Finally, it is important to understand drivers of past climate changes in order to predict the future of human-induced climate change. The world is currently undergoing an extremely fast human induced climate change similar to D-O events in the glacial period. By combining ice sheet modelling and reconstructed temperatures from ice cores it is possible to model sea level rise and contribute to adaptation strategies in coastal regions worldwide.

References

- Andersen, K.K., Azuma, N., Barnola, J.-M., Bigler, M., Biscaye, P., Caillon, N., Chappellaz, J., Clausen, H.B., Dahl-Jensen, D., Fischer, H., Flückiger, J., Fritzsche, D., Fujii, Y., Goto-Azuma, K., Grønvold, K., Gundestrup, N.S., Hansson, M., Huber, C., Hvidberg, C.S., Johnsen, S.J., Jonsell, U., Jouzel, J., Kipfstuhl, S., Landais, A., Leuenberger, M., Lorrain, R., Masson-Delmotte, V., Miller, H., Motoyama, H., Narita, H., Popp, T., Rasmussen, S.O., Raynaud, D., Röthlisberger, R., Ruth, U., Samyn, D., Schwander, J., Shoji, H., Siggard-Andersen, M.-L., Steffensen, J.P., Stocker, T., Sveinbjörnsdóttir, A.E., Svensson, A., Takata, M., Tison, J.-L., Thorsteinsson, T., Watanabe, O., Wilhelms, F., White, J., 2004. High-resolution record of the Northern Hemisphere climate extending into the last interglacial period. *Nature* 431, 147–151.
- Badgeley, J.A., Steig, E.J., Hakim, G.J., Fudge, T.J., 2020. Greenland temperature and precipitation over the last 20000 years using data assimilation. *Climate of the Past* 16, 1325–1346. <https://doi.org/10.5194/cp-16-1325-2020>
- Baldtzer Liisberg, J., 2020. Abrupt climate change and the nitrogen cycle. University of Copenhagen, Copenhagen.
- Blunier, T., Schwander, J., 2000. Gas enclosure in ice : age difference and fractionation. *Physics of Ice Core Records* 21.
- Bond, G., Heinrich, H., Broecker, W., Labeyrie, L., Mcmanus, J., Andrews, J., Huon, S., Jantschik, R., Clasen, S., Simet, C., Tedesco, K., Klas, M., Bonani, G., Ivy, S., 1992. Evidence for Massive Discharges of Icebergs into the North-Atlantic Ocean During the Last Glacial Period. *Nature* 360, 245–249. <https://doi.org/10.1038/360245a0>
- Broecker, W.S., Peteet, D.M., Rind, D., 1985. Does the ocean–atmosphere system have more than one stable mode of operation? *Nature* 315, 21–26.
- CIC, 2008a. History of ice core drilling in Greenland [WWW Document]. URL http://www.iceandclimate.nbi.ku.dk/research/drill_analysing/history_drilling/ (accessed 7.15.20).
- CIC, 2008b. The central Greenland ice cores [WWW Document]. URL http://www.iceandclimate.nbi.ku.dk/research/drill_analysing/history_drilling/central_ice_cores/ (accessed 7.15.20).
- CIC, 2008c. The search for Eemian ice [WWW Document]. URL http://www.iceandclimate.nbi.ku.dk/research/drill_analysing/history_drilling/search_eemian/ (accessed 7.15.20).
- Craig, H., Horibe, Y., Sowers, T., 1988. Gravitational Separation of Gases and Isotopes in Polar Ice Caps. *Science* 242, 1675–1678. <https://doi.org/10.1126/science.242.4886.1675>
- Dansgaard, W., 2004. Frozen annals: Greenland ice cap research. Narayana Press.
- Döring, M., Leuenberger, M.C., 2018. Novel automated inversion algorithm for temperature reconstruction using gas isotopes from ice cores. *Clim. Past* 14, 763–788. <https://doi.org/10.5194/cp-14-763-2018>
- Fuhrer, K., Neftel, A., Anklin, M., Maggi, V., 1993. Continuous measurements of hydrogen peroxide, formaldehyde, calcium and ammonium concentrations along the new grip ice core from summit, Central Greenland. *Atmospheric Environment. Part A. General Topics* 27, 1873–1880. [https://doi.org/10.1016/0960-1686\(93\)90292-7](https://doi.org/10.1016/0960-1686(93)90292-7)

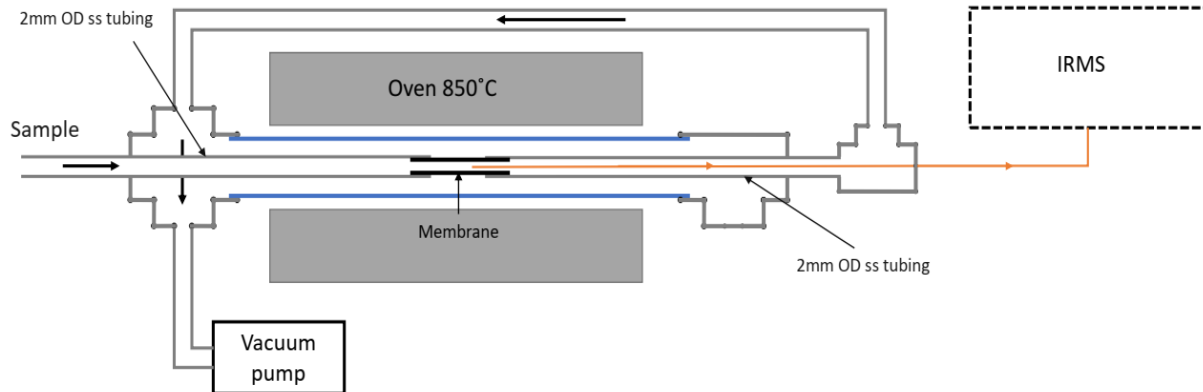
- Herron, M.M., Langway, C.C., 1980. Firm Densification: An Empirical Model. *Journal of Glaciology* 25, 373–385. <https://doi.org/10.3189/S0022143000015239>
- Hoefs, J., 2009. *Stable isotope geochemistry*. Springer.
- Huber, C., Leuenberger, M., 2004. Measurements of isotope and elemental ratios of air from polar ice with a new on-line extraction method. *Geochemistry, Geophysics, Geosystems* 5. <https://doi.org/10.1029/2004GC000766>
- Johnsen, S.J., Dahl-Jensen, D., Gundestrup, N., Steffensen, J.P., Clausen, H.B., Miller, H., Masson-Delmotte, V., Sveinbjörnsdóttir, A.E., White, J., 2001. Oxygen isotope and palaeotemperature records from six Greenland ice-core stations: Camp Century, Dye-3, GRIP, GISP2, Renland and NorthGRIP. *Journal of Quaternary Science* 16, 299–307. <https://doi.org/10.1002/jqs.622>
- Kindler, P., Guillevic, M., Baumgartner, M.F., Schwander, J., Landais, A., Leuenberger, M., 2014. Temperature reconstruction from 10 to 120 kyr b2k from the NGRIP ice core. *Climate of the Past* 10, 887–902.
- Kobashi, T., Severinghaus, J.P., Kawamura, K., 2008. Argon and nitrogen isotopes of trapped air in the GISP2 ice core during the Holocene epoch (0–11,500 B.P.): Methodology and implications for gas loss processes. *Geochimica et Cosmochimica Acta* 72, 4675–4686. <https://doi.org/10.1016/j.gca.2008.07.006>
- Krebs, R.E., 2006. *The History and Use of Our Earth's Chemical Elements: A Reference Guide*. Greenwood Publishing Group.
- Landais, A., Barnola, J.M., Masson-Delmotte, V., Jouzel, J., Chappellaz, J., Caillon, N., Huber, C., Leuenberger, M., Johnsen, S.J., 2004. A continuous record of temperature evolution over a sequence of Dansgaard-Oeschger events during Marine Isotopic Stage 4 (76 to 62 kyr BP). *Geophysical Research Letters* 31. <https://doi.org/10.1029/2004GL021193>
- Lang, C., Leuenberger, M., Schwander, J., Johnsen, S., 1999. 16°C Rapid Temperature Variation in Central Greenland 70,000 Years Ago. *Science* 286, 934–937. <https://doi.org/10.1126/science.286.5441.934>
- Liang, F., Jiang, H., Schiestel, T., Caro, J., 2010. High-Purity Oxygen Production from Air Using Perovskite Hollow Fiber Membranes. *Ind. Eng. Chem. Res.* 49, 9377–9384. <https://doi.org/10.1021/ie101311g>
- Masson-Delmotte, T.W.V., Zhai, P., Pörtner, H.O., Roberts, D., Skea, J., Shukla, P.R., Pirani, A., Moufouma-Okia, W., Péan, C., Pidcock, R., 2018. IPCC, 2018: Summary for Policymakers. In: *Global warming of 1.5 C. An IPCC Special Report on the impacts of global warming of 1.5 C above pre-industrial levels and related global greenhouse gas emission pathways, in the context of strengthening the global*. World Meteorological Organization, Geneva, Tech. Rep.
- Niels Bohr Institute, 2016. EastGRIP - The East Greenland Ice-core Project [WWW Document]. URL <https://eastgrip.nbi.ku.dk/> (accessed 7.15.20).
- Rahmstorf, S., 2002. Ocean circulation and climate during the past 120,000 years. *Nature* 419, 207–214. <https://doi.org/10.1038/nature01090>
- Röthlisberger, R., Bigler, M., Hutterli, M., Sommer, S., Stauffer, B., Junghans, H.G., Wagenbach, D., 2000. Technique for Continuous High-Resolution Analysis of Trace Substances in Firn and Ice Cores. *Environ. Sci. Technol.* 34, 338–342. <https://doi.org/10.1021/es9907055>

- Schüpbach, S.S., Federer, U., Kaufmann, P.R., Hutterli, M.A., Buiron, D., Blunier, T., Fischer, H., Stocker, T.F., 2009. A New Method for High-Resolution Methane Measurements on Polar Ice Cores Using Continuous Flow Analysis. *Environ. Sci. Technol.* 43, 5371–5376. <https://doi.org/10.1021/es9003137>
- Schwander, J., 1989. The Transformation of Snow to Ice and the Occlusion of gases. *The Environmental Record in Glaciers and Ice Sheets* pp.53-67.
- Schwander, J., Barnola, J.-M., Andrié, C., Leuenberger, M., Ludin, A., Raynaud, D., Stauffer, B., 1993. The age of the air in the firn and the ice at Summit, Greenland. *Journal of Geophysical Research: Atmospheres* 98, 2831–2838. <https://doi.org/10.1029/92JD02383>
- Schwander, J., Sowers, T., Barnola, J.-M., Blunier, T., Fuchs, A., Malaizé, B., 1997. Age scale of the air in the summit ice: Implication for glacial-interglacial temperature change. *Journal of Geophysical Research: Atmospheres* 102, 19483–19493. <https://doi.org/10.1029/97JD01309>
- Schwander, J., Stauffer, B., 1984. Age difference between polar ice and the air trapped in its bubbles. *Nature* 311, 45–47.
- Severinghaus, J.P., Grachev, A., Luz, B., Caillon, N., 2003. A method for precise measurement of argon 40/36 and krypton/argon ratios in trapped air in polar ice with applications to past firn thickness and abrupt climate change in Greenland and at Siple Dome, Antarctica. *Geochimica et Cosmochimica Acta* 67, 325–343. [https://doi.org/10.1016/S0016-7037\(02\)00965-1](https://doi.org/10.1016/S0016-7037(02)00965-1)
- Severinghaus, J.P., Sowers, T., Brook, E.J., Alley, R.B., Bender, M.L., 1998. Timing of abrupt climate change at the end of the Younger Dryas interval from thermally fractionated gases in polar ice. *Nature* 391, 141–146. <https://doi.org/10.1038/34346>
- Sigg, Andreas., Fuhrer, Katrin., Anklin, Martin., Staffelbach, Thomas., Zurmuehle, Daniel., 1994. A continuous analysis technique for trace species in ice cores. *Environ. Sci. Technol.* 28, 204–209. <https://doi.org/10.1021/es00051a004>
- Sowers, T., Bender, M., Raynaud, D., 1989. Elemental and isotopic composition of occluded O₂ and N₂ in polar ice. *Journal of Geophysical Research: Atmospheres* 94, 5137–5150. <https://doi.org/10.1029/JD094iD04p05137>
- Stoller-Conrad, J., 2017. Core questions: An introduction to ice cores [WWW Document]. *Climate Change: Vital Signs of the Planet*. URL <https://climate.nasa.gov/news/2616/core-questions-an-introduction-to-ice-cores> (accessed 8.10.20).
- Stowasser, C., Buizert, C., Gkinis, V., Chappellaz, J., Schüpbach, S., Bigler, M., Fäin, X., Sperlich, P., Baumgartner, M., Schilt, A., Blunier, T., 2012. Continuous measurements of methane mixing ratios from ice cores. *Atmospheric Measurement Techniques* 5, 999–1013. <https://doi.org/10.5194/amt-5-999-2012>
- Technical Glass Products Inc., n.d. Technical Glass Products: Properties of Fused Quartz [WWW Document]. *Technical Glass Products*. URL https://technicalglass.com/technical_properties/ (accessed 7.15.20).
- Thermo Fisher Scientific, n.d. Overview of Mass Spectrometry | Thermo Fisher Scientific - DK [WWW Document]. URL <https://www.thermofisher.com/dk/en/home/life-science/protein-biology/protein-biology-learning-center/protein-biology-resource-library/pierce-protein-methods/overview-mass-spectrometry.html> (accessed 7.15.20a).

- Thermo Fisher Scientific, n.d. DELTA V™ Isotope Ratio Mass Spectrometer [WWW Document]. URL <https://www.thermofisher.com/order/catalog/product/IQLAAEGAATFABHMZZZ> (accessed 7.15.20b).
- Venkatesh, J., 2020. An improved Gas-CFA system for methane measurements and preliminary results from the Dye-3 ice core. University of Copenhagen.
- Vladimirova, D., 2018. High-resolution methane record of the RECAP ice core (Eastern Greenland) over the last climatic cycle. Niels Bohr Institute, Centre for Ice and Climate 151.
- Weissler, G.L., Carlson, R.W., 1979. Methods of Experimental Physics - Vacuum Physics and Technology. Academic Press.

Appendix

Appendix 1. Oven setup showing the potential vacuum solution for oxygen removal



Appendix 1.: Alternative oven setup with a vacuum pump instead of the counter sample helium flow to carry the removed oxygen away.

The membrane is sealed on both ends to the 2 mm OD stainless steel tubing and there is a high partial pressure gradient across the membrane created by the vacuum pump that transports the extracted oxygen away. The sample capillary is pushed approx. 1 cm inside the membrane so that it can better measure the sample without the oxygen and does not get influenced by the helium flow.

Appendix 2. Main matlab script for data evaluation

```
%%Combining with Isotope data - David Soestmeyer (20/03/2020)
clc;
clear all;
close all;

[File1,Path1] = uigetfile('*.','Choose depth vs time file');
filename1 = strcat(Path1,File1);
Depth = readtable(filename1);
[File2,Path2] = uigetfile('*.','Choose isotope file');
filename2 = strcat(Path2,File2);
Isotope = readtable(filename2,'ReadVariableNames',true);
filename = '1816_daily_air_error_pinew_test1.txt';

%%
ratios = [0.740092659 0.323380425 0.832759842 0.072 -4.200
6.531 0.015 0.141 0.388]; % Here the daily ratio, delta value
and uncertainty for the lab air is plotted, in the order 15N, 36Ar,
Ar/N2
ratio29std=ratios(1);
```

```

ratio36std=ratios(2);
ratio40std=ratios(3);
delta29std=ratios(4);
delta36std=ratios(5);
delta40std=ratios(6);
e_std29 = ratios(7);
e_std36 = ratios(8);
e_std40 = ratios(9);

time = Isotope.time(50:end);
int_28 = Isotope.int_28;
int_29 = Isotope.int_29;
int_32 = Isotope.int_32;
int_36 = Isotope.int_36;
int_40 = Isotope.int_40;
int_44 = Isotope.int_44;
breaks = Depth.breaks;
newbag = Depth.newbag;

data28 = int_28(50:end) - mean(int_28(15:28));
data29 = int_29(50:end) - mean(int_29(15:28));
data32 = int_32(50:end) - mean(int_32(15:28));
data36 = int_36(50:end) - mean(int_36(15:28));
data40 = int_40(50:end) - mean(int_40(15:28));
data44 = int_44(50:end) - mean(int_44(15:28));
%%
% drift correction 4th only
Dr=-1;
dt=0.706279;
for i = 1:length(data40)
    data40(i)=data40(i)-1/(Dr*(time(i)-dt));
end

%
%%
Delta = 100; %Defines how much difference between datapoints you
need
%before defining actual data, instead of backgroundnoise only

% finding the indexes for at what points data shifts to and from
standard
in = [];
dy = [];
l=0;
for i = 2:length(data28)
    if abs(data28(i)-data28(i-1)) > Delta
        l=l+1;
        dy(l) = abs(data28(i)-data28(i-1)); % Getting the values too,
just in case
        in(l) = i; % Getting the indexes
    end
end

```

```

end
% Defining std and actual measurements

for i = 1:length(in)-1
ms2{i} = data28(in(i)+1:in(i+1));
end

ms28 = data28(in(1)+1:in(end));
ms29 = data29(in(1)+1:in(end));
ms36 = data36(in(1)+1:in(end));
ms40 = data40(in(1)+1:in(end));

std128 = data28(1:in(1));
std129 = data29(1:in(1));
std136 = data36(1:in(1));
std140 = data40(1:in(1));

std228 = data28(in(end):end);
std229 = data29(in(end):end);
std236 = data36(in(end):end);
std240 = data40(in(end) : end);

%% working std means

stdmean28 = (mean(std128) + mean (std228))/2;
stdmean40 = (mean(std140) + mean (std240))/2;

%% fitting for the std over time
fity28 = [mean(std128),mean(std228)];
fity29 = [mean(std129),mean(std229)];
fity36 = [mean(std136),mean(std236)];
fity40 = [mean(std140),mean(std240)];

fitx = [mean(linspace(1,in(1),in(1))),
mean(linspace(1,in(end),length(data28)))]];

fit28 = fit(fitx',fity28','poly1'); % making a fit
fit29 = fit(fitx',fity29','poly1');
fit36 = fit(fitx',fity36','poly1');
fit40 = fit(fitx',fity40','poly1');

%%
precal_n15=(fity29(1)/fity28(1)/ratio29std-1)*1000;
postcal_n15=(fity29(2)/fity28(2)/ratio29std-1)*1000;

precal_ar36=(fity36(1)/fity40(1)/ratio36std-1)*1000;
postcal_ar36=(fity36(2)/fity40(2)/ratio36std-1)*1000;

precal_ar40=(fity40(1)/fity28(1)/ratio40std-1)*1000;
postcal_ar40=(fity40(2)/fity28(2)/ratio40std-1)*1000;

disp(precal_n15);
disp(postcal_n15);
disp(precal_ar36);
disp(postcal_ar36);
disp(precal_ar40);

```

```

disp(postcal_ar40);

% making a fit
%figure
%plot(fit1) % plotting to see it
a28 = fit28(1); % defining coefficients
b28 = fit28(2);

a29 = fit29(1);
b29 = fit29(2);

% a36 = fit36(1);
% b36 = fit36(2);
%
% a40 = fit40(1);
% b40 = fit40(2);
%
for m = 1:length(data28)

    data28(m) = data28(m)-(fit28(m)-fit28(mean(fitx)));
    data29(m) = data29(m)-(fit29(m)-fit29(mean(fitx)));
    % data36(m) = data36(m)-(fit36(m)-fit36(mean(fitx)));
    % data40(m) = data40(m)-(fit40(m)-fit40(mean(fitx)));
end
%%
D = Depth.mh_delay;
infmt = 'mm:ss.S';
mh_delay = duration(D, 'InputFormat', infmt);

%%
ms_delay = duration(00,02,18);

C_time11 = Depth.MHtime + ms_delay + mh_delay;
C_time22 = char(C_time11);
C_time111 = datetime(C_time22, 'InputFormat', 'HH:mm:ss');
C_time111.Format = 'HH:mm:ss.S';

for j = 1:length(C_time111)
    C_date111(j) = datetime(2019,10,31); %choose date of sample run!
end
C_date111 = C_date111';

CDT = C_date111 + timeofday(C_time111);
CDT.Format = 'HH:mm:ss.S';
CnewDT = dateshift(CDT, 'start', 'second', 'nearest');

ms_time = datetime(time, 'ConvertFrom', 'excel');
ms_time.Format = 'HH:mm:ss.S';
for i = 1:length(ms_time)
    ms_date(i) = datetime(2019,10,31); %choose date of sample run!
end

ms_date = ms_date';
IDT = ms_date + timeofday(ms_time);
IDT.Format = 'HH:mm:ss.S';

```

```

InewDT = dateshift(IDT, 'start', 'second', 'nearest');

%%
[LiA, LocB] = ismember(CnewDT, InewDT);

%%
depth = Depth.depthfinal;
methane = Depth.ch4final;
gaspercent = Depth.gascentmm;
timemh = Depth.MHtime;
timems = zeros(length(depth), 1);
iso_28 = zeros(length(depth), 1);
iso_29 = zeros(length(depth), 1);
iso_32 = zeros(length(depth), 1);
iso_36 = zeros(length(depth), 1);
iso_40 = zeros(length(depth), 1);
iso_44 = zeros(length(depth), 1);

for m = 1:length(depth)
    if LiA(m) > 0
        id(m) = LocB(m); %Finds index where Picarro time matches
        timems(m) = Isotope.time(id(m)); %Sets to value at that
index
        iso_28(m) = data28(id(m)); %Sets to value at that index
        iso_29(m) = data29(id(m));
        iso_32(m) = data32(id(m)); %Sets to value at that index
        iso_36(m) = data36(id(m));
        iso_40(m) = data40(id(m));
        iso_44(m) = data44(id(m));
    else
        timems(m) = timems(m-1);
        iso_28(m) = NaN; %Sets to NaN where times don't match
        iso_29(m) = NaN;
        iso_32(m) = NaN;
        iso_36(m) = NaN;
        iso_40(m) = NaN;
        iso_44(m) = NaN;
    end
end

%Removing data where depth is NaN (field end depth correction)
tfnan = isnan(depth);

for k = 1:length(depth)
    if tfnan(k) == 1
        timems(k) = timems(k-1);
        iso_28(k) = NaN; %Sets to NaN where times don't match
        iso_29(k) = NaN;
        iso_32(k) = NaN;
        iso_36(k) = NaN;
        iso_40(k) = NaN;
        iso_44(k) = NaN;
    end
end

%%

```

```

funcalc =
findRatioNerror(iso_28,iso_29,iso_36,iso_40,ratio29std,ratio36std,ra
tio40std,e_std29,e_std36,e_std40);

dms29 = funcalc(:,1); %corrected for pressure and chemical slope
dms36 = funcalc(:,2);
dms40 = funcalc(:,3);
e_dms29 = funcalc(:,4); %error of mass spec corrected values
e_dms36 = funcalc(:,5);
e_dms40 = funcalc(:,6);

delta29 = zeros(length(iso_28),1);
delta36 = zeros(length(iso_28),1);
delta40 = zeros(length(iso_28),1);

e_d29 = zeros(length(iso_28),1); % errors for the deltas
e_d36 = zeros(length(iso_28),1);
e_d40 = zeros(length(iso_28),1);

tfnan = isnan(iso_28);
for k = 1:length(iso_28)
    if tfnan(k) == 1
        delta29(k) = NaN;
        delta36(k) = NaN;
        delta40(k) = NaN;
        e_d29(k) = NaN;
        e_d36(k) = NaN;
        e_d40(k) = NaN;
    elseif tfnan(k) == 0
        delta29(k) = ((dms29(k)/1000+1)*(delta29std/1000+1)-1)*1000;
        delta40(k) = ((dms40(k)/1000+1)*(delta40std/1000+1)-1)*1000;
        delta36(k) = ((dms36(k)/1000+1)*(delta36std/1000+1)-1)*1000;

        e_d29(k) =
        (((delta29std/1000+1)*e_dms29(k))^2+((dms29(k)/1000+1)*e_std29)^2)^0
        .5;
        e_d36(k) =
        (((delta36std/1000+1)*e_dms36(k))^2+((dms36(k)/1000+1)*e_std36)^2)^0
        .5;
        e_d40(k) =
        (((delta40std/1000+1)*e_dms40(k))^2+((dms40(k)/1000+1)*e_std40)^2)^0
        .5;
    end
end
%%
gp=smooth(gaspercent,69);
e_gp = zeros(length(iso_28),1);
% E_gas= zeros(69,1);

for i = 69:(length(iso_28))
    E_gas = gaspercent(i-68:i);
    e_gp(i) = std(E_gas);
end
%%

```

```

funcalc =
setupcorrectionerror(delta29,delta36,delta40,gp,e_d29,e_d36,e_d40,e_
gp);

dsc29 = funcalc(:,1); %sample only pressure imbalance corrected
dsc36 = funcalc(:,2);
dsc40 = funcalc(:,3);

e_dsc29 = funcalc(:,4); %sample only pressure imbalance corrected
e_dsc36 = funcalc(:,5);
e_dsc40 = funcalc(:,6);

%%
IsoData =
table(depth,timemh,timems,methane,breaks,newbag,iso_28,iso_29,iso_32
,iso_36,iso_40,iso_44,dsc29,dsc36,dsc40,e_dsc29,e_dsc36,e_dsc40,gasp
ercent); % gascentmm);
writetable(IsoData,filename,'Delimiter',' '); %Saves as a text file

```

Appendix 3. Matlab script for applying the pressure imbalance and chemical slope corrections

```

function ans
=findRatioNerror(data28,data29,data36,data40,ratio29std,ratio36std,ratio40std,e_std29,e_std36,e_std40)

e_28 = 14.49; % uncertainty of the intensity as found on the of
31st 15:00-15:46
e_29 = 10.66; % uncertainty of the intensity as found on the of
31st 15:00-15:46
e_36 = 3.797; % uncertainty of the intensity as found on the of
31st 15:00-15:46
e_40 = 12.11; % uncertainty of the intensity as found on the of
31st 15:00-15:46

p29 = 1.046*10^-4; % constants for pressure imbalance correction
p36 = 6.76*10^-4;
p40 = 5.587E-04;

e_p29 = 2.07E-05; % errors for pressure imbalance correction
e_p36 = 1.55E-05;
e_p40 = 5.53E-05;

a = -1.78E-02; % constants for the chemical slope correction for
a function a*d^3+b*d^2+c*d
b = 9.59E-06;
%c = -0.016562565;

a_n15 = 4.97186E-05; % constants for the chemical slope
correction for a function a*d^3+b*d^2+c*d

e_a_n15= 3.03572E-06;

e_a = 4.5E-04; % error of the chemical slope constants
e_b = 1.4E-06;
%e_c = 0.000201539;

e_off28= e_28*2^0.5; % error of the offset
e_off40= e_40*2^0.5;

ratio29 = zeros(length(data28),1);
ratio36 = zeros(length(data28),1);
ratio40 = zeros(length(data28),1);

deltap29 = zeros(length(data28),1);
deltac29 = zeros(length(data28),1);
deltap36 = zeros(length(data28),1);
deltap40 = zeros(length(data28),1);
deltac36 = zeros(length(data28),1);

e_r29= zeros(length(data28),1); % error of the ratios
e_r36= zeros(length(data28),1);
e_r40= zeros(length(data28),1);

e_dp29 = zeros(length(data28),1); % error of delta p 29

```

```

e_dc29 = zeros(length(data28),1); % error of delta c 36
e_dp36 = zeros(length(data28),1); % error of delta p
e_dp40 = zeros(length(data28),1); % error of delta p
e_dc36 = zeros(length(data28),1); % error of delta c 36

%% defining ratio
tfnan = isnan(data28);
for k = 1:length(data28)
    if tfnan(k) == 1
        ratio29(k) = NaN;
        ratio36(k) = NaN;
        ratio40(k) = NaN;
        deltap29(k) = NaN;
        deltap36(k) = NaN;
        deltap40(k) = NaN;
        deltac36(k) = NaN;
        deltac29(k) = NaN;

        e_r29(k) = NaN;
        e_r36(k) = NaN;
        e_r40(k) = NaN;
        e_dp29(k) = NaN;
        e_dp36(k) = NaN;
        e_dp40(k) = NaN;
        e_dc36(k) = NaN;
        e_dc29(k) = NaN;

    elseif tfnan(k) == 0
        ratio29(k) = data29(k)./data28(k);
        ratio36(k) = data36(k)./data40(k);
        ratio40(k) = data40(k)./data28(k);

        e_r29(k) =
            ((1/data28(k)*e_29)^2+(data29(k)./data28(k)^2*e_28)^2)^0.5;
        e_r36(k) =
            ((1/data40(k)*e_36)^2+(data36(k)./data40(k)^2*e_40)^2)^0.5;
        e_r40(k) =
            ((1/data28(k)*e_40)^2+(data40(k)./data28(k)^2*e_28)^2)^0.5;

        deltap29(k) = ((ratio29(k)./ratio29std)-1)*1000-
            p29*(data28(k)-10500);
        deltap36(k) = ((ratio36(k)./ratio36std)-1)*1000-
            p36*(data40(k)-8900);
        deltap40(k) = ((ratio40(k)./ratio40std)-1)*1000-
            p40*(data40(k)-10500);
        deltac36(k) = deltap36(k)-(a*deltap40(k)+b*deltap40(k).^2);
        deltac29(k) = deltap29(k)-(a_n15*deltap40(k));

        e_dp29(k) =
            ((1/ratio29std*e_r29(k))^2+(ratio29(k)./ratio29std^2*e_std29')^2+(p2
            9*e_off28)^2+((data28(k)-10500)*e_p29)^2)^0.5;
        e_dp36(k) =
            ((1/ratio36std*e_r36(k))^2+(ratio36(k)./ratio36std^2*e_std36')^2+(p3
            6*e_off40)^2+((data40(k)-8900)*e_p36)^2)^0.5;

```

```

        e_dp40(k) =
        ((1/ratio40std*e_r40(k))^2+(ratio40(k)./ratio40std^2*e_std40')^2+(p4
0*e_off40)^2+((data40(k)-10500)*e_p40)^2)^0.5;
        e_dc29(k) =
        ((e_dp29(k))^2+(a_n15*e_dp40(k))^2+(deltap40(k)*e_a_n15)^2)^0.5;
        e_dc36(k) =
        ((e_dp36(k))^2+((a+2*b*deltap40(k))*e_dp40(k))^2+(deltap40(k)*e_a)^2
+(deltap40(k).^2*e_b)^2)^0.5;
    end
end

%% ans
ans(:,1) = deltac29;
ans(:,2) = deltac36;
ans(:,3) = deltap40;
ans(:,4) = e_dc29;
ans(:,5) = e_dc36;
ans(:,6) = e_dp40;
end

```

Appendix 4. Matlab script for applying the solubility effect corrections

```
function ans = setupcorrectionerror
(d29,d36,d40,gaspercent,e_29,e_36,e_40,e_gp)

sc29 = 5.846*10^-3;
sc36 = -0.2997;
sc40 = 27.337;

e_sc29 = 3.16*10^-3;
e_sc36 = 3.45*10^-2;
e_sc40 = 2.45;

%%
dc29 = zeros(length(d29),1); %+0.1 these are the values
we added from the difference between the oven valve and
the needlevalve
dc36 = zeros(length(d29),1); %+5.96 I am of the
opinion they should not be subtracted from the values.
dc40 = zeros(length(d29),1); %+3.8

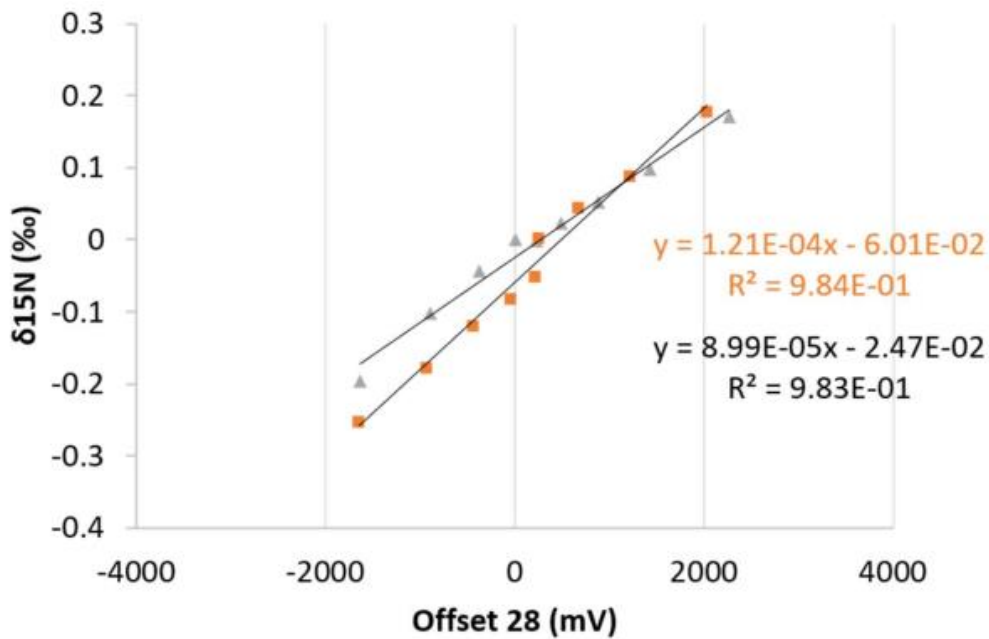
e_dc29 = zeros(length(d29),1);
e_dc36 = zeros(length(d29),1);
e_dc40 = zeros(length(d29),1);

%%
tfnan = isnan(d29);

for k = 1:length(d29)
    if tfnan(k) == 1
        dc29(k) = NaN;
        dc36(k) = NaN;
        dc40(k) = NaN;
        e_dc29(k) = NaN;
        e_dc36(k) = NaN;
        e_dc40(k) = NaN;
    elseif tfnan(k) == 0
        dc29(k) = d29(k)-sc29*log(gaspercent(k)); %+0.1
these are the values we added from the difference between
the oven valve and the needlevalve
        dc36(k) = d36(k)-sc36*log(gaspercent(k));
%+5.96 I am of the opinion they should not be
subtracted from the values.
        dc40(k) = d40(k)-sc40*log(gaspercent(k));
        e_dc29(k) =
(e_29(k)^2+(sc29/gaspercent(k)*e_gp(k))^2+(log(gaspercent
(k))*e_sc29)^2)^0.5;
        e_dc36(k) =
(e_36(k)^2+(sc36/gaspercent(k)*e_gp(k))^2+(log(gaspercent
(k))*e_sc36)^2)^0.5;
        e_dc40(k) =
(e_40(k)^2+(sc36/gaspercent(k)*e_gp(k))^2+(log(gaspercent
(k))*e_sc40)^2)^0.5; %
    end
end
```

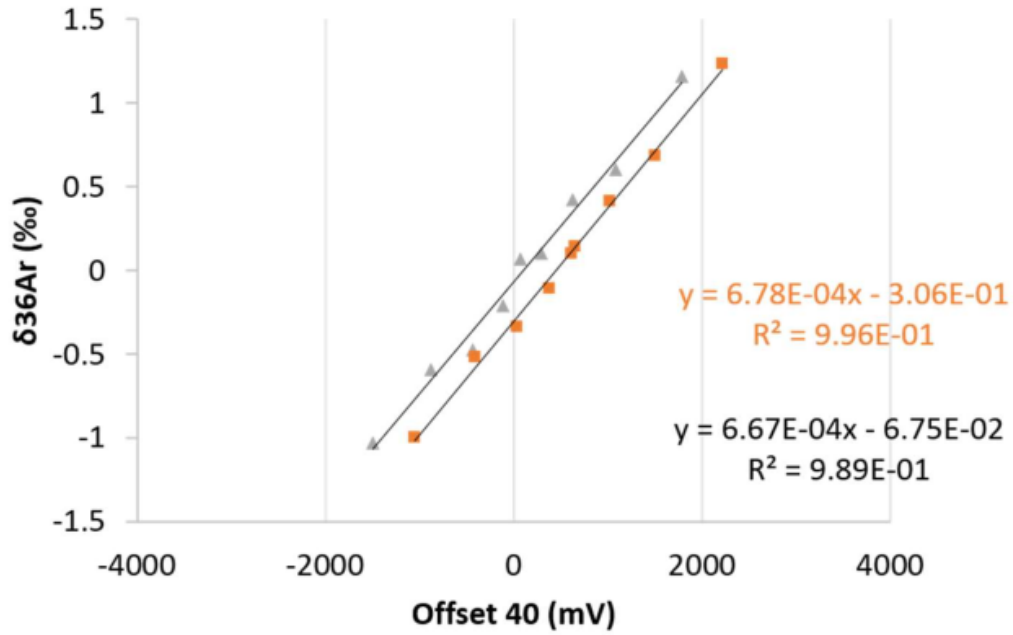
```
%% ans
ans(:,1) = dc29;
ans(:,2) = dc36;
ans(:,3) = dc40;
ans(:,4) = e_dc29;
ans(:,5) = e_dc36;
ans(:,6) = e_dc40;
end
```

Appendix 5. Pressure imbalance slopes found experimentally



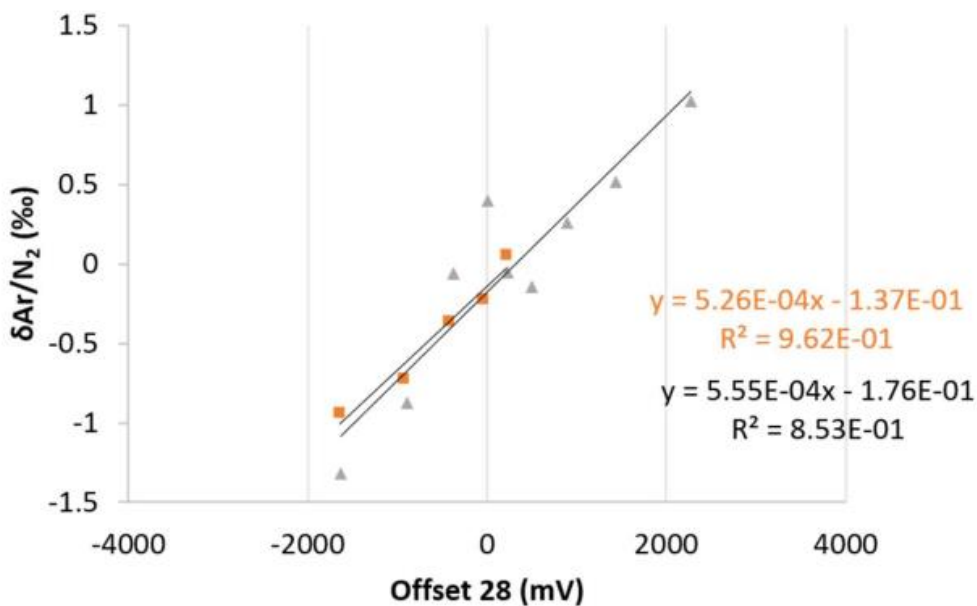
Appendix 5.1.: Pressure imbalance plot for $\delta^{15}\text{N}$. The resulting offset was calculated by intensity28-10500 mV. The two experiments (orange and grey) result in slightly different slopes.

The graph shows the changes in $\delta^{15}\text{N}$ plotted against the offset of intensity 28. The offset was calculated by subtracting 10500 mV from the measured intensity of mass 28, which was determined to be the reference intensity. The FPR on the standard line was changed to determine the pressure imbalance. The pressure setpoint of the FPR was varied from 130 to 160 mbar.



Appendix 5.2.: Pressure imbalance plot for $\delta^{36}\text{Ar}$. The resulting offset was calculated by intensity40-8900 mV. The two experiments (orange and grey) result in similar slopes.

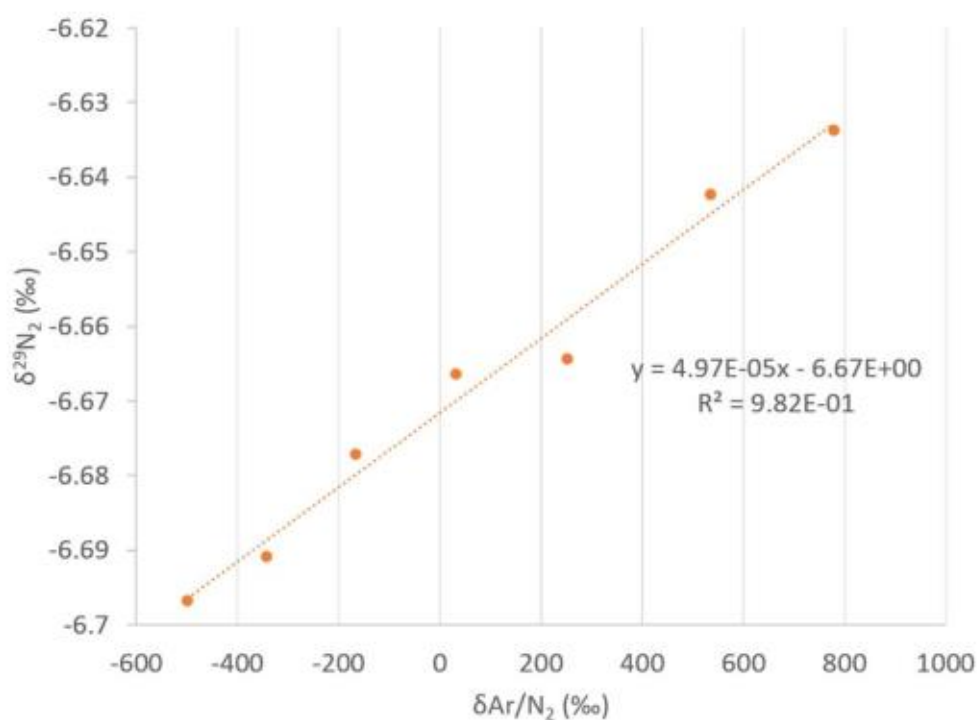
The graph shows the changes $\delta^{36}\text{Ar}$ plotted against the offset of intensity 40. The offset was calculated by subtracting 8,900 mV from the measured intensity of mass 40, which was determined to be the reference intensity. The FPR on the standard line was changed to determine the pressure imbalance. The pressure setpoint of the FPR was varied from 130 to 160 mbar.



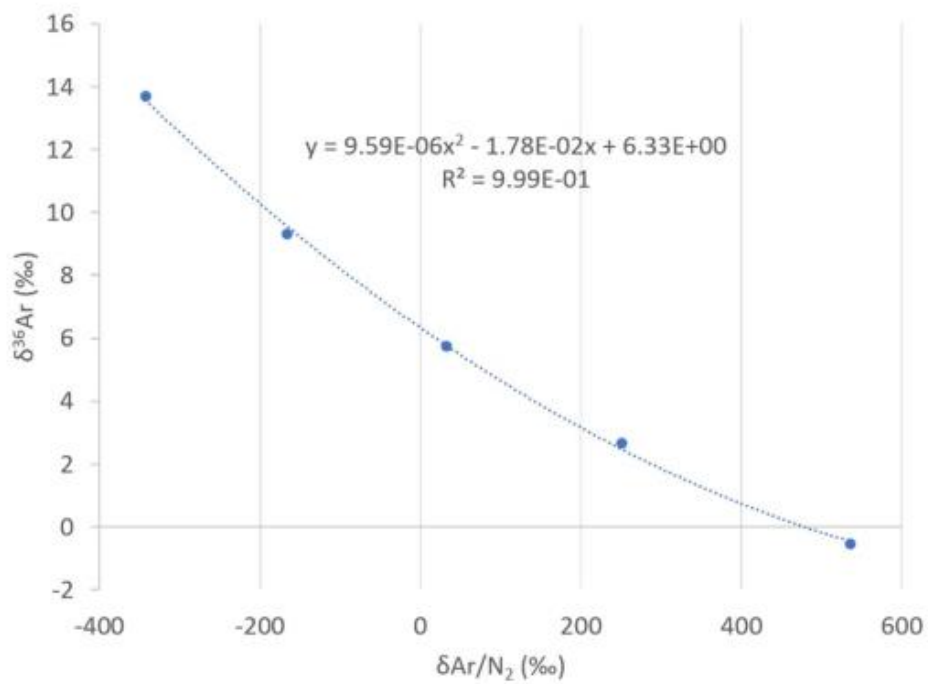
Appendix 5.3.: Pressure imbalance plot for $\delta^{36}\text{Ar}$. The resulting offset was calculated by intensity40-8900 mV.

The graph shows the changes in the elemental ratio $\delta\text{Ar}/\text{N}_2$ plotted against the offset of intensity 28. The offset was calculated by subtracting 10500 mV from the measured intensity of mass 28, which was determined to be the reference intensity. The FPR on the standard line was changed to determine the pressure imbalance. The pressure setpoint of the FPR was varied from 130 to 160 mbar.

Appendix 6. Chemical slopes found experimentally



Appendix 6.1: Chemical slope effect for $\delta^{36}\text{Ar}$ plotted against $\delta\text{Ar}/\text{N}_2$



Appendix 6.2: Chemical slope effect for $\delta^{36}\text{Ar}$ plotted against $\delta\text{Ar}/\text{N}_2$

The graphs 6.1 and 6.2 show the chemical slopes for $\delta^{29}\text{N}_2$ and $\delta^{36}\text{Ar}$ plotted against the elemental ratio of $\delta\text{Ar}/\text{N}_2$. The argon fraction in the dynamically mixed standard was varied between 1.0 and 2.2 bar to change the composition of the standard line.

Appendix 7. Error propagation for $\delta^{29}\text{N}_2$

$$\sigma(r_{29}) = \sqrt{\left(\frac{1}{\text{int}28} \cdot \sigma(\text{int}29)\right)^2 + \left(\frac{\text{int}29}{\text{int}28^2} \cdot \sigma(\text{int}28)\right)^2} \quad (1)$$

$$\sigma(\partial^{29}N_{P.cor}) = \sqrt{\left(\frac{1}{r_{29STD}} \cdot \sigma(r_{29})\right)^2 + \left(\frac{r_{29}}{r_{29STD}^2} \cdot \sigma(r_{29STD})\right)^2 + (P_{29} \cdot \sigma(\text{int}28))^2 + ((\text{int}28 - 10500mV) \cdot \sigma(P_{29}))^2} \quad (2)$$

$$\sigma(\partial^{29}N_{MS.cor}) = \sqrt{\sigma(\partial^{29}N_{P.cor})^2 + \left(\partial \frac{Ar}{N_2MS.cor} \cdot \sigma(a_{29})\right)^2 + \left(a_{29} \cdot \sigma\left(\partial \frac{Ar}{N_2MS.cor}\right)\right)^2} \quad (3)$$

$$\sigma(\partial^{29}N_{air.cor}) = \sqrt{\left((\partial^{29}N_{D.air} + 1) \cdot \sigma(\partial^{29}N_{MS.cor})\right)^2 + \left((\partial^{29}N_{MS.cor} + 1) \cdot \sigma(\partial^{29}N_{D.air})\right)^2} \quad (4)$$

$$\sigma(\partial^{29}N_{cor}) = \sqrt{\left(1 \cdot \sigma(\partial^{29}N_{air.cor})\right)^2 + \left(\frac{S_{29}}{G\%} \cdot \sigma(G\%)\right)^2 + \left(\ln(G\%) \cdot \sigma(S_{29})\right)^2} \quad (5)$$

$$\sigma(\partial^{29}N(x)_{smo}) = \sqrt{\sigma(\partial^{29}N(x)_{cor})^2 + \frac{1}{29} \cdot \sum_{i=x-1}^{x+14} (\partial^{29}N(i)_{cor} - \bar{\partial^{29}N_{cor}})^2} \quad (6)$$

Appendix 8. Error propagation for $\delta^{40}\text{Ar}$

$$\sigma(r_{36}) = \sqrt{\left(\frac{1}{\text{int}40} \cdot \sigma(\text{int}36)\right)^2 + \left(\frac{\text{int}36}{\text{int}40^2} \cdot \sigma(\text{int}40)\right)^2} \quad (1)$$

$$\sigma(\partial^{36}Ar_{P.cor}) = \sqrt{\left(\frac{1}{r_{36STD}} \cdot \sigma(r_{36})\right)^2 + \left(\frac{r_{36}}{r_{36STD}^2} \cdot \sigma(r_{36STD})\right)^2 + (P_{36} \cdot \sigma(\text{int}40))^2 + ((\text{int}40 - 8900mV) \cdot \sigma(P_{36}))^2} \quad (2)$$

$$\sigma(\partial^{36}Ar_{MS.cor}) = \sqrt{\sigma(\partial^{36}Ar_{P.cor})^2 + \left((2b_{36} \cdot \delta 40 + a_{36}) \cdot \sigma(\partial^{40}Ar/N_2MS.cor)\right)^2 + (\delta 40^2 \cdot \sigma(b_{36}))^2 + (\delta 40 \cdot \sigma(a_{36}))^2} \quad (3)$$

$$\sigma(\partial^{36}Ar_{air.cor}) = \sqrt{\left((\partial^{36}Ar_{D.air} + 1) \cdot \sigma(\partial^{36}Ar_{MS.cor})\right)^2 + \left((\partial^{36}Ar_{MS.cor} + 1) \cdot \sigma(\partial^{36}Ar_{D.air})\right)^2} \quad (4)$$

$$\sigma(\partial^{36}Ar_{cor}) = \sqrt{\left(1 \cdot \sigma(\partial^{36}Ar_{air.cor})\right)^2 + \left(\frac{S_{36}}{G\%} \cdot \sigma(G\%)\right)^2 + \left(\ln(G\%) \cdot \sigma(S_{36})\right)^2} \quad (5)$$

$$\sigma(\partial^{36}Ar(x)_{smooth}) = \sqrt{\sigma(\partial^{36}Ar(x)_{cor})^2 + \frac{1}{36} \cdot \sum_{i=x-1}^{x+14} (\partial^{36}Ar(i)_{cor} - \bar{\partial^{36}Ar_{cor}})^2} \quad (6)$$

$$\sigma(\partial^{40}Ar(x)_{smoot}) = \frac{\sigma(\partial^{36}Ar(x)_{smooth})}{(\partial^{36}Ar_{smooth} + 1)^2} \quad (7)$$

Appendix 9. Error propagation for $\delta Ar/N_2$

$$\sigma(r_{Ar/N_2}) = \sqrt{\left(\frac{1}{int28} \cdot \sigma(int40)\right)^2 + \left(\frac{int40}{int28^2} \cdot \sigma(int28)\right)^2} \quad (1)$$

$$\sigma(\partial Ar/N_{2MS.cor}) = \sqrt{\left(\frac{1}{\frac{r_{Ar}}{N_2} \cdot STD} \cdot \sigma(r_{Ar/N_2})\right)^2 + \left(\frac{\frac{r_{Ar}}{N_2}}{\frac{r_{Ar}^2}{N_2} \cdot STD} \cdot \sigma\left(\frac{r_{Ar}}{N_2} \cdot STD\right)\right)^2 + \left(\frac{P_{Ar}}{N_2} \cdot \sigma(int28)\right)^2 + \left((int28 - 10500mV) \cdot \sigma(P_{Ar/N_2})\right)^2} \quad (2)$$

$$\sigma(\partial Ar/N_{2air.cor}) = \sqrt{\left((\partial Ar/N_{2D.air} + 1) \cdot \sigma(\partial Ar/N_{2MS.cor})\right)^2 + \left((\partial Ar/N_{2MS.cor} + 1) \cdot \sigma(\partial Ar/N_{2D.air})\right)^2} \quad (3)$$

$$\sigma(\partial Ar/N_{2cor}) = \sqrt{\left(1 \cdot \sigma(\partial Ar/N_{2air.cor})\right)^2 + \left(\frac{S_{29}}{G\%} \cdot \sigma(G\%)\right)^2 + \left(\ln(G\%) \cdot \sigma(S_{29})\right)^2} \quad (4)$$

$$\sigma(\partial Ar/N_2(x)_{smoot}) = \sqrt{\sigma(\partial Ar/N_2(x)_{cor})^2 + \frac{1}{29} \cdot \sum_{i=x-1}^{x+14} (\partial Ar/N_2(i)_{cor} - \bar{\partial Ar/N_2}_{cor})^2} \quad (5)$$